UNIVERSITÄT KARLSRUHE (TH)

Physikalisches Institut

Jahresbericht

Annual report

2008

Redaktion: G. Fischer, W. Wulfhekel

Prof. Dr. Hilbert v. Löhneysen
Prof. Dr. Alexey Ustinov
Prof. Dr. Georg Weiß
Prof. Dr. Wulf Wulfhekel
Apl. Prof. Dr. Gernot Goll
Apl. Prof. Dr. Bernd Pilawa

Physikalisches Institut
Universität Karlsruhe
D - 76128 Karlsruhe
Germany

Telefon: +49 (0) 721 608 3451
Fax: +49 (0) 721 608 6103
Internet: http://www.pi.uni-karlsruhe.de
E-Mail: pi@physik.uni-karlsruhe.de

Dear Colleagues and Friends,

With the Annual Report 2008 of our Institute, we present an overview over our last year's activities ranging from fundamental properties of solids to more materials-related aspects. Our research interests cover electronic transport in nano-structured metallic systems, superconductivity, quantum computing, magnetism, physics of strongly correlated electron systems, metal-insulator transitions, atomic dynamics of disordered solids, and chemical physics. Since this report cannot cover all our activities, you are welcome to contact us for further information.

The year 2008 brought many changes to our institute. After Elmar Dormann retired as a professor in the fall of 2007, we were joined by his successor Alexey Ustinov and his group in spring 2008. Alexey's research interest is focused on quantum computing, coherence in nano-structures as well as low temperature solid state physics. We all wish him a a good start and many interesting discoveries in the years to come.

On June 5, 2008 our dear secretary Monika Hornung passed away at the age of only 45 years after a short but severe illness. She had been responsible for book-keeping for our former SFB 195 from 1994 to 2004 and then took over this responsibility for the much larger research activities in the Center for Functional Nanostructures. Despite this overburdening tasks, she managed to contribute to the secretarial and book-keeping chorus of our Institute. With her energetic way to tackle problems and her positive attitude she very much contributed to the friendly and creative atmosphere in the Institute.

The Karlsruhe Institute of Technology (KIT) continued in taking shape with the aim that research at the University and at the Forschungszentrum Karlsruhe will be even more entangled. One of the fields of competence of the KIT will be Condensed Matter with H. v. Löhneysen as the spokesperson. Our Institute is involved with all of its groups.

The strong links between our Institute and the Institute for Solid State Physics (IFP) of Forschungzentrum Karlsruhe has been manifested for the last decades through regular joint seminars. Both Institutes have projects in the Research Unit "Quantum Phase Transitions" (FOR 960) funded by the Deutsche Forschungsgemeinschaft (DFG) with participating groups from Augsburg, Dresden, Göttingen, Karlsruhe, Köln, and München and with H. v. Löhneysen as spokesperson.

All groups of Physikalisches Institut participate in the "Center for Functional Nanostructures" (CFN) funded by the DFG. This center provides substantial support for our research activities in the field of electronic transport in sub-micron structures down to single molecules and atoms as well as in superconducting circuits. Numerous further projects were funded by the Landesstiftung Baden-Württemberg, the DFG, the Ministerium für Wissenschaft, Forschung und Kunst in Baden-Württemberg, the Alexander von Humboldt Foundation, the German Academic Exchange Service, and the European Science Foundation.

Our research activities would not have been possible without the dedicated and hard work of all scientific and technical staff and, of course, the doctorate and diploma students. We thank Steffi Baatz, Birgit Schelske and the late Monika Hornung for their help and support in book-keeping and secretarial services. Lars Behrens takes care very skillfully of all our graphic work, runs our internet page, and manages the PC network. We would like to thank Reinhold Dehm and his team of the mechanical workshop, Orhan Aydin and the team of the electronics workshop, and Franz Hartlieb who runs the He liquefaction facilities. The scientific results presented in this report have largely profited from the expert work of apl. Prof. Dr. Gernot Goll and apl. Prof. Dr. Bernd Pilawa, the post-doc scientists Dr. Veronika Fritsch, Dr. Regina Hoffmann-Vogel, Dr. Jürgen Lisenfeld, Dr. Oleksandre Lukashenko, Dr. Carmen Pérez León, Dr. Stefano Poletto, Dr. Lars Schnelzer, Dr. Albert Takács, and – last but definitely not least – of our permanent scientific staff Dr. Gerda Fischer and Dr. Christoph Sürgers.

Karlsruhe, January 2009

Hilbert v. Löhneysen   Alexey Ustinov   Georg Weiß   Wulf Wulfhekel

Monika Hornung
27. Dezember 1962* – 5. Juni 2008†

Contents

Signature of quantum criticality in photoemission spectroscopy

M. Klein[1], A. Nuber[1] , F. Reinert[1,2], J. Kroha[3], O. Stockert[4], H. v. Löhneysen

A quantum phase transition (QPT) is a second-order transition occurring at zero temperature, driven by a nonthermal control parameter such as composition or pressure. Here, two competing groundstates are separated by a quantum critical point (QCP). Heavy-fermion (HF) systems, in particular, show striking deviations from Fermi-liquid (FL) behavior at a QPC between a magnetically ordered and a paramagnetic phase [1, 2]. In the standard Hertz-Millis (HM) scenario [3, 4] only the bosonic fluctuations of the order parameter become quantum critical, i.e., long-ranged in space and time, leading to anomalous behavior of physical quantities, but leaving the fermionic quasiparticles intact. However, in a heavy fermion (HF) system the order-parameter fluctuations always couple to the spin degree of freedom of the fermionic excitations, so that the latter may become critical as well and disintegrate. In this case, the formation of the Kondo spin singlet between the conduction electron and the local $4f$ magnetic moments is prevented, and hence the Kondo scale T_K vanishes at the quantum critical point (QCP). This scenario has, therefore, been termed local quantum critical (LQC) [5, 6] and was prompted by extensive experiments on $\mathrm{CeCu}_{6-x}\mathrm{Au}_x$ which is one of the best characterized HF compounds [1] with a QPT between a fully Kondo-screened paramagnetic and an antiferromagnetically ordered phase at a critical Au concentration of $x_c = 0.1$. In particular, inelastic neutron scattering experiments [7] led to the suggestion of the LQC scenario.

Ultraviolet photoemission spectroscopy (UPS) measurements provide the most immediate access to the screening scale T_K by directly recording the Kondo resonance (KR) in the local Ce $4f$ spectrum [8, 9]. The high-resolution UPS was performed with a Gammadata R4000 analyzer and a monochromatized VUV lamp at $h\nu = 40.8$ eV. We cleaved the single-crystaline samples *in situ* just before the measurement, already at the measurement temperature.

The inset of Fig. 1(a) shows survey spectra for five Au concentrations x at $T = 15$ K. The energy range includes the spin-orbit (SO) feature at $E_B \approx 260$ meV and the tail of the Kondo resonance just below the Fermi energy E_F. A distinct crystal-field (CF) feature as observed, e.g., in $\mathrm{CeCu_2Si_2}$ and $\mathrm{CeNi_2Ge_2}$ [8, 9], is expected near $E_B = 7$ meV, but strongly broadened and, hence, not discernible in $\mathrm{CeCu}_{6-x}\mathrm{Au}_x$. In order to investigate the KR in more detail we performed high-resolution measurements near E_F (Fig. 1(a)). For all concentrations one observes a significant rise in the intensity from $E_B \approx 20$ meV towards E_F, attributed to the tail of the KR which has its major spectral weight a few meV *above* the Fermi energy and hence is suppressed by the Fermi-Dirac distribution function (FDD) in the UPS data. Normalizing to the FDD allows to recover the thermally occupied spectrum up to $\approx 5k_BT$ above E_F [8, 9] and reveals the KR. Fig. 1 shows the FDD-renormalized spectra for $x = 0.1$ (b) and 0.2 (c). In the low-T spectra ($T = 15\,\mathrm{K}$) at the KR maximum is at about 3 meV above E_F for $x = 0.1$ and at 1 meV for $x = 0.2$. The striking feature is the significant drop of the spectral weight of the KR from $x = 0.1$ to 0.2, i.e., in the vicinity of the critical concentration x_c.

To extract the Kondo screening scale T_K from the experimental results, one must bear in mind that the coherence temperature T_{coh} obtained from resistivity measurements [10] as well as the Kondo scale extracted from specific heat [11] or neutron scattering data [12, 7], are well below our lowest experimental temperature. Moreover, quantum critical fluctuations, which in $\mathrm{CeCu}_{6-x}\mathrm{Au}_x$ extend up to about $T = 7$ K [7] and certainly become crucial at low T, are not expected to influence our experimental spectra. Thus, our data exhibit the onset of the *local* Kondo physics on the Ce atoms only. Therefore, the single-impurity Anderson model (SIAM) is employed to interpret the experimental data. To determine T_K we follow the procedure successfully applied to various Ce compounds in the past [8, 9]: Using the non-crossing approximation (NCA) [13] we calculate the Ce $4f$ spectral function of the SIAM, including all CF and SO excitations. For each composition x the NCA spectra are broadened by the experimental resulotion and fitted to the experimental data, using a single parameter set for all experimental T. The NCA spectra are then computationally extrapolated to $T \approx 0.1\,T_K$, where T_K is extracted from the Kondo-peak half-width at half maximum (HWHM).

Fig. 2 shows the x dependence of T_K for $\mathrm{CeCu}_{6-x}\mathrm{Au}_x$ obtained from our UPS data, compared to results of various other experiments [10 − 12]. We emphasize that, irrespective of a possible systematic ambiguity in the fit procedure, the surprisingly abrupt step of T_K near $x_c \approx 0.1$ is significant and already clearly visible in the raw data (Fig. 1). What can be learnt from this step-like behavior at elevated T about the nature of the QPT at $T = 0$? The method of extracting a Kondo scale

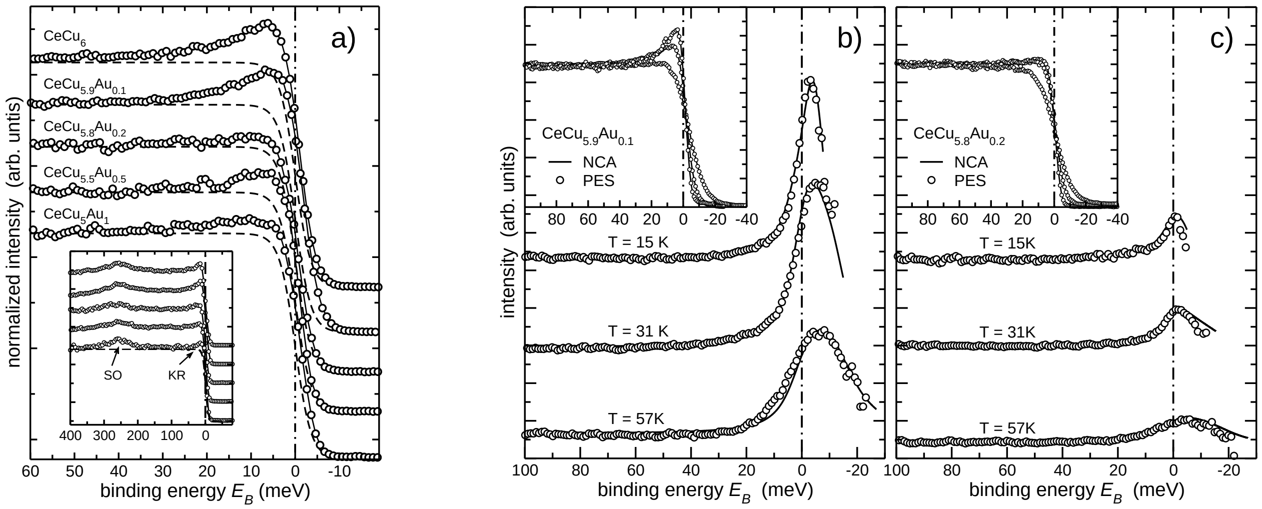

Figure 1: (a) Near-E_F spectra of CeCu$_{6-x}$Au$_x$ for five different Au concentrations at $T = 15$ K ($h\nu = 40.8$ eV, energy resolution $\Delta E = 4.9$ meV), normalized at $E_B \approx 100$ meV. The dashed lines describe the resolution broadened FDD at $T = 15$ K. The inset shows a larger energy range including the SO partner at $E_B \approx 260$ meV ($\Delta E = 15$ meV). (b) and (c) show spectra for $x = 0.1$ and $x = 0.2$, respectively, devided by the FDD, at various T. The solid lines are best NCA fits for the resulting model parameter values. The insets in (b) and (c) show the corresponding raw data.

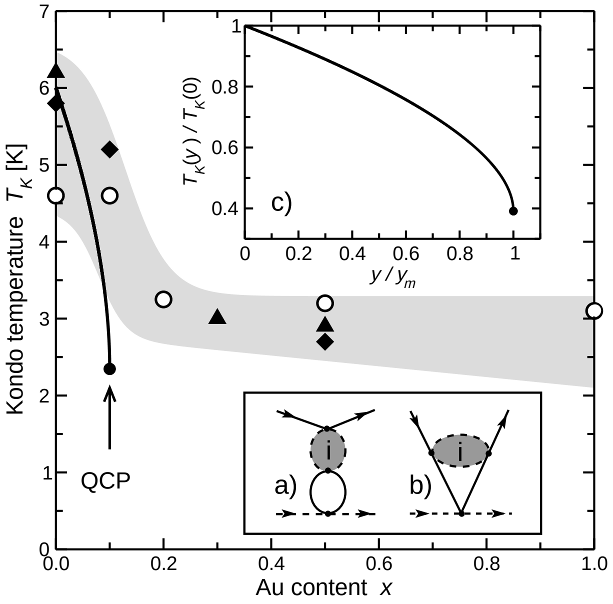

Figure 2: Dependence of the Kondo temperature T_K on the Au content x, as determined by UPS (open circles), specific heat [11] (triangles) and neutron scattering [7, 12] (diamonds). The shaded area is a guide to the eye. The insets (a) and (b) show diagrammatic representations of the RKKY corrections to the local Kondo vertex. The inset (c) and the solid line in the main panel show the universal curve $T_K(y)/T_K(0)$ vs. y/y_m as given by Eq.(1)

from a single-ion picture described above mimics exactly a system of dense Kondo atoms that, however, would *not* undergo any lattice coherence or magnetic ordering at sufficiently low T. This scenario is different from the low-T behavior of the Kondo lattice and two-impurity Kondo problems, where Kondo spin screening competes with the formation of inter-impurity coherent states [14] or could be destroyed by critical fluctuations of a magnetic order parameter [15]. By contrast, our system is represented by an effective single-impurity Kondo model where the (bare) Kondo exchange coupling J is renormalized by the local spin fluctuations on the surrounding *identical* Kondo atoms through the indirect Ruderman-Kittel-Kasuya-Yosida (RKKY) coupling. This problem can be treated in a controlled way by renormalization group (RG) enhanced perturbation theory which allows for definite predictions about the formation of HF quasiparticles at low T.

In particular, a highly non-linear renormalization of T_K is given by the self-consistency equation:

$$\frac{T_K(y)}{T_K(0)} = \exp\left\{-\left(\frac{1}{2g} + \ln 2\right) \frac{f(u)}{1 - f(u)}\right\} \qquad (1)$$

with $g = N(0)J$, $f(u) = u - u^2/2$, $u = yg^2D_0/[4T_K(y)]$, N_0 the density of states at the Fermi level, and $D_0 \approx E_F$ the band cutoff. y is a dimensionless factor which describes the (experimentally not known) relation between the RKKY coupling strength and the Au content x. We assume a linear dependence across the QPT, $y = \alpha(x + x_0)$, with adjustable parameters α and x_0. For details, see [16]. The single-ion Kondo scale without RKKY coupling is $T_K(0) = D_0 \exp(-1/2g)$. We have verified that this perturbative RG treatment of the RKKY corrections is controlled in the sense that the effective perturbation parameter $f(u) \leq 0.1$ for all self-consistent solutions, i.e., the exponent in Eq. (1) remains small.

The solution of Eq. (1) is universal in the dimensionless variables $T_K(y)/T_K(0)$ and y/y_m and turns out to exist only for y smaller than a maximum value y_m. Hence, as the essential result of this analysis, in a dense system of Kondo ions, complete Kondo screening ceases to exist above a critical RKKY coupling strength, $y > y_m$, even if magnetic ordering does not occur. The theory predicts two possible scenarios, depending on the size of $T_K(0)/D_0$: (1) Magnetic ordering at $T = 0$ occurs for an RKKY parameter $y = y_{\mathrm{SDW}} \leq y_m$, i.e., without breakdown of Kondo screening. The ordering may arise in this case from a $T = 0$ spin-density-wave (SDW) instability of the underlying heavy Fermi liquid. This corresponds to the HM scenario. In this case, a step-like behavior of T_K as extracted from the high-T UPS spectra is still predicted from Eq. (1) at $y = y_m$, i.e., inside the region where magnetic ordering occurs at $T < T_N$. (2) Magnetic ordering does not occur for $y < y_m$. In this case Eq. (1) indicates a breakdown of Kondo screening at the magnetic QCP, and quantum critical fluctuations (not considered in our theory) will suppress the low-T spin screening scale to zero at this point. This is the LQC scenario. The sharp step of T_K occurring in our UPS data very close to x_c (see Fig. 2) strongly supports that $\mathrm{CeCu}_{6-x}\mathrm{Au}_x$ falls into the latter class, as was previously inferred indirectly from inelastic neutron scattering data [7].

[1] H. v. Löhneysen et al., Rev. Mod. Phys. **79**, 1015 (2007)
[2] P. Gegenwart et al., Nature Phys. **4**, 186 (2008)
[3] J. A. Hertz, Phys. Rev. B **14**, 1165 (1976)
[4] A. J. Millis, Phys. Rev. B **48**, 7183 (1993)
[5] Q. Si et al., Nature **413**, 804 (2001)
[6] P. Coleman et al., J. Phys. Condens. Matter **13**, R723 (2001)
[7] A. Schröder et al., Nature **407**, 351 (2000)
[8] F. Reinert et al., Phys. Rev. Lett. **87**, 106401 (2001)
[9] D. Ehm et al., Phys. Rev. B **76**, 045117 (2007)
[10] H. v. Löhneysen et al., J. Alloys Compd. **408-412**, 9 (2006)
[11] H. G. Schlager et al., J. Low Temp. Phys. **90**, 181 (1993)
[12] B. Stroka et al., Z. Phys. B **90**, 155 (1993)
[13] T. Costi et al., Phys. Rev. B **90**, 1850 (1996); N. E. Bickers et al., Phys. Rev. B **36**, 2036 (1987)
[14] B. A. Jones, C. M. Varma, Phys. Rev. Lett. **58**, 843 (1987)
[15] H. Maebashi et al., Phys. Rev. Lett. **95**, 207207 (2005)
[16] M. Klein et al., Phys. Rev. Lett. **101**, 266404 (2008)

[1] Universität Würzburg, Experimentelle Physik II, Am Hubland, D-97074 Würzburg, Germany and
[2] Forschungszentrum Karlsruhe, Gemeinschaftslabor für Nanoanalytik, D-76021 Karlsruhe, Germany
[3] Universität Bonn, Physikalisches Institut, Nussallee 12, D-53115 Bonn, Germany
[4] Max Planck Institute for Chemical Physics of Solids, Nöthnitzer Str. 40, 01187 Dresden, Germany

Thermal expansion: a particularly sensitive probe for phase transitions approaching zero temperature

S. Drobnik, S. Zaum[1], K. Grube[1], C. Meingast[1], O. Stockert[2], and H. v. Löhneysen

The heavy-fermion compound $\mathrm{CeCu}_{6-x}\mathrm{Au}_x$ with $x = 0.15$ orders antiferromagnetically below a Néel temperature of $T_N \approx 82\,\mathrm{mK}$ [1]. When the continuous phase transition is shifted to zero temperature by reducing the Au content to $x \approx 0.1$, the system reaches a quantum critical point (QCP). Close to this point, measurements of the thermodynamic and transport properties reveal strong deviations from Fermi-liquid behavior, e.g., the coefficient of the specific heat does not become constant but diverges logarithmically with decreasing temperature, $C/T \propto \ln(T_0/T)$.

In Figure 1 the magnetic susceptibility χ, specific heat C, and the volumetric thermal expansion coefficient β divided by T of a $\mathrm{CeCu}_{5.85}\mathrm{Au}_{0.15}$ single crystal are displayed as a function of temperature. The susceptibility measurement, plotted in Fig. 1(a), shows clearly the transition to antiferromagnetism [2]. In the specific heat measurement, on the other hand, the phase transition is only visible as a tiny feature on top of an excessive non-Fermi liquid background, which above T_N is reminiscent of that of a sample at the critical composition $x_c \approx 0.1$, i.e., right at the QCP with, however, a reduced T_0 (solid line Fig. 1(b)) [1]. Neutron scattering experiments [3] indicate a very small ordered moment (see Fig. 2). Similar to C/T, the pronounced temperature dependence of β/T shows above T_N strong deviations from Fermi-liquid behavior (see Figure 1c). Surprisingly, β/T reveals, in contrast to χ and C, a huge discontinuity at T_N [4]. Apparently, thermal expansion measurements are especially sensitive to phase transitions approaching $T = 0$.

In the following we will show that the large difference between the discontinuities of β and C is caused by a fundamental property of quantum phase transitions. If the QCP is reached by a volume change, β and C are related to each other via the volume dependence of the energy scale, $E^\star$, which characterizes the system. Usually, such a dependence is described in terms of the so-called Grüneisen parameter $\Gamma = V_m B_S \cdot \beta/C$, where V_m denotes the molar volume, B_S the isentropic bulk modulus, and C the isobaric specific heat. Assuming that the entropy S (or free energy) of the system is dominated by a single energy, so that $S = f(T/E^*)$, Γ reflects the normalized volume dependence of $E^\star$:

$$\Gamma = \frac{\partial S/\partial \ln(V_m)|_T}{\partial S/\partial \ln(T)|_{V_m}} = -\left.\frac{\partial \ln(E^\star)}{\partial \ln(V_m)}\right|_S .$$

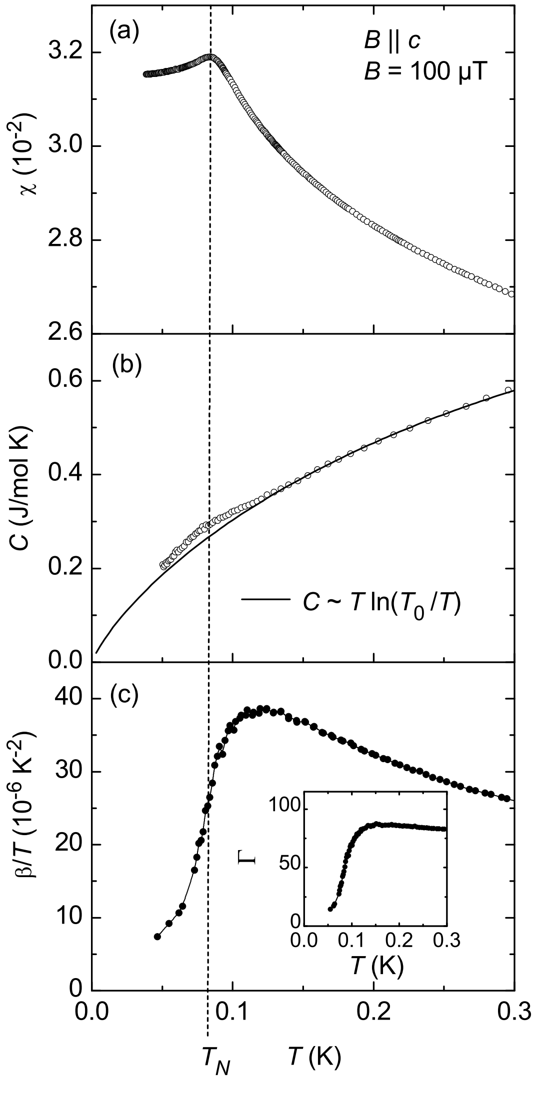

Figure 1: Thermodynamic measurements of a $\mathrm{CeCu}_{5.85}\mathrm{Au}_{0.15}$ single crystal versus T: a) The magnetic susceptibility measured in a magnetic field of $B = 100\,\mu\mathrm{T}$ parallel to the easy axis [2]. b) The specific heat at zero magnetic field [1]. c) The ratio of the thermal expansion coefficient to the temperature [4]. The inset displays the Grüeisenparameter calculated with the β and C data.

As, at the onset of a macroscopically ordered state, the associated characteristic energy scale vanishes, Γ has to diverge when the QCP is approached [5] unless the volume dependence of $E^\star$ vanishes.

In general, properties of solids are determined by more than a single characteristic energy scale. In this case one has to disentangle the different Grüneisen parameters $\Gamma_i = V_m B_S \cdot \beta_i / C_i$ by extracting the individual contributions to $C = \sum C_i$ and $\beta = \sum \beta_i$ arising from various energy scales $E_i^\star$ under the assumption that all subsystems experience the same B_S [6]. A convenient way to get the Grüneisen parameter of an ordered phase is to assume discontinuities of β and C at a second order phase transition by replacing the measured $\beta(T)$ and $C(T)$ by an equal-volume or equal-entropy construction.

The ground state of the heavy-fermion compound $\mathrm{CeCu}_{6-x}Au_x$ is decisively determined by the crystal volume V due to the high sensitivity of the Kondo effect to the $4f$-electron-conduction-electron hybridization. Experimentally, V is changed by the application of pressure p or the substitution of Cu with larger, isoelectronic Au ions. As $E^\star$ is roughly given by the transition temperature T_N we get the Grüneisen parameter of the antiferromagnetic phase in terms of the well-known Ehrenfest relation [7]:

$$\Gamma_{AF}|_{T=T_N} = V_m B_S \cdot \frac{\Delta\beta}{\Delta C} = \frac{V_m}{T_N} \cdot \left.\frac{\partial T_N}{\partial V_m}\right|_S .$$

As a result the discontinuity $\Delta\beta$ is directly proportional to $\Gamma_{AF} \cdot \Delta C$ and can, therefore, diverge if the QCP is approached. In fact, measurements on $\mathrm{CeCu}_{6-x}\mathrm{Au}_x$ crystals with different Au contents show that with decreasing T_N, $\Delta\beta$ grows disproportionately in comparison to ΔC [1, 8].

For the measurements of $\mathrm{CeCu}_{5.85}\mathrm{Au}_{0.15}$, shown in Fig. 1, the Ehrenfest relation yields an initial pressure dependence $dT_N/dp \approx -0.65\,\mathrm{K/GPa}$. This value is in reasonable agreement with the independently determined pressure effect of $\mathrm{CeCu}_{5.8}\mathrm{Au}_{0.2}$, $dT_N/dp \approx -0.43\,\mathrm{K/GPa}$, measured resistively in a hydrostatic pressure cell [9]. Assuming a bulk modulus $B_S \approx 100\,\mathrm{GPa}$ [10] and using $V_m = 6.3 \cdot 10^{-5}\,\mathrm{m}^3/\mathrm{mol}$ [11], Γ_{AF} attains an enormously high negative value of -700 ± 100 which agrees quite well with the value, $\Gamma_{AF} \approx -605$ estimated from the x dependence of V and T_N. Consequently, the large difference between $\Delta\beta$ and ΔC can indeed be attributed to the volume dependence of T_N and reflects the strongly enhanced Γ_{AF} at the QCP.

The large Γ_{AF} values, however, cannot be seen in the effective, total Grüneisen parameter Γ of the entire system, depicted in the inset of Fig. 1(c). At the QCP the magnetic interactions compete with the Kondo effect which leads likewise to a large, but this time positive, Grüneisen parameter Γ_{Kondo}. As Γ weights the different Γ_i's according to their contributions to the specific heat, $\Gamma = \sum(C_i/C) \cdot \Gamma_i$, the large, Kondo-dominated background of C apparently cancels the negative Γ_{AF} below T_N. The volume and temperature dependence of Γ_{AF} and Γ_{Kondo} and their interplay next to the QCP will be the subject of future investigations.

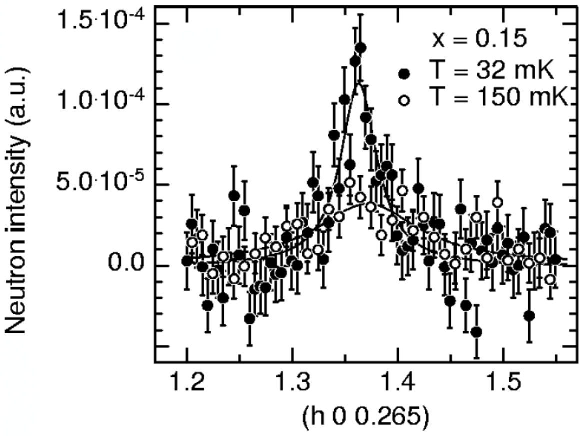

Figure 2: Neutron scattering intensity for elastic scans of $\mathrm{CeCu}_{5.85}\mathrm{Au}_{0.15}$ along $(h\,0\,0.265)$ measured with an incident energy of $E_0 = 2.74\,\mathrm{meV}$ below $T_N = 82\,\mathrm{mK}$ [3].

[1] H. v. Löhneysen et al., Rev. Mod. Phys. **79**, 1015 (2007).

[2] A. Hamann, diploma thesis, Universität Karlsruhe, 2006.

[3] H. v. Löhneysen et al., Acta Phys. Pol. B **32**, 3313 (2001).

[4] S. Drobnik, Ph.D. thesis, Universität Karlsruhe, 2008.

[5] L. Zhu et al., Phys. Rev. Lett. **91**, 066404 (2003).

[6] T.H.K. Barron et al., Adv. Phys. **29**, 609 (1980).

[7] P. Ehrenfest, Leiden Comm. Suppl. **75b**, 628 (1933).

[8] P. Estrella et al., J. Magn. Magn. Mater. **272-276**, 23 (2004).

[9] H. v. Löhneysen et al., Phys. Rev. B **63**, 134411 (2001).

[10] K. Grube et al., unpublished results.

[11] T. Pietrus et al., Physica B **206&207**, 317 (1995).

---

[1] Forschungszentrum Karlsruhe, Institut für Festkörperphysik, 76021 Karlsruhe, Germany.

[2] MPI für chemische Physik fester Stoffe, 01187 Dresden, Germany.

Magnetic order by C-ion implantation into Mn_5Si_3 and Mn_5Ge_3

C. Sürgers, N. Joshi, G. Fischer, H. v. Löhneysen, K. Potzger[1], T. Strache[1], W. Möller[1]

Metal-semiconductor compounds like Mn_5Ge_3 have been considered as promising candidates for spintronic applications due to their easy implementation into the semiconductor-based device fabrication-technology [1]. The rather low Curie temperature T_C =304 K of Mn_5Ge_3, which is a severe disadvantage for technological applications, is enhanced in $Mn_5Ge_3C_{0.8}$ films obtained by magnetron sputtering to a maximum $T_C = 445$ K [2] due to insertion of carbon into the voids of Mn octahedra of the hexagonal structure [3]. Similarly, the isostructural antiferromagnetic Mn_5Si_3 ($T_N = 99$ K) can be driven ferromagnetic by insertion of carbon yielding $Mn_5Si_3C_{0.8}$ with $T_C = 350$ K [4]. Hence, ferromagnetic $Mn_5Si_3C_x$ or $Mn_5Ge_3C_x$ could be appealing materials for implementation into semiconductor-based magnetoelectronic devices.

In an alternative approach to co-sputtering of Mn, Si or Ge, and C, we report here the preparation of ferromagnetic $Mn_5Si_3C_{0.8}$ and $Mn_5Ge_3C_{0.8}$ with T_C well above room temperature by implantation of carbon into antiferromagnetic Mn_5Si_3 or ferromagnetic Mn_5Ge_3 films [5] which were deposited by magnetron sputtering on sapphire substrates at optimum substrate temperatures $T_S = 450\,^\circ$C and $400\,^\circ$C, respectively, as described earlier [4]. Each 400-nm thick film was protected by 5 - 10 nm Si or Ge to avoid oxidation in air during transfer to the ion implanter. $^{12}C^+$-ion implantation was performed in three steps of 195, 100, and 45 keV energy [5]. The structure of all polycrystalline films (typical grain size $\approx$ 100 nm) was of Mn_5Si_3 type (hexagonal $D8_8$ structure) as checked by $\theta - 2\theta$ x-ray diffractometry [4].

Figure 1 shows the temperature dependence of the magnetization $M(T)$ measured with a superconducting quantum interference device (SQUID) magnetometer in a weak magnetic field $\mu_0 H = 2.5$ mT applied parallel to the film plane. We mention that $M(T)$ of the C-implanted $Mn_5Si_3C_{0.8}$ [Fig. 1(a)] was recorded after demagnetization of the system in contrast to all other data that were recorded after magnetization. This explains the reduction of the magnetization $M(T)$ for $T < 200$ K with respect to sputtered $Mn_5Si_3C_{0.8}$. The implanted film has almost the same Curie temperature T_C as the sputtered film. In addition, the implanted $Mn_5Si_3C_{0.8}$ film shows a reduced coercivity and a higher saturation moment $m_S \approx 1.2\ \mu_B$/Mn than the sputtered film, see the $M(H)$ loops in the inset of Fig. 1(a). This is the highest moments for ferromagnetic $Mn_5Si_3C_{0.8}$ reported so far.

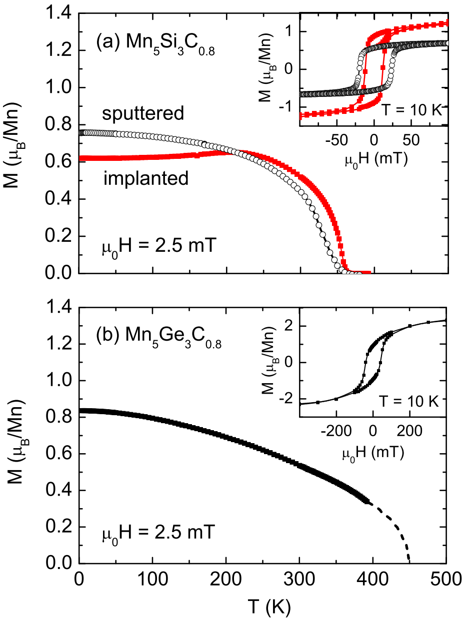

Figure 1: (a) Magnetization $M(T)$ of ion implanted (closed symbols) and magnetron sputtered (open circles) $Mn_5Si_3C_{0.8}$ films. (b) $M(T)$ of ion implanted $Mn_5Ge_3C_{0.8}$. Dashed line indicates the extrapolation towards $M(T_C) = 0$ for temperatures above the experimental limit of the magnetometer. Insets show $M(H)$ loops taken at $T = 10$ K.

A similar behavior was observed for C-implanted $Mn_5Ge_3C_{0.8}$, see Fig. 1(b), with an extrapolated, strongly enhanced $T_C \approx 420$ - 450 K compared to $T_C = 304$ K of Mn_5Ge_3 in agreement with T_C = 445 K obtained for sputtered $Mn_5Ge_3C_{0.8}$ [2]. The deviation of $M(T)$ from the Bloch-like behavior of an isotropic ferromagnet is attributed to the easy axis not lying perfectly in the plane. This is also inferred from the shape of the $M(H)$ loop [inset Fig. 1(b)]. We mention that the coercivity and m_S decrease with increasing temperature but the shape of the $M(H)$ loop does not change notably with T. At $T = 10$ K, the average saturated moment $m_S \approx 2.2\ \mu_B$/Mn is similar to that of sputtered $Mn_5Ge_3C_{0.8}$ [2] and somewhat smaller than 2.6 μ_B/Mn of Mn_5Ge_3 polycrystals [6]. m_S is in good agreement with an average moment of 2.3 μ_B/Mn estimated from an empirical model, where the individual Mn moments in Mn_5X_3 (X = Si, Ge) compounds strongly depend

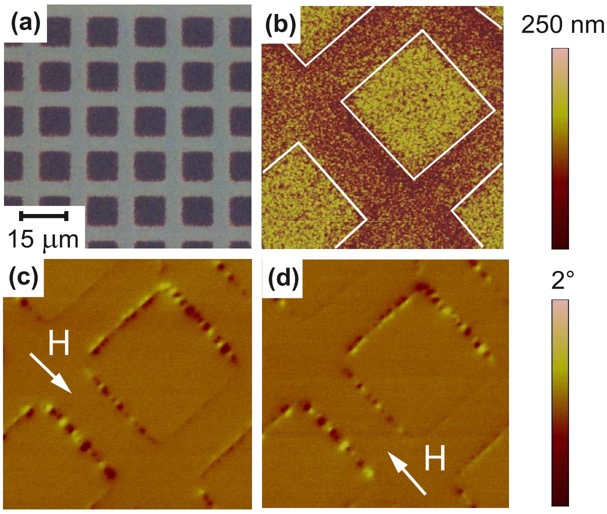

Figure 2: (a) Optical micrograph of Mn_5Si_3 irradiated with $^{12}C^+$ ions through a 7 μm × 7 μm gold mesh. C-implanted regions appear dark. (b) AFM image (25 μm× 25 μm) of the topography. Ion-irradiated squares are indicated by white lines. (c) MFM images taken in an applied magnetic field μ_0H = 50 mT and (d) after field reversal.

on the different Mn-Mn bond lengths [7], as discussed earlier [2].

After having verified the ferromagnetic properties of C-implanted $Mn_5Si_3C_{0.8}$ and $Mn_5Ge_3C_{0.8}$ films, we focus on the lateral modification of the magnetic order by ion implantation. Patterning was achieved by using a commercially available 100-μm thick gold mesh with 7 μm × 7 μm square openings (Plano GmbH, Germany) serving as a stencil mask during implantation of the virgin carbon-free films. For the simultaneous measurement of laterally resolved structural and magnetic properties we used an atomic force microscope (AFM, Veeco/DI Multimode) with magnetic force microscopy (MFM) option. In MFM, the contrast results from stray fields arising from finite domains and domain walls. The system was operated in the tapping mode at room temperature in air. For MFM, a tip from Nanosensors^{TM} with Co/Cr coating was used which was magnetized along the tip axis.

Figure 2(a) shows an optical micrograph and Fig. 2(b) an AFM image of patterned $Mn_5Si_3/Mn_5Si_3C_{0.8}$, both taken at room temperature. The implanted areas show an implantation-induced expansion perpendicular to the surface (swelling). They protrude by about 50 nm, i.e., 10% of the total film thickness with respect to the virgin Mn_5Si_3 regions. This large swelling effect is attributed to the ion-induced formation of voids in the film at $T_S = 450°C$.

For patterned $Mn_5Si_3/Mn_5Si_3C_{0.8}$ no magnetic contrast was observed in MFM images taken in the remanent state at zero applied field (not shown). Figs. 2(c,d) show MFM images taken in a field of μ_0H = 50 mT applied in the plane along the indicated directions. A magnetic contrast is only observed for micrometer-sized circular features arranged along each border of an implanted area. The features show a dark-bright contrast along the field direction which is inverted after field reversal. Since the MFM tip detects only the out-of-plane force component, the contrast is due to magnetic stray fields arising from domain boundaries. The MFM images suggest that implanted carbon is distributed inhomogeneously and the ferromagnetic phase is nucleated at the border between the carbon-rich and carbon-devoid Mn-Si phase during implantation at 450 °C.

In conclusion, ferromagnetic $Mn_5Si_3C_{0.8}$ and $Mn_5Ge_3C_{0.8}$ films with Curie temperatures well above room temperature have been obtained by $^{12}C^+$-ion implantation. Patterning of initially carbon-free films by ion implantation allows the synthesis of magnetic structures comprised of different magnetic phases. The present work suggests a promising way to obtain lateral magnetic hybrid structures in the micrometer and sub-micrometer range.

[1] C. Zeng, S. C. Erwin, L. C. Feldman, A. P. Li, R. Jin, Y. Song, J. R. Thompson, and H. H. Weitering, Appl. Phys. Lett. **83**, 5002 (2003).

[2] M. Gajdzik, C. Sürgers, M. Kelemen, and H. v. Löhneysen, J. Magn. Magn. Mater. **221**, 248 (2000).

[3] J. P. Sénateur, J.-P. Bouchaud, R. Fruchart, Bull. Soc. Fr. Mineral. Cristallogr. **90**, 537 (1967).

[4] C. Sürgers, M. Gajdzik, G. Fischer, H. v. Löhneysen, E. Welter, and K. Attenkofer, Phys. Rev. B **68**, 174423 (2003).

[5] C. Sürgers, N. Joshi, K. Potzger, T. Strache, W. Möller, G. Fischer, H. v. Löhneysen, Appl. Phys. Lett. **93**, 062503 (2008).

[6] G. Kappel, G. Fischer, and A. Jaéglé, Phys. Lett. **45A**, 267 (1973).

[7] J. B. Forsyth, P. J. Brown, J. Phys.: Condens. Matter **2**, 2713 (1990).

---

[1] Institute for Ion Beam Physics and Materials Research, Forschungszentrum Dresden-Rossendorf, D-01328 Dresden, Germany

Pressure dependent magnetization measurements on CoS_2 and on Co-doped $BaFe_2As_2$

S. Drotziger, K. Grube [1], Th. Wolf [1], H. v. Löhneysen

Macroscopic magnetic order can in a number of systems be suppressed to $T \rightarrow 0$ by variation of a non-thermal control parameter, e.g. chemical composition, pressure, or magnetic field. At this so-called quantum phase transition (QPT) metals can reveal electronic properties inconsistent with Fermi-liquid theory. An important example showing such a behavior is the heavy-fermion compound $CeCu_{6-x}Au_x$ [1]. In addition, the instability of the system at a QPT might give rise to the formation of novel phases like unconventional superconductivity ($CeIn_3$ [2]). To study the critical behavior of QPTs, we measure the order parameter directly, e.g., the magnetization M for ferromagnets. This quantity is also useful to identify a superconducting phase transition.

In order to measure the magnetization as a function of pressure we developed a miniaturized diamond anvil cell (DAC), for pressures higher than those which can be reached by conventional clamp cells. This cell fits into the restricted sample space of a vibrating-sample magnetometer. Up to now only few studies of ferromagnets close to a QPT exist. A particularly promising model system to study quantum criticality is CoS_2 because of its simple ferromagnetic order. As summarized in a previous report [3] we investigated the phase diagram of CoS_2 up to 3.5 GPa. We have now built a new pressure cell, with an improved design and signal-to-background ratio. To reach higher pressures we use diamonds having a larger height-to-diameter ratio [4, 5] to prevent diamond breakage. We grind the diamond seats on a massive sapphire plate to improve the flatness of the diamond seats. Additionally we have replaced the formerly used pressure transmitting medium, a methanol:ethanol mixture by Daphne oil 7373 [6] which has a smaller compressibility. With these improvements we are now able to reach pressures higher than 5 GPa. Figure 1 shows the magnetic phase diagram of CoS_2 up to 4.5 GPa. A first test measurement at 5.2 GPa does not show any hint at a magnetic transition down to 2.5 K. Future measurements will focus on this pressure range to investigate the disappearance of magnetic order.

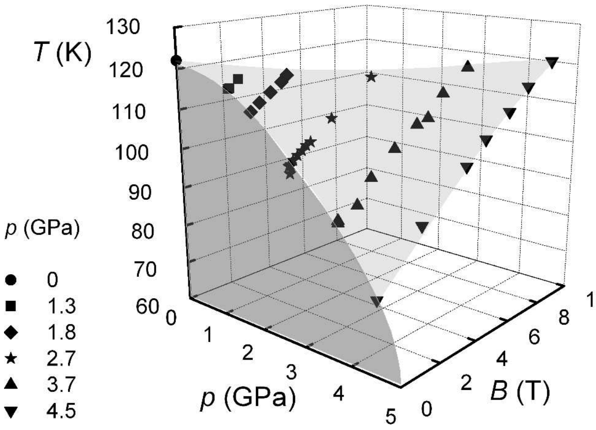

Figure 1: Magnetic phase diagram of CoS_2: In the $B = 0$ plane T_C decreases continuously with increasing p. The onset of the field induced metamagnetic transition shows an almost linear field dependence.

The recently discovered superconductivity in layered iron-arsenide compounds [7] emerges at the onset of antiferromagnetic order, similar to unconventional superconductivity observed in heavy-fermion systems, e.g., $CeIn_3$, but with a higher T_c. In this class of materials the ternary compound $BaFe_2As_2$ is a promising candidate to test the influence of hydrostatic pressure or Co-doping on superconductivity.

The parent compound $BaFe_2As_2$ is a paramagnetic metal and crystallizes in the quasi two-dimensional tetragonal $ThCr_2Si_2$ structure with the space group $I4/mmm$. In this structure layers of edge-sharing $FeAs_4$-tetrahedra are separated by Ba atoms. At $T = 140\,K$ the system undergoes a structural and antiferromagnetic phase transition (SDW) with a symmetry change to orthorhombic $Fmmm$. Electron doping through Co substitution on the Fe sites or the application of hydrostatic pressure induces superconductivity in this compound with a maximum T_c of 22 K [8]. We want to investigate the combined $T_c(x, p)$ behavior to study the interplay between hydrostatic pressure and Co doping.

The Co-doped $BaFe_2Co_2As_2$ single crystals used in this study were prepared with a self-flux method in an alumina crucible [9]. To determine the composition, energy-dispersive x-ray spectroscopy was used, indicating that the Co concentration of the crystal is $x = 0.08$.

We have measured the magnetization of $Ba(Fe_{0.92}Co_{0.08})_2As_2$ as a function of temperature in $B = 5\,mT$ for different pressures. For $p = 0$ the magnetization was measured in a SQUID magnetometer on a larger $Ba(Fe_{0.92}Co_{0.08})_2As_2$

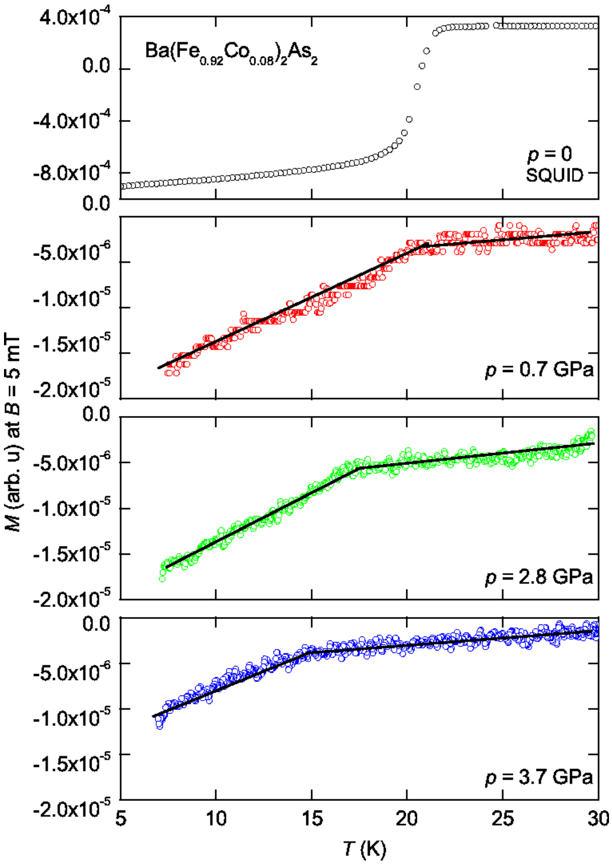

Figure 2: Magnetization M of Ba(Fe$_{0.92}$Co$_{0.08}$)$_2$As$_2$ as a function of temperature T at $B = 5\,\mathrm{mT}$. At $p = 0$ the critical temperature is $T_c \approx 21.4\,\mathrm{K}$. With increasing pressure $p = 0.7, 2.8$ and $3.7\,\mathrm{GPa}$ the superconducting order is shifted to lower temperatures.

single crystal. At ambient pressure the sample has a T_c of 21.4 K. For the pressure dependent measurements we used the DAC with a smaller crystal $0.1 \times 0.1 \times 0.05\,\mathrm{mm}^3$ from the same batch. To cancel the background of the cell we subtracted the field-cooled and zero-field-cooled data. With increasing pressure T_c is shifted to lower temperatures as shown in Figure 2 for $p = 0.7, 2.8$ and $3.7\,\mathrm{GPa}$.

Figure 3 shows the pressure dependence of the superconducting transition temperature obtained from the $M(T)$ curves. The initial pressure effect is $\mathrm{d}T_c/\mathrm{d}p \approx -0.7\,\mathrm{K/GPa}$. This agrees with the results Hardy et al. where the hydrostatic pressure effect $(\mathrm{d}T_c/\mathrm{d}p)_{p=0}$ is estimated to be $\mathrm{d}T_c/\mathrm{d}p \approx -0.9\,\mathrm{K/GPa}$ via the Ehrenfest relation from specific-heat and thermal-expansion measurements [10].

Further magnetization measurements are planned on the parent compound BaFe$_2$As$_2$ and on samples with other Co concentrations in order to investigate the interplay between doping and hydrostatic or chemical pressure in detail.

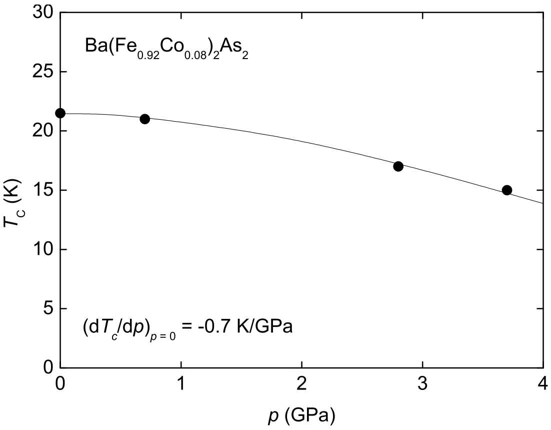

Figure 3: T_c of Ba(Fe$_{0.92}$Co$_{0.08}$)$_2$As$_2$ as a function of hydrostatic pressure p. From a linear fit in the low pressure regime we extracted $\mathrm{d}T_c/\mathrm{d}p \approx -0.7\,\mathrm{K/GPa}$ which is in good agreement with the value given by $\mathrm{d}T_c/\mathrm{d}p \approx -0.9\,\mathrm{K/GPa}$ [10].

[1] H. v. Löhneysen, T. Pietrus, G. Portisch, H. G. Schlager, A. Schröder, M. Sieck, T. Trappmann, Phys. Rev. Lett. **72**, 3262 (1994).

[2] N. D. Mathur, F. M. Grosche, S. R. Julian, I. R. Walker, D. M. Freye, R. K. Haselwimmer, G. G. Lonzarich, Nature **394**, 39 (1998).

[3] S. Drotziger, K. Grube, C. Pfleiderer, M. Uhlarz, H. v. Löhneysen, Annual report, Physikalisches Institut, Universität Karlsruhe (2006).

[4] D. M. Adams, A. C. Shaw, J. Phys. D: Appl. Phys., **15**, 1609 (1982).

[5] K. Syassen, private communication.

[6] K. Yokogawa, K. Murata, H. Yoshino, S. Aoyama, Japan. J. Appl. Phys. **46**, 3636 (2007).

[7] Y. Kamihara, T. Watanabe, M. Hirano, H. Hosono, J. Am. Chem. Soc. **130**, 3296 (2008).

[8] J.-H. Chu, J. G. Analytis, C. Kucharczyk, I. R. Fisher, Phys. Rev. B **79**, 014506 (2009).

[9] A. S. Sefat, R. Jin, M. A. McGuire, B. C. Sales, D. J. Singh, D. Mandrus, Phys. Rev. B **101**, 117004 (2008).

[10] F. Hardy, P. Adelmann, H. v. Löhneysen, Th. Wolf, C. Meingast, arXiv: 0812.4176v1 (2008).

[1] Forschungszentrum Karlsruhe, Institut für Festkörperphysik, D-76021 Karlsruhe.

Magnetic anisotropy in $R\mathrm{Au_2Ge_2}$ (R = Ce and Pr)

V. Fritsch, M. Marz and H. v. Löhneysen

Intermetallic compounds with $\mathrm{ThCr_2Si_2}$ structure have been studied in depth in the past revealing new physics in different areas, e.g. the first heavy fermion superconductor $\mathrm{CeCu_2Si_2}$ [1] and the new high-temperature superconducting Fe pnictides [2]. Further, there is the surprising evolution of spin-glass behavior in the series $\mathrm{PrAu_2(Ge_{1-x}Si_x)_2}$ [3], whose origin is still under debate [4 − 5].

All investigations on the latter material were performed on polycrystals. To our knowledge up to now nobody succeeded in preparing single-crystalline $\mathrm{PrAu_2Si_2}$, although recently a single crystal of $\mathrm{CeAu_2Si_2}$ was prepared [6]. Here we report on the synthesis of single-crystalline $\mathrm{CeAu_2Ge_2}$ and $\mathrm{PrAu_2Ge_2}$ by the flux-growth method in an Au-Ge flux. The starting materials were filled in an alumina crucible and sealed in an evacuated quartz tube which was subsequently heated to 1100°C for four hours. After cooling down with a cooling rate of 10°C per hour to 600°C the flux was separated from the crystals by centrifugation. The crystals were flat plates with a length and width of a few millimeters within the *ab*-plane and an average thickness of half a millimeter along the *c*-axis. We confirmed by x-ray diffraction measurements that the samples where single phase, crystallizing in the well-known $\mathrm{ThCr_2Si_2}$ structure. The lattice parameters were found to be a = 4.3948 Å and c = 10.4635 Å ($\mathrm{CeAu_2Ge_2}$) and a = 4.3729 Å and c = 10.4623 Å ($\mathrm{PrAu_2Ge_2}$), in fair agreement with previously published results on polycrystalline material [7], resulting in a c/a ratio of 2.38 (Ce) and 2.39 (Pr).

The dc magnetization M was measured with a commercial vibrating sample magnetometer (VSM) from Oxford Instruments in the temperature range between 2 and 300 K in magnetic fields up to 12 T. The electrical resistivity was measured with a conventional four-terminal method with a LR-700 resistance bridge in a home-built cryostat in the temperature range between 1.5 and 300 K in magnetic fields up to 6 T.

Fig. 1 shows the temperature dependence of the magnetic dc susceptibility M/B of $\mathrm{CeAu_2Ge_2}$ (upper panel) and $\mathrm{PrAu_2Ge_2}$ (lower panel) in an external magnetic field of 100 mT parallel and perpendicular to the *c*-axis. A strong magnetic anisotropy is found: the measurements with the magnetic field along the *c*-axis show the onset of antiferromagnetic order at T_N = 11.9 K (Ce) and 10.8 K (Pr). These temperatures are slightly smaller than the Néel temperatures found previously on polycrystalline samples (Ce: T_N = 16 K [7], Pr: T_N = 11.9 K [3]). The data for $\mathrm{PrAu_2Ge_2}$ reveal a second transition at 4.3 K. There is no significant difference between field-cooled and zero-field cooled measurements and the application of hydrostatic pressure up to 10 kbar has no effect on the transition temperatures. At high temperatures (100 < T < 300 K) the polycrystalline average of M/H can be fitted with a Curie-Weiss law, resulting effective paramagnetic moments $m_{\mathrm{eff}} = 2.68\ \mu_B$ (Ce) and $3.60\ \mu_B$ (Pr). These values are slightly above the values expected for the free trivalent ions, which may be attributed to a small misorientation of the crystals.

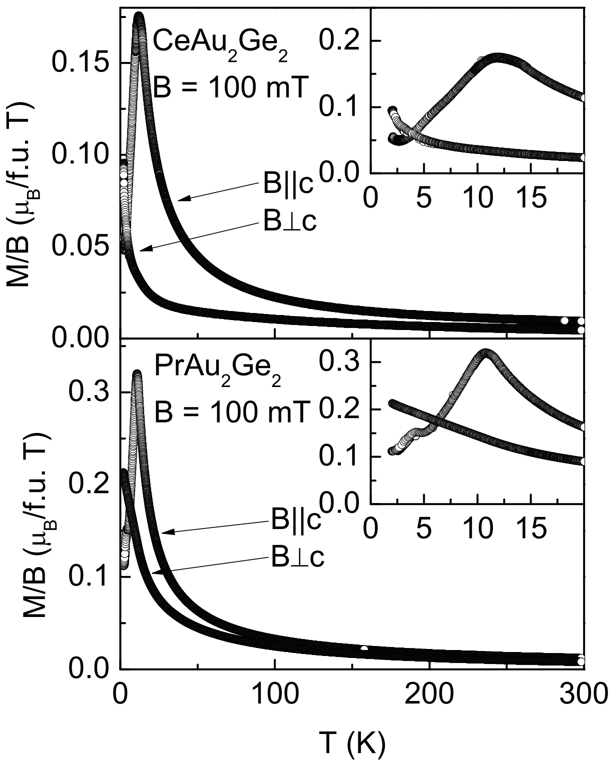

Figure 1: Magnetic dc susceptibility M/B vs. temperature of $\mathrm{CeAu_2Ge_2}$ (upper panel) and $\mathrm{PrAu_2Ge_2}$ (lower panel) in an external magnetic field of 100 mT parallel and perpendicular to the *c*-axis.

The magnetization $M(B)$ of $\mathrm{CeAu_2Ge_2}$ and $\mathrm{PrAu_2Ge_2}$ at T = 2.5 K is depicted in the upper panel of Fig. 2. There is no significant hysteresis around zero field, but the magnetization does not increase smoothly with increasing field. This is visible more clearly in the lower panel of Fig. 2, where M/B vs. the magnetic field is shown. At B = 3.2 T

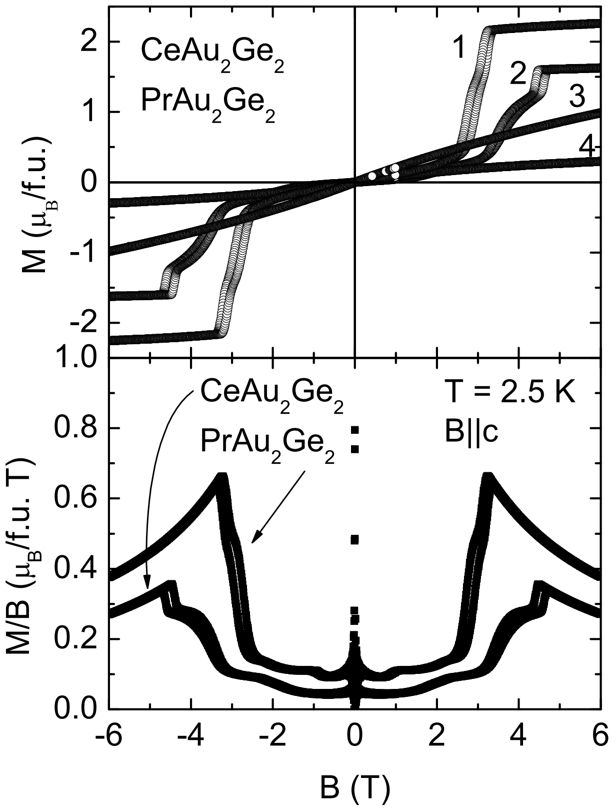

Figure 2: Upper panel: Magnetization of $CeAu_2Ge_2$ and $PrAu_2Ge_2$ vs magnetic field; curve 1: $PrAu_2Ge_2$, $B \| c$, 2: $CeAu_2Ge_2$, $B \| c$, 3: $PrAu_2Ge_2$, $B \perp c$, 4:$CeAu_2Ge_2$, $B \perp c$ at $T = 2.5$ K. Lower panel: M/B vs magnetic field at $T = 2.5$ K with the magnetic field along the c-axis.

(Ce) and 2.5 T (Pr) a steep increase of the magnetization with a small hysteresis indicates a spin-flop transition. This increase is rather broad and displays several steps. At higher fields the magnetization continues to increase slowly further towards saturation.

Fig. 3 presents the temperature dependence of the electrical resistivity of $CeAu_2Ge_2$ (upper panel) and $PrAu_2Ge_2$ (lower panel) in magnetic fields of 0, 1.5 and 4.5 T. At high temperatures in zero field both samples show metallic behavior with a slight concave curvature. There is a sharp upward kink at 14 K for $CeAu_2Ge_2$ and at 11.4 K for $PrAu_2Ge_2$. These kinks are shifted downward slightly in an external field of 1.5 T and vanish in a field of 4.5 T. For $PrAu_2Ge_2$ the temperature of the kink coincides fairly with the Néel temperature found in magnetization measurements. For $CeAu_2Ge_2$ this kink lies a few kelvin above the transition temperature found in the magnetization. While the strong increase of ρ indicates a spin-density wave type of magnetic order with a concomitant gap at parts of the Fermi surface, further measurements are necessary in order to clarify this point.

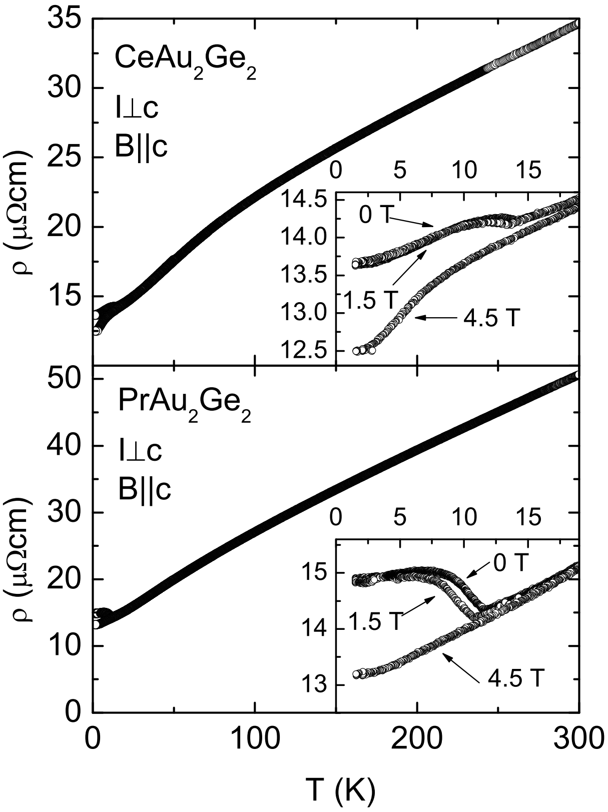

Figure 3: Resistivity of $CeAu_2Ge_2$ (upper panel) and $PrAu_2Ge_2$ (lower panel) in an external magnetic field of 0, 1.5 and 4.5 T.

In summary we have shown that $CeAu_2Ge_2$ and $PrAu_2Ge_2$ single crystals exhibit a strong magnetic anisotropy, which suppresses the magnetic phase transition in certain directions and might possibly provide a clue for explaining for the unusual low temperature behavior of these samples.

[1] F. Steglich *et al.*, Physica B **223 & 224**, 1 (1996).

[2] H.-H. Klauss and B. Büchner, Physik Journal **7**, 18 (2008).

[3] A. Krimmel *et al.*, J. Phys.: Condens. Matter **11**, 6991 (1999).

[4] E. A. Goremychkin *et al.*, J. Magn. Magn. Mater. **310**, 1535 (2007).

[5] E. A. Goremychkin *et al.*, Nature Physics **4**, 766 (2008).

[6] A. Sefat *et al.*, J. Solid State Chem. **181**, 282 (2008).

[7] A. Loidl *et al.*, Phys. Rev. B **46**, 9341 (1992).

Magnetic anisotropy in the layered heavy-fermion compounds $Ce_2M Ga_{12}$ ($M =$ Ni, Pd, Pt)

V. Fritsch, O. Berg, M. Marz, H. v. Löhneysen

The discovery of superconductivity in $CeCoIn_5$, which has the highest T_c of a Ce-based heavy fermion superconductor until today [1], boosted a quest for new layered heavy-fermion compounds in order to deepen the understanding of the role of structure and dimensionality in these materials. In the last years several layered Ce-Pd-Ga alloys were found, including Ce_2PdGa_{12} [2].

We synthesized the series Ce_2MGa_{12} with $M =$ Ni, Pd and Pt by using flux-growth methods [2]. Powder x-ray diffraction confirmed the samples to be of the tetragonal crystal structure [2]. The lattice parameters are given in Tab. 1 and are in fair agreement with the lattice parameters reported previously [2]. Likewise, the magnetic properties of the Pd compound point to the 2-1-12 structure. [2]. On the other hand, atomic absorption spectroscopy measurements (AAS) resulted in a Ni/Ga ratio of 9.8, a Pd/Ga ratio of 9.7 and a Pt/Ga ratio of 13.8. This would yield for the Ni and the Pd compound rather a 2-1-10 structure type [3] than the assumed 2-1-12 structure, while the Pt compound resembles a 2-1-14 stoichiometry. More detailed studies of the crystallography of these compounds are necessary in order to resolve this issue, but for now we assume the 2-1-12 structure.

	Ni	Pd	Pt
a (Å)	6.073	6.089	6.094
c (Å)	15.456	15.542	15.586

Table 1: Lattice parameters of Ce_2MGa_{12}.

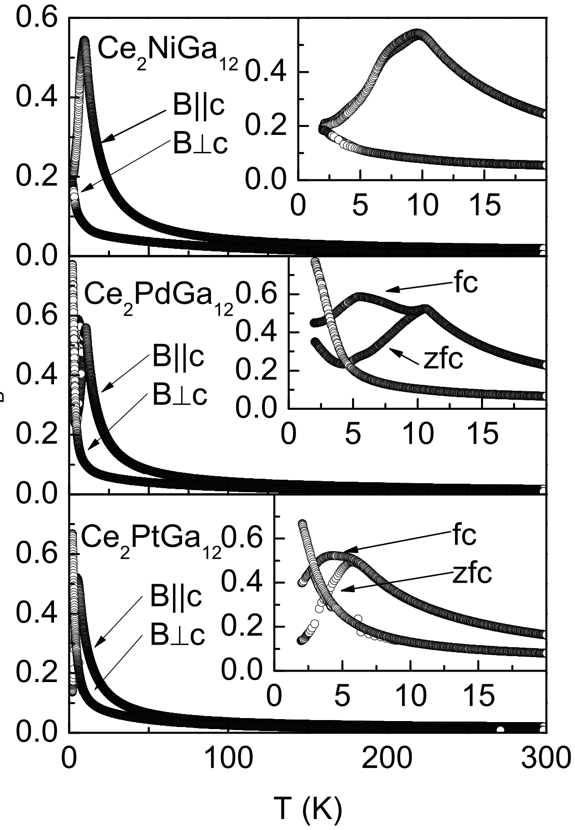

Figure 1: Magnetization M/B vs. temperature of Ce_2NiGa_{12} (upper panel), Ce_2PdGa_{12} (middle panel) and Ce_2PtGa_{12} (lower panel) in an external magnetic field of $B = 100$ mT parallel and perpendicular to the c-axis.

The magnetization M was measured with a commercial vibrating sample magnetometer (VSM) from Oxford Instruments in the temperature range between 2 and 300 K in magnetic fields B up to 12 T. The electrical resistivity was measured with a conventional four-terminal method with a LR-700 resistance bridge in the temperature range between 1.5 and 300 K in magnetic fields up to 6 T.

Fig. 1 shows the dc susceptibility M/B in a magnetic field of 100 mT of Ce_2MGa_{12}. All three compounds exhibit a distinct magnetic anisotropy: with the magnetic field aligned along the c-axis all samples show indications of a magnetic transition at 9.6 (Ni), 10.6 (Pd), and 5.7 K (Pt) respectively. With the magnetic field aligned perpendicular to the c-axis, no magnetic transitions are found. Below the transition the samples with Pt and Pd show a clear difference between field-cooled (fc) and zero-field cooled (zfc) data (see insets of Fig. 1). For antiferromagnetic transitions, no difference between fc and zfc measurements is expected. This point requires further study. A fc-zfc difference is indeed absent in the Ni compound, suggesting antiferromagnetic ordering. The sample with Pd shows an additional peak at 5.6 K in its fc data. These data are in fair agreement with those reported for Ce_2PdGa_{12} [2].

At temperatures above 100 K the polycrystalline average of the inverse susceptibility of the Pt and the Pd sample can be described with a Curie-Weiss law yielding an effective paramagnetic moment of $m_{\mathrm{eff}} = 2.04\ \mu_B$ for Ce_2PdGa_{12} and 1.91 μ_B for

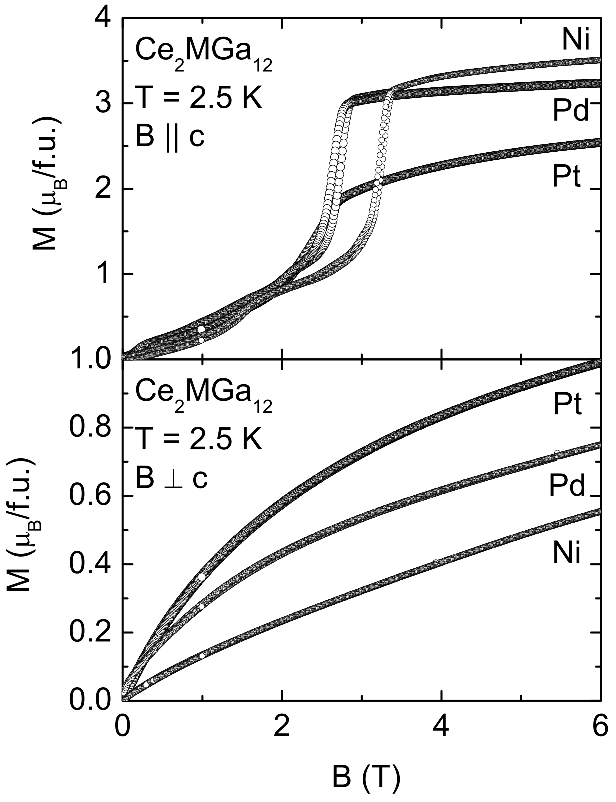

Figure 2: Magnetization M vs. field B of Ce$_2M$Ga$_{12}$ with the field parallel (upper panel) and perpendicular (lower panel) to the c-axis.

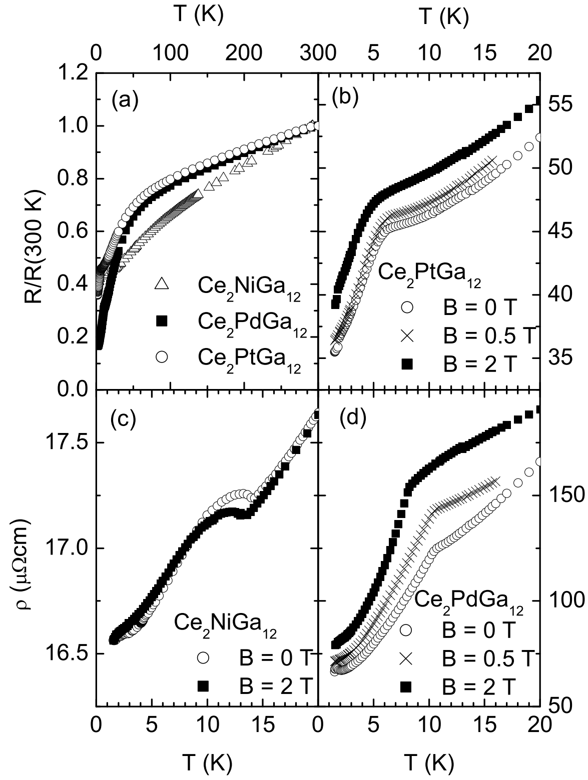

Figure 3: Electrical resistivity $\rho(T)$ of Ce$_2M$Ga$_{12}$: (a) resistivity $\rho(T)$ of all three samples normalized on room temperature values; (b) resistivity $\rho(T)$ of Ce$_2$PtGa$_{12}$ in magnetic fields of 0, 0.5 and 2 T; (c) resistivity $\rho(T)$ of Ce$_2$NiGa$_{12}$ in magnetic fields of 0 and 2 T; (d) resistivity $\rho(T)$ of Ce$_2$PdGa$_{12}$ in magnetic fields of 0, 0.5 and 2 T.

Ce$_2$PtGa$_{12}$. These values are lower than the full moment of trivalent Ce, pointing to a tendency towards intermediate valency of the Ce ions or the presence of crystal field effects.

The field dependence of the magnetization of Ce$_2M$Ga$_{12}$ is depicted in Fig. 2. With the field perpendicular to the c-axis the magnetization increases slowly with increasing field. With the magnetic field aligned along the c-axis the magnetization exhibits a sudden increase at 2.7 T for the compounds with Pt and Pd and 3.4 T for the Ni compound and then increases slowly towards saturation. Note that the absolute values of the magnetization at $B = 6$ T increase from Ni to Pt with the field perpendicular to the c-axis, but vice versa with the field parallel to the c-axis.

The electrical resistivity $\rho(T)$ of all three compounds was measured with the current within the ab-plane and the magnetic field along the c-axis. The results are presented in Fig. 3. All samples exhibit metallic behavior (Fig. 3 (a)). At temperatures below 100 K the resistivities of Ce$_2$PtGa$_{12}$ and Ce$_2$PdGa$_{12}$ bend strongly downwards. In particular, $\rho(T)$ exhibits a downward kink at the ordering temperature with a further decrease below. Application of an external magnetic field results in a decrease of the ordering temperature as can be seen from the susceptibility (not shown) and the resistivity (Fig. 3).

Ce$_2$NiGa$_{12}$ behaves differently: At the magnetic transition a sharp upturn followed by a broader maximum is found. A magnetic field results in a small reduction of resistivity around the Néel temperature. This points to a spin density wave magnetic transition.

[1] C. Petrovic *et al.*, J. Phys.: Condens. Matter **13**, L337 (2001).
[2] R. Macaluso *et al.*, J. Solid State Chem. **178**, 3547 (2005).
[3] J. N. Millican *et al.*, J. Solid State Chem. **177**, 4695 (2004).
[4] Z. Fisk *et al.*, Science **239**, 33 (1988).

Concentration tuning in $\mathrm{CePd_{1-x}Ni_xAl}$ heavy-fermion compounds

N. Bagrets, V. Fritsch, G. Goll, S. Drobnik[1], and H. v. Löhneysen

The ternary intermetallic compound CePdAl crystallizes in the hexagonal ZrNiAl structure with P62m space group [1]. It is a well known heavy-fermion system which orders antiferromagnetically at 2.7 K. Its electronic specific-heat coefficient is $\gamma = 270$ mJ/K^{2}mol. The competition between RKKY interaction and Kondo screening in feavy-fermion system may lead to quantum critical behavior near $T \to 0$, i.e. the system can be tuned to a quantum critical point by applying hydrostatic pressure or by means of doping (chemical pressure).

Specific-heat measurements on CePdAl under pressure [2] have shown that the antiferromagnetic ordering temperature (T_N) is reduced down to 1.7 K under 0.9 GPa. Therefore, it is of interest to investigate the chemical pressure effect in the substituted system $\mathrm{CePd}_{1-x}\mathrm{Ni}_x\mathrm{Al}$. Previous studies [3] have shown that magnetic order disappears at Ni content $x \geq 0.1$. In this report we present results of specific heat C at very low temperatures and magnetization M for $\mathrm{CePd}_{1-x}\mathrm{Ni}_x\mathrm{Al}$ alloys.

The samples were prepared by arc melting of the constituent elements under argon atmosphere. X-ray diffraction measurements confirm a single phase with the hexagonal ZrNiAl structure for all $\mathrm{CePd}_{1-x}\mathrm{Ni}_x\mathrm{Al}$ samples. In order to determine the exact Ni content x, AAS (atom absorption spectroscopy) measurements were performed for each sample as well.

In Fig. 1 the dependence of C/T on T is shown. The transition temperature decreases with increasing Ni content. For the sample with $x = 0.1$ the antiferromagnetic transition is still visible as a weak shoulder in C/T around 1K. So, further measurements will be performed for the sample with $x = 0.12$.

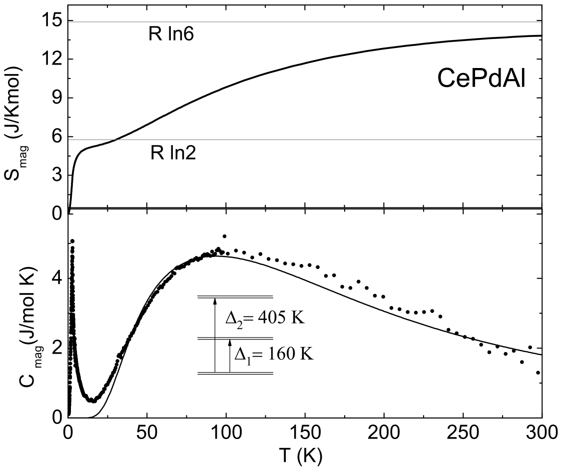

Figure 2: Magnetic entropy and magnetic specific heat versus T of CePdAl. The solid line corresponds to a theoretical fit in paramagnetic phase within the crystalline electric field (CEF) scheme with $\Delta_1 = 160$ K and $\Delta_2 = 405$ K.

From C_{mag} ($C_{\mathrm{CePdAl}} - C_{\mathrm{LuPdAl}}$), we have calculated the magnetic entropy $S_{\mathrm{mag}} = \int_0^T (C_{\mathrm{mag}}/T)\, dT$ which is depicted in Fig. 2 for CePdAl. LuPdAl which has the same crystallographic structure as CePdAl was used as reference compound. We note that the La-based compound, LaPdAl (which serves as a usual nonmagnetic reference system for Ce compounds) has a different crystallographic structure.

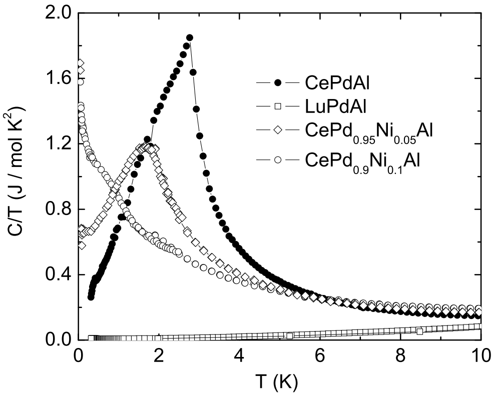

Figure 1: C/T versus T of $\mathrm{CePd}_{1-x}\mathrm{Ni}_x\mathrm{Al}$.

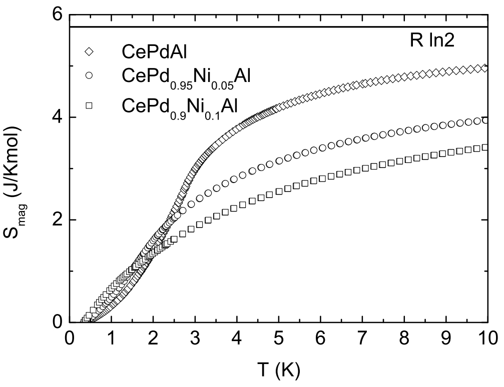

Figure 3: Magnetic entropy versus T of $\mathrm{CePd}_{1-x}\mathrm{Ni}_x\mathrm{Al}$.

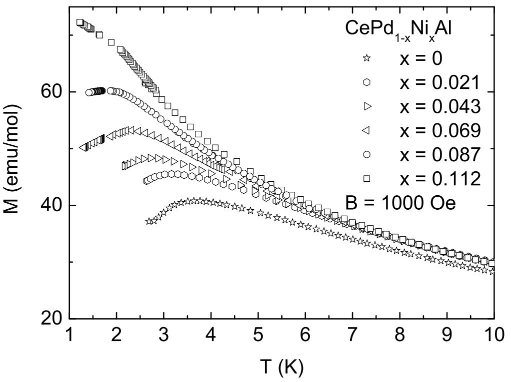

Figure 4: DC magnetization versus T of $\mathrm{CePd}_{1-x}\mathrm{Ni}_x\mathrm{Al}$.

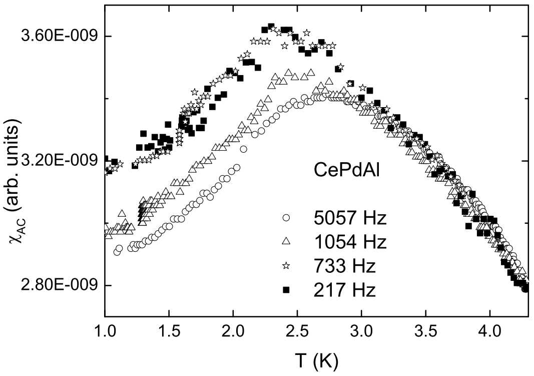

Figure 5: AC susceptibility versus T of CePdAl at different frequencies.

The magnetic contribution to the specific heat C_{mag} exhibits a broadened Schottky-type anomaly around 100 K. Due to the low-symmetry site occupied by Ce^{3+} ion, the $J = 5/2$ ground multiplet splits into three crystal-field doublets. The best fit is obtained assuming that the excited states are separated from the ground state by energy gaps $\Delta_1 = 160$ K and $\Delta_2 = 405$ K.

In Fig. 3 we present S_{mag} versus T at low T for $\mathrm{CePd}_{1-x}\mathrm{Ni}_x\mathrm{Al}$ ($x = 0, 0.05, 0.1$) samples. We note that the entropy at transition temperatures of each sample is smaller than $R \ln 2$, indicating the influence of the Kondo effect.

In Fig. 4 the DC magnetization curves for $\mathrm{CePd}_{1-x}\mathrm{Ni}_x\mathrm{Al}$ samples are shown. Surprisingly, the magnetization of the samples at low T goes up with increasing Ni concentration, whereas T_N decreases. So, AC susceptibility measurements at $B = 0$ for the same samples are necessary.

According to neutron diffraction experiments [4], the Ce moments in CePdAl compound are partially frustrated. For such a frustrated system a metastable behavior is expected. We have therefore performed AC magnetic susceptibility measurements down to 300 mK at different frequencies ω. The transition temperature rises from 2.2 K to 2.8 K with increasing ω from 217 Hz to 5057 Hz, similar to what one usually expects for a spin glass. This result is in good agreement with previous studies [5] on susceptibility measurements for CePdAl down to 2 K.

[1] B. Xue, H. Schwer, F. Hulliger, Acta Crystallogr. C **50** (1994) 338.
[2] J. Tang et al., Physica B **217** (1996) 97.
[3] Y. Isikawa et al., Physica B **281-282** (2000) 365.
[4] A. Donni et al., J. Phys.: Condens. Matter **8** (1996) 11 213.
[5] D.X. Li et al., Physica B **378-380** (2006) 805.

[1] Institut für Festkörperphysik, Forschungszentrum Karlsruhe

Electric field driven ferromagnet-antiferromagnet switching in Fe islands on Cu(111)

Lukas Gerhard, Toyokazu Yamada, Timofey Balashov, Albert F. Takács, Arthur Ernst[1],
Wulf Wulfhekel

Fe is widely used in practical applications ranging from a variety of steels to magnetic power electronics and spin technology. Fe in bulk takes not only various crystal phases depending on temperature (bcc alpha-phase (<1185 K), fcc gamma-phase (1185-1667 K) and bcc delta-phase (1667-1811 K: melting point) at 1 atm), but also various spin states (e.g. ferromagnet, paramagnet, antiferromagnet etc.) depending on slight modifications of the crystalline structure.

Recently, a coexistence of bcc and fcc-Fe structures was found in bilayer Fe islands on Cu(111) [1]. We apply scanning tunneling spectroscopy to investigate the spin structure of the two phases within the islands. We show that the structures have different magnetic states, and that an electric field can drive a phase transition between the two states.

Bilayer Fe islands were grown on a Cu(111) single crystal at room temperature in ultra-high vacuum, and investigated with our homemade low-temperature scanning tunneling microscope (STM). All STM measurements were performed at 4.2 K with clean W tips.

The STM image in Fig. 1 shows a triangular bilayer Fe island on Cu(111). The rim of the island appears about 30 pm higher than the core, and therefore the rim appears brighter in the STM image. The rim and the core have bcc and fcc structures, respectively [1].

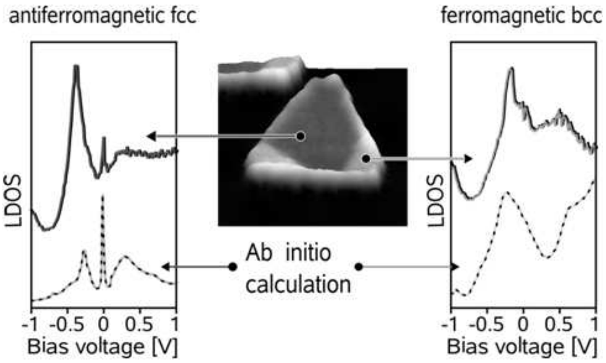

Figure 1: Topographic STM image of a bilayer Fe islands on Cu(111) together with experimental (solid lines) and calculated (dotted lines) LDOS on the rim and the core of the island.

Experimentally obtained LDOS curves from the rim and the core are also shown in Fig. 1 (solid curves). The LDOS at the rim has a peak at -0.3 V, and the LDOS at the core has peaks around -0.4 V, 0 V, and $+0.3$ V. The experimental LDOS were compared with *ab-initio* calculations of the LDOS of Fe bilayers of different magnetic orders. Only the LDOS of a high spin ferromagnetic (FM) bcc structure and LDOS of a layer-wise antiferromagnetic (AFM) fcc structure (dotted curves) fit well to the experimentally obtained LDOS of the rims and the cores, respectively, which proves that the bcc and fcc parts of the bilayer Fe islands have ferro- and antiferromagnetic phases, respectively.

During these STM measurements we found a transition from FM bcc to AFM fcc Fe and vice versa. This transition is manifested by changes of the position of the domain border from line to line in the STM image as shown inside the circle in Fig. 2(a). Figure 2(b) shows an STM image in a line-scan mode obtained at the boundary between FM and AFM phases. A fixed line on the surface was constantly scanned (white line in Fig. 2(a)), the bias voltage was increased row by row from top to bottom of the image and the tunneling current was kept constant. The boundary stays at almost the same position of 4.5 nm up to 0.5 V. However, above 0.5 V, the boundary jumps to a position around 1.5 nm (marked by an arrow in Fig. 2(b)), i.e. the magnetic structure between positions 4.5 nm and 1.5 nm switches from AFM to FM at the critical voltage of 0.5 V. We also found that this critical voltage (U_{crit}) depends on the tunneling current setting. Figure 2(c) shows results of the critical voltages obtained at various currents (I).

Five possible causes for the switching were systematically investigated as follows. (1) The tunneling current, i.e. the number of electrons, might cause the transition by the spin torque effect. In such a case the transition must occur at a certain current (curve 1 in Fig. 2(c)). (2) An inelastic excitation might cause the transition, in such case the transition should happen at a certain bias voltage (curve 2 in Fig. 2(c)). (3) The transition might be caused by the dissipating power during the tunneling. Under a constant power condition the tunneling current is proportional to $1/U$ (curve 3 in Fig. 2(c)). (4) An interaction between tip and sample (overlap of wave functions) might be a cause of the transition, in such

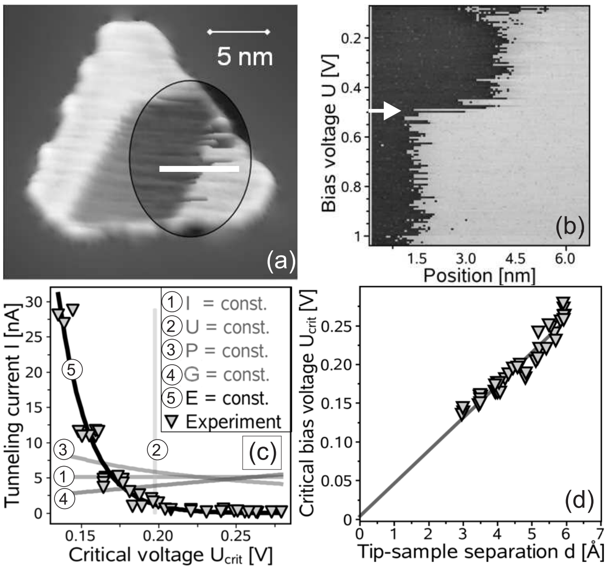

Figure 2: (a) STM image of one bilayer Fe island. The boundary between bcc and fcc areas is unstable. (b) line scan at the white line in (a), where the bias voltage was increased row by row. (c) A dependence of the critical voltage on the tunneling current. Triangles are experimentally obtained data. Five curves show possible candidates to switch the phase. (d) The experimentally obtained critical voltages in (c) are replotted as a function of the tip-sample separation.

case the transition appears at a certain tip-sample separation, i.e. at a constant conductance. Under this condition the tunneling current is proportional to the bias voltage (curve 4 in Fig. 2(c)). All these models do not agree with the observed dependence of the critical voltage on the tunneling current. Finally, (5) a local electric field between tip and sample might be a cause of the transition. Under a constant electric field the bias voltage (U) is proportional to the tip-sample separation (d), thus the tunneling current can be described as $I \propto U \exp(-\sqrt{\Phi} U/E_c)$, where Φ denotes the work function, and E_c the critical electric field (curve 5 in Fig. 2(c)). Only curve 5 in Fig. 2(c) fits, which indicates that the transition is caused by the local electric field.

The experimentally obtained critical tunneling current was replotted as a function of the tip-sample separation by assuming $I = G_0 U$ at $d = 0$, where G_0 denotes a conductance of a point contact, i.e. $I = G_0 U \exp(-\sqrt{\Phi} d)$ (Fig 2(d)). The slope of the curve in Fig. 2(d) gives us an electric field of 0.42 GV/m.

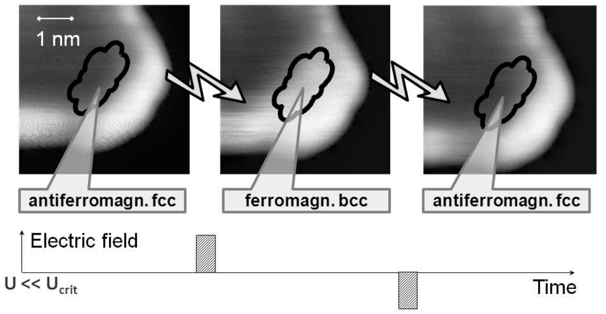

Figure 3: Controlled switching of the magnetic phase by the application of a positive or negative electric field pulse.

We suppose that the switching is driven by magnetoelectric coupling in the Fe islands. Both the experimental results and the theoretical calculations show a difference of the work functions of bcc and fcc Fe of 0.2 eV. The huge electric field under the STM tip couples to the electric field associated with the work function, inducing a crystallographic transition (piezoelectric effect) in combination with the magnetic transition. Such a coupling between electric field and magnetization could be used to control magnetic properties by an electric field or vice versa.

A demonstration of the control of such magnetic switching driven by an electric field can be seen in Fig. 3. Three STM images were obtained from left to right at a much lower bias voltage than U_{crit}, while a pulse voltage larger than U_{crit} (i.e. a huge electric field) was applied after recording each STM image. A positive (negative) field pulse was applied between the first and the second (the second and the third) STM images. The scans clearly show that a darker FM-bcc area before the pulse switches to the brighter (AFM-fcc) phase after the positive pulse and back after the negative pulse. It proves that it is possible to control the magnetic transition by the electric field.

[1] A. Biedermann, W. Rupp, M. Schmid, and P. Varga, Phys. Rev. B **73** (2006), 165418.

[1] Max-Plank-Institut für Mikrostrukturphysik, Weinberg 2, 06120 Halle, Germany

Magnetic anisotropy and magnetization dynamics of individual atoms and clusters of Fe and Co on Pt(111)

T. Schuh, T. Balashov, A. F. Takács, A. Ernst[1], S. Ostanin[1], J. Henk[1], P. Bruno[1], T. Miyamachi[2], S. Suga[2], W. Wulfhekel

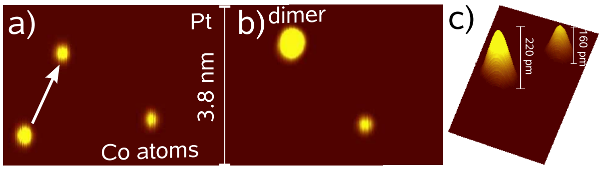

Figure 1: (a) Topography of single Co atoms on Pt(111) (b) Co dimer created by manipulating two Co atoms with the STM [arrow]. (c) 3D view of an atom and a dimer, showing their different topographic heights.

The magnetic anisotropy energy (MAE) is primarily responsible for the magnetic stability of nanoscopic magnetic grains e.g. in hard disks. The microscopic origin of the MAE on atomic scale is, however, not completely understood and has been much discussed recently. Thus, fundamental investigations of the MAE on the atomic scale are necessary. The pioneering study of an ensemble of single Co atoms on Pt(111) was done by Gambardella et al. [1] using x-ray magnetic circular dichroism (XMCD). In that work, a giant MAE of 9.3 meV per atom was reported. We here use a scanning tunneling microscope (STM) to probe the MAE of individual Co and Fe atoms, dimers and trimers on Pt(111), as well as their magnetization dynamics.

For preparation, small amounts of Fe or Co were deposited on an atomically clean Pt(111) crystal at 4.3 K, resulting in isolated atoms. Using the atomic manipulation capabilities of the STM, it is possible to laterally manipulate atoms to form dimers or trimers (Fig. 1b). The dimers—and even more trimers—appear significantly higher than single atoms in topographic scans (see Fig. 1c).

To determine the MAE and the magnetization dynamics of individual atoms and clusters, inelastic tunneling spectroscopy (ITS) was employed at 4.3 K. During the tunneling process, electrons may exchange angular momentum (spin) with the magnetic cluster or atom [2]. As a result of such an inelastic spin-flip scattering, the magnetization direction of the object is changed [3]. For Fe and Co atoms and clusters on Pt(111) the uniaxial anisotropy dominates, favoring a magnetization perpendicular to the surface plane [1, 4]. In the quantum limit, i.e. for an isolated atom or small cluster with spin S, the uniaxial anisotropy energy term can be written as DS_z^2 ($D < 0$). This description is linked to the classical uniaxial MAE $K \cos^2\theta$ by the correspondence principle $\cos\theta = S_z/S$, where θ is the angle of the magnetization with respect to the surface normal. To relate the spin-flip energy E_{sf} of a tunneling electron with spin 1/2 to the MAE, we note that upon spin-flip scattering the magnetic cluster is excited from its ground state with $S_z = \pm S$ to a state with $S_z = \pm(S-1)$, i. e. S_z of the object is changed by 1. When S is known, K can be estimated as $E_{\mathrm{sf}} \times S^2/(2S-1)$ according to the correspondence principle and $|D|(2S-1) = E_{\mathrm{sf}}$. S is calculated using ab initio methods to 3/2 for Fe and 1 for Co. E_{sf} can be measured because the inelastic spin-flip scattering shows up in ITS. For metallic systems, elastic tunneling leads to a linear increase in tunneling current I upon increasing the bias voltage U in the low bias regime. When the energy eU equals E_{sf}, an additional inelastic tunneling channel opens. As a consequence, the slope of $I(U)$ is slightly increased for $eU > E_{\mathrm{sf}}$. This change is usually too small to be identified directly. It can, however, be seen as a peak in $\mathrm{d}^2I/\mathrm{d}U^2$ [5]. The excitation occurs for both tunneling directions such that a negative peak appears at negative bias.

$\mathrm{d}^2I/\mathrm{d}U^2$ spectra were recorded for Fe atoms and the Pt surface (crosses in Fig. 2a). While the spectrum (b) of the Fe atom on Pt(111) clearly shows an 'inelastic' minimum/maximum structure, the Pt spectrum (c) displays a minute signal. The genuine excitation spectrum (d) was obtained by subtracting (c) from (b) and found to be almost symmetric, with the minimum and the maximum reflecting inelastic excitations. An excitation energy of ≈ 6 meV is estimated. The same process for Co atoms on Pt(111) gives very similar results, providing E_{sf} of ≈ 10 meV (Fig. 2e).

Besides the spin-flip excitation, creation of plasmons and phonons as well as a Kondo effect can cause the observed features. For energetic reasons, phonons and plasmons can be excluded. An increase of the magnetic moment due to hybridization with Pt is known to occur for Fe and Co, excluding a Kondo effect.

The excitation energies were measured on a large set of Co atoms and collected in a histogram (Fig. 2g). The distribution fitted with a Gaussian

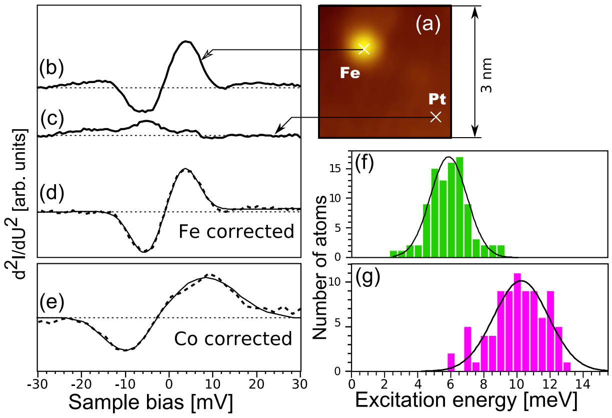

Figure 2: (a) Topography of a single Fe adatom on Pt(111). (b-d) d^2I/dU^2 spectra of an Fe atom on Pt(111) (b), of the bare Pt(111) (c). Background-corrected Fe (d) and Co spectrum (e) (dashed lines) with Gaussian fits (solid lines). Distribution of excitation energies for Fe atoms (f) and Co atoms (g).

yields an average MAE of 10.25 meV per Co atom (see Table 2). Since the spin of Co is 1, the excitation energy directly corresponds to the classical uniaxial MAE. The result agrees well with the experimental observations on an ensemble of Co atoms using XMCD [1], thereby confirming our assumption that the excitation is of magnetic origin.

A similar analysis was performed for an Fe atom on Pt(111). The Gaussian fit gives an excitation energy of 5.83 meV. Collecting the excitation energies from many measurements in the histogram on Fig. 2f and using the correspondence principle, we determine the average MAE of 6.53 meV per Fe atom (Table 2).

Note that the probability for spin-flip scattering determined from the area under the inelastic peaks is about 2% for both Fe and Co when a bias higher than the MAE is used. We further note that the peaks in the tunneling spectra are rather broad due to the short lifetimes. When corrected for experimental broadening, we find lifetimes of the excited states of less than 60 fs for Fe and 24 fs for Co atoms.

Table 2: Spin relationship between measured excitation energies and MAE of Fe and Co atoms and clusters.

cluster	spin transition	excitation energy [meV]	MAE [meV/atom]
Co_1	1→0	10.25±0.15	10.25±0.15
Co_2	2→1	8.2±0.4	5.5±0.3
Co_3	3→2	8.3±1.2	5.0±0.8
Fe_1	3/2→1/2	5.83±0.08	6.53±0.09
Fe_2	3→2	5.98±0.09	5.20±0.09
Fe_3	9/2→7/2	6.5±0.2	5.4±0.2

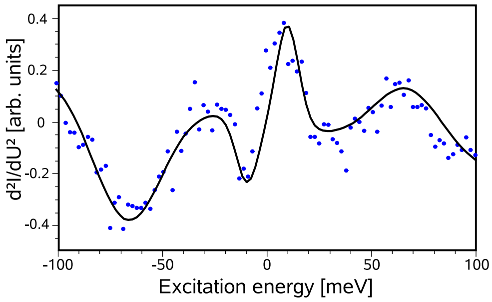

Figure 3: (a) d^2I/dU^2 spectra of an Fe dimer on Pt(111) with two excitations visible. Gaussian fits are shown as solid line.

Exactly the same experiment was done for the clusters, showing similar inelastic excitation features as single atoms. In this case, magnetic atoms couple ferromagnetically such that their magnetic moments align in parallel. A list of excitation energies and corresponding MAEs for Fe and Co clusters is shown in Table 2. In good agreement with XMCD data and calculations [1], the MAE per atom drops with the size of the cluster.

At higher energies, the inner magnetic structure of the cluster can be excited, leading to a non-collinear state. Besides the anisotropy energy, an exchange energy has to be paid in this case. Indeed, we observe high energy excitations as shown in Fig. 3c. They appear as broad peaks around 50 meV for Fe dimers. The width indicates a lifetime of the excited state of 10 fs. A statistical evaluation of 18 measurements of dimers gives an excitation energy of 54 ± 2 meV (Fig. 3b). Assuming a spin of $S = 3$ for a ferromagnetically coupled Fe dimer, the quantum mechanical excitation energy is $3J - 5D$ and J can be determined to 16 ± 1 meV. This is in a good agreement with ab initio calculations which give J = 11 meV. The extremely short lifetime of the non-collinear state is due to the exchange interaction which introduces a decay into a collinear excited state.

[1] P. Gambardella *et al.* Science **300** 1130 (2003)
[2] A.J. Heinrich *et al.* Science **306** 466 (2004)
[3] T. Balashov *et al.* Phys. Rev. B **78** 174404 (2008)
[4] C. Etz *et al.* Phys. Rev. B **77** 184425 (2008)
[5] B. Stipe *et al.* Science **280** 1732 (1998)

[1] MPI für Mikrostukturphysik, Halle, Germany
[2] Graduate School of Engineering Science, Osaka University, Japan

Magnon dispersion in thin films of Co on Cu(100)

N. Urban, T. Balashov, A. Takács, W. Wulfhekel

Physical systems with reduced dimensions can have properties much different than those of the bulk. Examples are thin magnetic films used in modern spinelectronic applications. Unfortunately, not much is known about their magnetic dynamics. The dynamics of the magnetisation is defined, on the lowest level, by the elementary magnetic excitations, i.e. magnons. The established methods of magnon investigation are currently limited to a small part of the Brillouin zone and/or macroscopic samples. Only recently a new technique, spin-polarised electron energy loss spectroscopy, succeeded to measure the dispersion in thin films of Co and Fe on Cu(100) in the plane of the film in the whole Brillouin zone [1]. Now, following the possibility to investigate spin waves in bulk materials with inelastic tunneling spectroscopy (ITS) [2], we have decided to apply this method to thin films.

A film is a two-dimensional system, i.e. magnons can only propagate freely in the plane of the film. In the out-of-plane direction (z axis) the propagation is forbidden, and the system behaves like a quantum well, forming discrete energy levels. Due to the discrete nature of the system along the z axis, i.e. N discrete atomic layers, the number of magnon modes is finite and equal to N. Every mode still has a continuous dispersion in the xy-plane, such that the magnon spectrum consists of N branches. The calculation of the magnon disperion following the Heisenberg model shows, that at the $\bar{\Gamma}$ point, i.e. $q_{\|} = 0$, the discrete modes closely follow the original bulk dispersion, if one assigns a virtual wave vector to each mode in the form

$$q_n = \frac{n}{N} Q_{\max}, n = 0, ..., N-1 \qquad (1)$$

where $Q_{\max}$ is the Brillouin zone boundary in bulk for the z axis direction.

Inelastic excitation of these modes by tunneling electrons in ITS will lead to peaks and dips in the second derivative of the tunneling current I with respect to the bias voltage U. A peak in $\mathrm{d}^2I/\mathrm{d}U^2$ is produced when the energy of the tunneling electron ($\mathrm{e}U$) reaches the energy of an inelastic excitation. A symmetric dip is produced at the negative bias of the same magnitude. In case of a magnon band, only low-$q_{\|}$ magnons will contribute to the spectra [3], so the positions of the peaks and dips correspond to the beginning of the bands. Therefore we expect the inelastic spectra to have several peak-dip pairs, with the amount of features depending on film thickness.

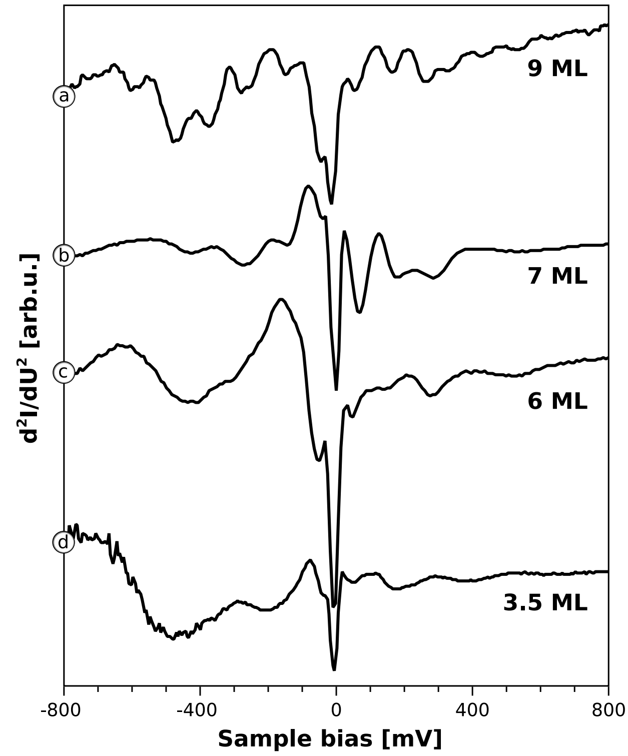

Figure 1: $\mathrm{d}^2I/\mathrm{d}U^2$ curves recorded on Co films of different thicknesses, as indicated. The curves were shifted vertically for clarity.

All the experiments were performed in ultra-high vacuum. Co films 3.5, 6, 7 and 9 monolayers (ML) thick were deposited on Cu(100) at room temperature. As the freshly deposited films of Co are relatively rough, they were annealed up to 370 K. This process was, however, not applied to the thinnest film, as for it a diffusion of Cu through the film occurs. The experiments were perfored in a scanning tunneling microscope at 4.2 K. The inelastic $\mathrm{d}^2I/\mathrm{d}U^2$ spectra were obtained by the lock-in technique at 16 kHz and 5 meV modulation, and averaged over areas of some 100 nm^2.

Experimental curves, presented on Fig. 1, conform to our expectations, as the number of peaks scales with film thickness. The 9 ML film shows approximately 3 times more peaks than the 3.5 ML one, and 6 and 7 ML Co/Cu(100) have a very similar signal shape. The peak intensity decreases with the peak number, while the width of the peak increases.

This means that magnons with higher energy have a shorter lifetime, broadening the peaks. This is expected due to the proximity of high energy modes to the Stoner continuum. At the same time, the width of the peaks changes only slightly with film thickness, when comparing peaks in the same energy region. The peaks are less pronounced in thinner films, that can be attributed to the mean free path of electrons due to magnon creation of about 3 nm [2]. One also notices that all the spectra have a broad dip around -400 meV. For thin films (6 and 3.5 ML) this dip nearly completely hides the less intense structure expected for magnon excitations. Comparing the spectra with the band structure calculation for bulk fcc Co, one can attribute this feature to a majority band edge, appearing at the same energy.

Knowing the energy of the magnons, we can construct the dispersion, by assign wave vector values to every peak, according to (1). However, we cannot exclude the possibility that some of the peaks observed in the spectra are related to features in the density of states. To ensure that the peaks, that we take, correspond to inelastic excitations, we use the symmetry between peaks and dips as the basis for selecting and numbering peaks. The features in the density of states are usually not symmetric, so the peaks, that do not have a partner dip and vice versa, can be rejected.

Matching the peaks and dips proved to be successful for 9 and 7 ML thick films. In thinner films the strong elastic feature in the negative part of the spectra totally hides the dips, so only the right part of the spectra was used. Additional caution had to be exercised with the 3.5 ML film. As this film was not annealed after deposition, it exhibits terraces of 3 and 4 ML local thicknesses. We can expect that if two areas of different thicknesses are connected, magnons will be excited with both sets of energies. And indeed, the spectrum on Fig. 1d shows more than four peaks on the positive side. The negative side is again strongly obscured by density of states features. If we suppose that peaks on the positive side correspond to magnon modes in both 3 and 4 ML, we can construct two dispersions. This is also supported by the fact that spectra taken on different positions on the sample sometimes show that the intensity of some of the peaks increases, decreasing for the others.

The magnon dispersion extracted from all the spectra for different thicknesses is collected in Fig. 2 and compared to the bulk calculation by Pajda *et al.* [4]. Overall, the experiment shows that magnon dispersion in thin films closely follows the bulk dispersion down to 3 ML. The absolute values are, however, slightly lower than for bulk. To compare our results with neutron scattering investigations, we calculated the spin-wave stiffness by fitting the lower part of the dispersion with a parabola. The resulting value of $360 \pm 20\,\mathrm{meV\,Å^2}$ is very close to the previously reported values between 370 and $450\,\mathrm{meV\,Å^2}$. We can conclude that Co films on Cu(100) have bulk-like magnon dispersion, and the magnetism of the films is well-describable by a Heisenberg localised spin model. Note, however, that the dispersion of the thinner film lies systematically below that of the thicker. Although the reduction is small, it indicates the softening of magnons by finite size effects. This can be due to an exchange beyond the nearest neighbour, that has not been taken into account in our model, or to a change of the electronic structure in very thin films.

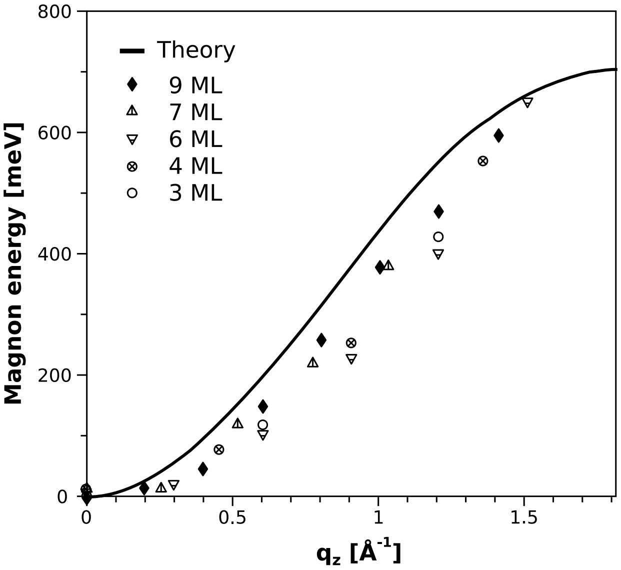

Figure 2: The dispersion obtained from the experimental curves by matching peaks and dips for Co/Cu(100). The solid line is the dispersion obtained by Pajda *et al.* for bulk fcc Co [4].

[1] R. Vollmer *et al.* *J. Appl. Phys.* **95** 7435 (2004)
[2] T. Balashov *et al.* *Phys. Rev. Lett.* **97** 187201 (2006)
[3] T. Balashov *et al.* *Phys. Rev. B* **78** 174404 (2008)
[4] M. Pajda *et al.* *Phys. Rev. B* **64** 174402 (2001)

Measurement of the spin polarisation of Co_2FeSi with Andreev reflection point-contact spectroscopy

S. Bouvron, G. Goll, and C. Felser[1]

With a theoretical spin polarisation of 100 % at the Fermi level, a Curie temperature of 1100 K and a high magnetic moment of $6\,\mu_B$, the ferromagnetic Heusler compound Co_2FeSi exhibits advantageous properties for spin-electronic devices. According to electronic structure calculations, Co_2FeSi Heusler compounds are called half-metallic ferromagnets because they show the behavior of a metal for the electrons of one spin direction, and the behavior of an insulator for the other. The efficiency of spin-electronic devices strongly depends on the spin polarisation P of the transport current. Andreev reflection spectroscopy at ferromagnet (F)-superconductor (S) interfaces has emerged as a simple method for measurement of P [1]. The key idea is to use the sensibility of the Andreev process to the spin of the charge carrier, which occurs at the interface between F and S. Using Andreev-reflection spectroscopy spin polarisation measurements were performed on Co_2FeSi and $Co_2FeAl_{1-x}Si_x$ compounds [2].

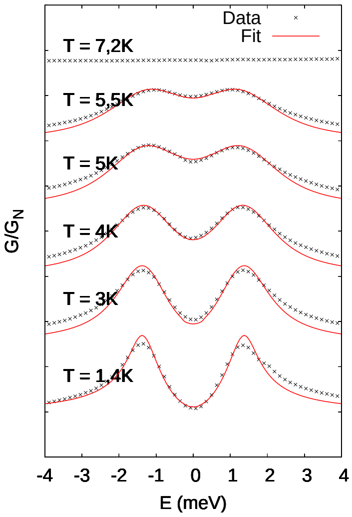

Figure 1: Andreev spectra measured on Co_2FeSi polycrystal for a contact resistance of $R = 12\,\Omega$

Point contacts were realized with the tip-to-anvil method, with a mechanical control of a superconductive Pb tip. The Andreev spectra, i. e. the differential conductance G as a function of the applied bias voltage V, were measured at temperatures $T \geq 1.5\,\mathrm{K}$ and analysed using the Cuevas model [3]. With the approximation that the contact can be characterized by only two spin-dependent transmission coefficients $\tau_\uparrow$ and $\tau_\downarrow$, P is given by $P = (\tau_\uparrow - \tau_\downarrow)/(\tau_\uparrow + \tau_\downarrow)$. P extracted from the measurements is lower than expected from the bandstructure, the measured average value being $P_a = 37 \pm 9\,\%$ for the Co_2FeSi polycrystalline sample. In Fig. 1 the Andreev spectrum of a contact with contact resistance $R = 12\,\Omega$ is shown together with its T dependence.

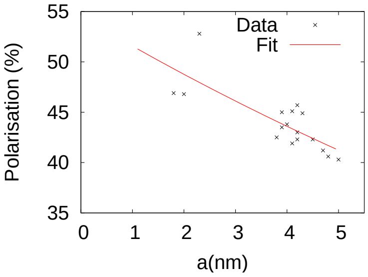

Figure 2: The measured spin polarisation P as a function of the size a of the contact

A decrease of P with increasing contact size a was observed, see Fig. 2, where a was calculated from R using the Wexler formula [4]. A $P(a)$ dependence is not predicted by the theory. An exponential decay of $P(a) \propto \exp -a/l_{so}$ caused by spin-orbit scattering was suggested from measurements on Al-Fe nanostructured contacts [5]. From Fig. 2 we dereived a spin-orbit scattering lenth $l_{so} = 17.9\,\mathrm{nm}$. The substitution of Si by Al in Co_2FeSi compounds shifts the Fermi level within the energy gap of the minority band, that stabilizes the half-metallic behavior of the material for an equal concentration of Si and Al [6]. From Andreev-reflection spectroscopy measurement an average spin polarisation $P_a = 45 \pm 3\,\%$, was observed.

[1] G. J. Strijkers *et al.*, PRB **63**, 104510 (2001)
[2] S. Bouvron, Diplomarbeit, Universität Karlsruhe, 2008.
[3] A. Martin-Rodero, Physica C **352**, 67 (2001).
[4] G. Wexler, Proc. Phys. Soc. **89**, 927 (1966).
[5] M. Stokmaier *et al.*, PRL **101**, 147005 (2008).
[6] G. Fecher and C. Felser, J. Phys. D **40**, 1582 (2007).

---

[1] Institute for Inorganic and Analytical Chemistry, Johannes Gutenberg University of Mainz, 55099 Mainz, Germany

^{75}As-NMR study of the ternary iron arsenide BaFe$_2$As$_2$

G. Fischer and B. Pilawa

The discovery of superconductivity in F-doped LaFeAsO with $T_c = 23$ K [1] has enhanced the interest in the related superconductors. The common feature of these compounds is the possession of FeAs layers which is analogous to the CuO$_2$ planes in high T_c cuprates. In addition, non-doped materials commonly exhibit spin density wave (SDW) or antiferromagnetic order with an adjacent structural phase transition, which also resembles the parent materials of the high T_c cuprates.

Soon after the discovery of the oxypnictides, oxygen-free iron pnictides BaFe$_2$As$_2$ [2] and SrFe$_2$As$_2$ [3] were proposed as candidates of parent materials of superconductors with high T_c. The crystal structure of these pnictides is the ThCr$_2$Si$_2$-type structure which is familiar in the heavy fermion systems. This structure possesses the similar FeAs layer to that realized in LaFeAsO. Moreover, both materials exhibit the SDW anomalies at $T_{SDW} = 140$ K (BaFe$_2$As$_2$) and 205 K (SrFe$_2$As$_2$). It is important to notice that both compounds exhibit a structural phase transition from tetragonal $I4/mmm$ to orthorhombic $Fmmm$ simultaneously with the SDW anomaly [2, 3].

The most striking feature of these compounds is that the SDW anomaly disappears and the superconductivity sets in by hole doping, for example, K substitution for Ba [4] or Sr [5]. In order to understand the superconductivity in these doped oxygen-free iron-based pnictides, it is also important to study the magnetic and electronic properties of the parent materials. Especially the relation between the SDW instability and the superconductivity should be revealed by local-probe measurements in addition to bulk measurements. Hence we performed ^{75}As-NMR and static magnetic susceptibility measurements on Sn-flux grown BaFe$_2$As$_2$ samples [6].

The measurements of the magnetic moments have been carried out with a SQUID magnetometer (MPMS, Quantum Design). The NMR experiments of the ^{75}As nucleus ($I = 3/2$, $\gamma = 7.292$ MHz/T) have been carried out by using a pulsed NMR spectrometer (Bruker MSL 300) and a superconducting magnet (7 T). Temperature was varied between ≈80 K and room temperature using an Oxford Instruments He gas flow cryostat. Typically the fourier transform (FT) of the second half of the NMR spin echo, excited by two radio frequency pulses of 2 and 4 μs length and 20 μs separation, was analysed.

In Fig. 1, we show the temperature dependence of M/H measured on three single crystals (≈4 mg) with the magnetic field oriented perpendicular to the tetragonal symmetry axis. The magnetization follows a Curie-behavior indicating a huge amount of defect spins. This result contrasts with the magnetic susceptibility of FeAs-flux grown BaFe$_2$As$_2$ single crystals which shows the expected temperature dependence of an itinerant antiferromagnet [7]. The SDW anomaly is clearly visible but shifted down to $T_{SDW} = 90(2)$ K. This result agrees with thermodynamic [8] and neutron scattering experiments on Sn-flux grown BaFe$_2$As$_2$ samples [9]. The Ba-atoms are expected to be replaced by a small number of Sn-atoms which modify - nevertheless - considerably the magnetic properties of BaFe$_2$As$_2$.

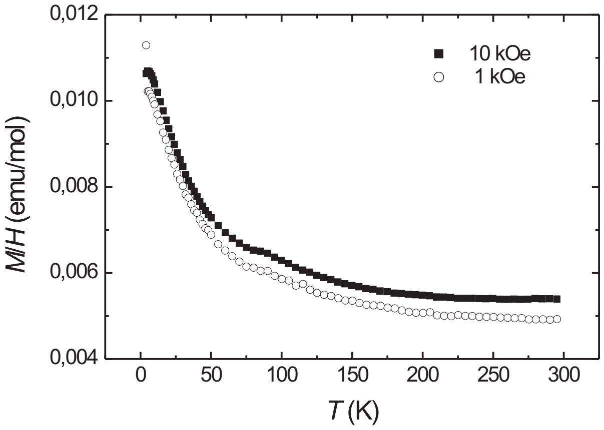

Figure 1: Temperature dependence of the magnetization of Sn-flux grown BaFe$_2$As$_2$ single crystals. The magnetic field was applied perpendicular to the tetragonal symmetry axis.

Spectra and nuclear spin relaxation was measured for ^{75}As of powdered BaFe$_2$As$_2$ single crystals in fixed external magnetic field of $B_0 = 7$ T in the temperature range between ≈ 80 K and room temperature. In Fig. 2a, we show the ^{75}As-NMR spectrum of BaFe$_2$As$_2$ at 100 K in the paramagnetic state. The obtained spectrum is a powder pattern expected for weak electric quadrupole coupling [10]. The rather broad satellite peaks are due to the first-order perturbation effect of the electric quadrupole interaction against the Zeeman splitting. The sharp central peak shown in Fig. 2b was observed at $\nu_0 = 51.6$ MHz. The line shape is due to the second-order effect of the electric quadrupole term. The enhancement of the perpendicular component, which is parallel to the *ab* plane, is due to the partial orientation of the crys-

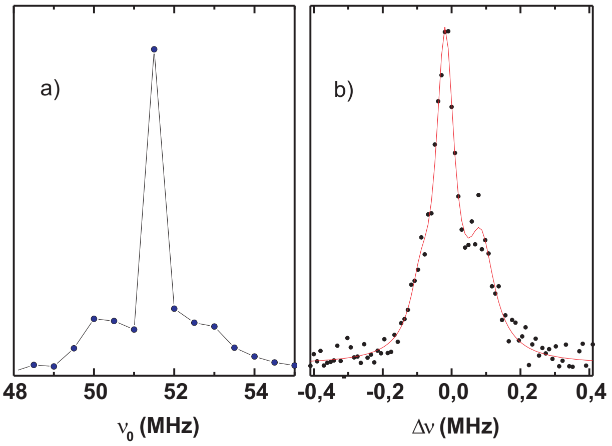

Figure 2: a) ^{75}As-NMR spectrum of poly-crystalline $BaFe_2As_2$ at 100 K. b) central line of the spectrum measured at $\nu_0 = 51.6$ MHz (FT of the second half of the NMR spin echo).

tals in the H_{ext} with decreasing temperature. This suggests that the magnetic easy axis of $BaFe_2As_2$ is within the *ab* plane.

The central line can be fitted by Lorentzian functions. In Fig. 3, we show the frequency shift of the central peak and the perpendicular component of the ^{75}As-NMR of $BaFe_2As_2$ versus temperature. In contrast to the measurement of the magnetic moment shown in Fig. 1, the central peak shifts linearly with temperature. The shift follows the intrinsic magnetic susceptibility of $BaFe_2As_2$ [7] confirming that the static measurement of the magnetic moment is masked by defect spins. The perpendicular component follows the linear temperature dependence down to ≈170 K and turns to higher frequencies in the temperature range of T_{SDW} of FeAs-flux grown $BaFe_2As_2$. This result indicates an increase of the quadrupole interaction well above the SDW-transition of Sn-flux grown $BaFe_2As_2$.

In Fig. 4, we show the T dependence of $1/(TT_1)$ of ^{75}As. The nuclear magnetization recovery curve $M(t)$ was fitted by the double exponential function expected for the center line after the inversion of the $(1/2, -1/2)$ transition, $M(t) \propto exp(-t/T_1) + 9 \cdot exp(-6t/T_1)$ [11]. $1/(TT_1)$ follows the Korringa relation above ≈170 K and increases towards the SDW-transition at $T_{SDW} = 90(2)$ K. Below T_{SDW} $1/(TT_1)$ drops abruptly and the ^{75}As-NMR spectrum becomes very broad.

In summary, we perfomed ^{75}As-NMR measurements in the paramagnetic phase of Sn-flux grown $BaFe_2As_2$. The ^{75}As-NMR spectra clearly reveal a magnetic transition around $T_{SDW} = 90(2)$ K. The measurement of $1/T_1$ shows the critical slowing-down phenomenon, when T approaches T_{SDW}.

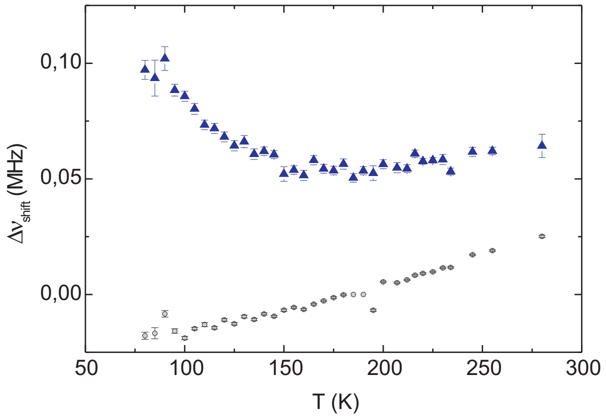

Figure 3: a) Frequency shift of the central peak (dots) and the perpendicular component (triangles) of the ^{75}As-NMR versus temperature.

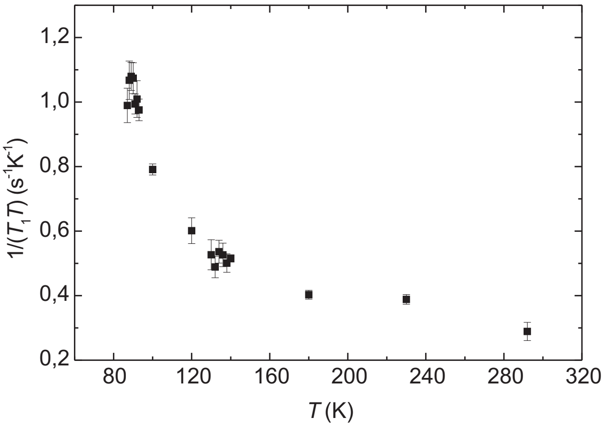

Figure 4: T dependence of $1/(TT_1)$ of ^{75}As.

[1] Y. Kamihara *et al.*: J. Am. Chem. Soc. **130** (2008) 3296.
[2] M. Rotter *et al.*: arXiv: 0805.4021v1.
[3] C. Krellner *et al.*: arXiv: 0806.1043v1.
[4] M. Rotter *et al.*: arXiv: 0805.4630v1.
[5] G. M. Chen *et al.*: arXiv: 0806.1209v1.
[6] Thomas Wolf, IFP, FZ-Karlsruhe.
[7] X. F. Wang *et al.*: arXiv: 0806.2452v1.
[8] N. Ni *et al.*: Phys. Rev B **78** (2008) 014507.
[9] Y. Su *et al.*: arXiv: 0807.1743v1.
[10] G. C. Carter *et al.*: *Metallic Shifts in NMR* (Pergamon Press. 1977 Chap. 2&6.).
[11] W. W. Simmons *et al.*: Phys. Rev. **127** (1962) 1168.

Imaging the vortex-lattice of $NbSe_2$ with a low temperature scanning tunneling microscope

M. Marz, G. Goll and H. v. Löhneysen

A home-built scanning tunneling microscope (STM) was installed into a dilution refrigerator. The setup allows to reach temperatures down to 30 mK and apply magnetic fields up to 13 T. The piezo of the scanning head was calibrated at room temperature on HOPG and $NbSe_2$, where atomic resolution was achieved. At low temperatures single atoms were resolved as well as demonstrated by imaging the topography of $NbSe_2$ [1].

Since Hess et al. [2] showed the first measurements of the vortex lattice on $NbSe_2$ with a STM, this material has become a standard sample for low temperature STM, basically due to the easy and fast way of surface preparation. As on HOPG, the surface can be cleaved with a piece of adhesive tape, obtaining a surface which remains clean for an adequate time period at room temperature and even in air. These properties permit the use of $NbSe_2$ even in non-UHV systems.

The tip was prepared by cutting a 250 μm thick Pt/Ir (80/20) wire in tension with ceramic scissors at an angle of 45°. The sharpness of a tip is tested at room temperature in three steps. First, measurements on a AuPd NanoGrid® [1] are performed, in order to check the lateral resolution by imaging the 160 nm grid structure. It is possible to improve the tip performance by applying cleaning pulses. The second step follows on HOPG, where a good tip is supposed to give atomic resolution. The final step is to achieve atomic resolution on $NbSe_2$. Because HOPG and $NbSe_2$ are layered materials, cleaning pulses will contaminate the tip rather than improve its qualities. After confirming the good quality of the tip at room temperature, the tip is mounted in the STM at a position far away from the sample to avoid damage during the cooldown process. Afterwards, a freshly cleaved sample of $NbSe_2$ is installed.

The assembly of the different components of the cryostat takes several houres, until the pumping on the inner vacuum chamber can be started. To get an acceptable pressure of about $8 \cdot 10^{-4}$ mbar in the inner vacuum chamber one has to wait for one day. To get rid of possible contamination, for example a water film on the surface, we heat the whole STM setup to 100° C while cooling the outer parts, i.e., the magnet, the He dewar and the inner vacuum chamber to liquid nitrogen temperature. Thus, we can expect that nearly all water evaporates from the sample surface and condenses at the wall of the vacuum chamber. For the further cooling down we use clean He as exchange gas until we reach 10 K. The whole cryostat is cooled down to 1 K and the ^{3}He circulation is started before approaching the tip to the sample.

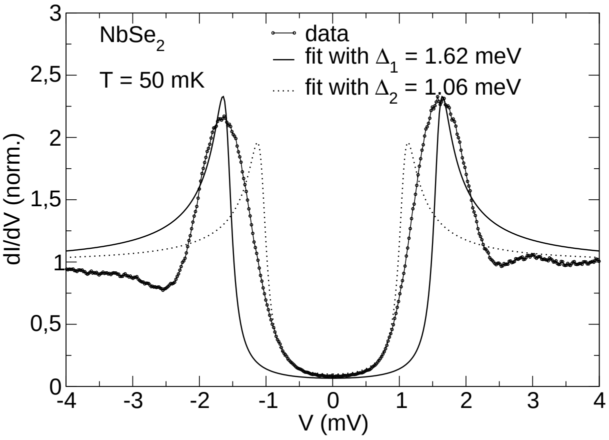

Figure 1: Differential conduction dI/dV vs. voltage V of a $NbSe_2$-Pt/Ir vacuum tunnel contact.

After reaching 50 mK spectroscopic measurements are performed, i.e., we measure the differential conductance dI/dV vs. the voltage V. In order to record the tunneling curves, the tunneling voltage is modulated with an ac bias and the signal is measured with a lock-in amplifier. For low dc bias the superconducting density of state for $NbSe_2$ can be observed. In figure 1 the data taken at one point on the surface averaged over 100 measurements is shown in the voltage range of $|V| \leq 4$ mV with 512 steps in this voltage span. The value of the energy gap can be estimated by fitting the spectra in respect of BTK theory [3] for large Z parameter. As depicted in figure 1 the energy gap determined from a fit of the dI/dV vs. V curves reveals a distribution of the gap depending on the region where one optimizes the fit. By fitting the positions at the maxima, $\Delta = 1.62$ meV is the energy gap obtained, whereas a fit to the width of zero conductance results in $\Delta = 1.06$ meV for the gap. These variations of the gap value are probably due to the presence of the charge-density wave in $NbSe_2$ [4].

---

[1] Commercial available at Schaefer Technologie GmbH

The measurements are relatively slow. Hence some drift of the point where a spectrum is taken can also not be excluded.

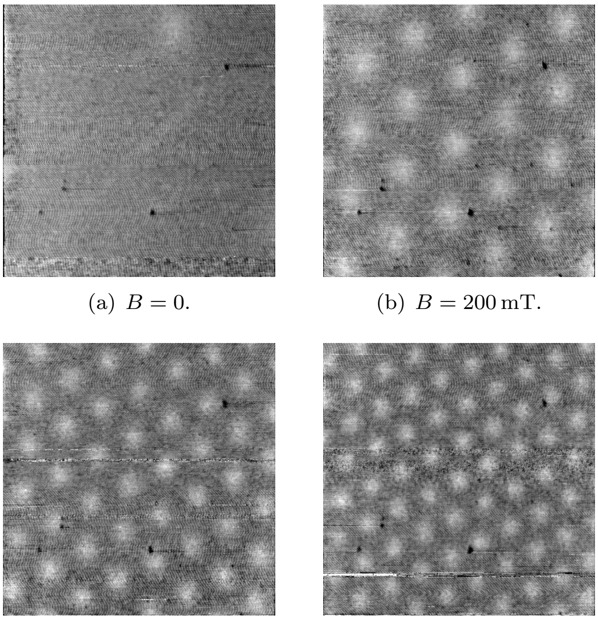

(a) $B = 0$.

(b) $B = 200\,\mathrm{mT}$.

(c) $B = 400\,\mathrm{mT}$.

(d) $B = 600\,\mathrm{mT}$.

Figure 2: STM-Images on $NbSe_2$ in different fields

To observe the flux-line lattice of $NbSe_2$ a small magnetic field is applied. We perform field-dependent measurements of the topography at the voltage corresponding to the maximum of the coherence peak found by spectroscopy without field. In figure 2, STM images of the same region and with the same scanning area acquired in the constant current mode at $V \approx 1.6\,\mathrm{mV}$ are shown for different fields. The image (a) is taken at zero field, but after a field sweep. A trapped one flux line in the upper right corner can be identified. There can still be flux inside the sample either due to a residual magnetization of the magnet or pinning of the flux line at a defect. In image (b) of figure 2, taken at $B = 200\,\mathrm{mT}$, the expected hexagonal structure of the Abrikosov lattice clearly shows up. With increasing field (c and d) an increased density of vortices is recorded. For higher fields $B \geq 800\,\mathrm{mT}$ a strong drift at the lower parts of our measurements occurs. One possible reason for this drift could be a heating of the setup while changing the field, but the drift should then be present also for lower fields. Another possibility is that the measurements are taken too fast after applying the field. For stronger fields the arrangement of the flux lines may take some time until a stable configuration is accomplished. In the pictures (a-c) of figure 2, the overall drift of the scanning area between different scans can be neglected, since characteristic surface defects remain at almost the same positions in every picture. This excludes major shifts due to heating of the sample and/or the tip during field change.

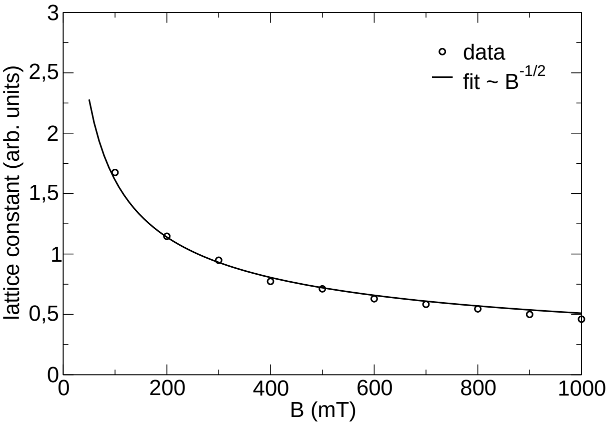

Figure 3: Field-dependance of the lattice constant.

In figure 3 the lattice constant a of the Abrikosov lattice is shown together with the expected field dependence $a \propto 1/\sqrt{B}$ according to Ginzburg-Landau theory [5]. With these data, a calibration of our scanning head at low temperatures for large scanning areas is obtained, while the atomic resolution allows us to calibrate it for small scanning ranges.
In addition, linescans through a vortex were performed. Along the $x-$direction about 150 spectra were taken at different but equidistant points and for the $y-$direction spectroscopy at about 60 points was performed. The spectra clearly show the superconducting density of states in the superconducting regions and the absence of the gap in the normal conducting regions. Moreover we have observed Andreev bound states in the vortex core [6].

[1] M. Marz, G. Goll, Annual Report 2007, Physikalisches Institut, Universität Karlsruhe.

[2] H. F. Hess et al., Phys. Rev. Lett. 62, 214 (1989).

[3] G. E. Blonder et al., Phys. Rev. B 25, 4515 (1982).

[4] I. Guillamon et al., Phys. Rev. B 77, 134505 (2008).

[5] M. Tinkham, Introduction to superconductivity, Dover Publications (2004).

[6] J. D. Shore et al., Phys. Rev. Lett. 62, 3089 (1989).

Surface induced superconductivity of Bi nanowires?

Thomas Kaupp and Georg Weiss

Owing to its large Fermi wavelength and very long mean free paths, Bi is a fascinating metal for studies of transport phenomena in low dimensional systems. We have continued our experiments on the low temperature magnetoresistance of Bi nanowires fabricated by Thomas Cornelius at GSI Darmstadt as electrochemically deposited arrays in polycarbonate foils. Previous experiments [1] explored the influence of the wire diameter on the resistance and the magnetoresistance in a wide temperature range above 1 K. More recently, with our close to single crystalline samples we observed an unexpected reduction of the resistance below 0.3 K [2] which could be reversed in a magnetic field of the order of 50 mT. Here, we like to present a few more detailed results concentrating on the lowest temperature range.

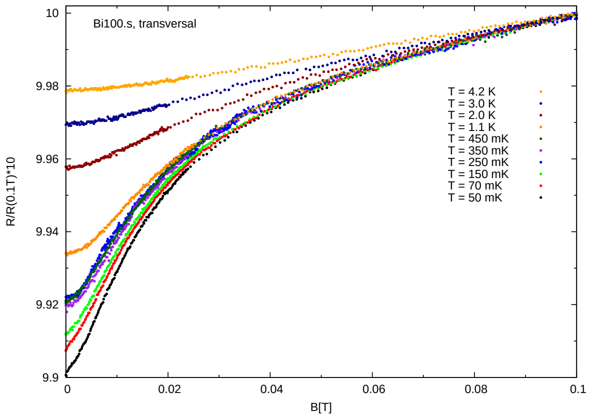

Figure 1: Transverse magnetoresistance of 100 nm diameter, highly textured Bi wires at various temperatures, normalized at $B = 0.1$ T.

Figure 1 shows the relative variation of the resistance of an array of wires with 100 nm diameter as a function of an external magnetic field applied perpendicular to the wire, and thus also to the current direction. The resistance is normalized to its value at $B = 0.1$ T and exhibits a small but characteristic increase with magnetic field of the order of 1% at the lowest temperatures. At higher temperatures this magnetic field effect gradually vanishes apart from a persisting slight further increase which continues to become a $B^{3/2}$ dependence extending to much higher fields as observed previously [1].

For comparison, we also measured the longitudinal magnetoresistance, i.e. with wires parallel to the magnetic field. As shown in figure 2, there is no big difference to the behaviour in a transverse field. The resistance change up to 0.1 T is again of the order of 1% at the lowest temperatures. However, a closer look reveals that higher fields, by a factor of 1.5 as compared to the transverse effect, are required to increase the resistance by the same fraction. Moreover, the resistance variation persisting at high temperatures is considerably smaller. It again develops to a $B^{3/2}$ dependence, which is however much weaker than in the transverse case. Inset of figure 2 shows the resistance variation at lowest temperatures. Up to temperatures of about 0.3 K, the resistance increases rather rapidly and then bends over to a much weaker temperature dependence. We should note that this variation with temperature makes up only a small fraction of about 10% of the total relative resistance change shown in the main body of figure 2.

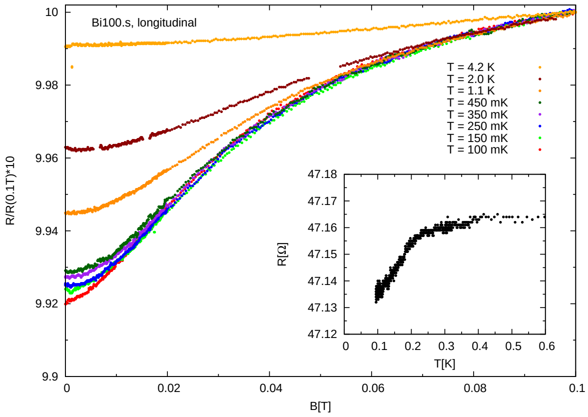

Figure 2: Longitudinal magnetoresistance of the sample of figure 1. Inset shows the temperature dependence of the resistance.

Qualitatively and at first glance, Bi-wires with larger diameters behave similar to the 100 nm wires. There are, however, important differences in detail. The results of our measurements of wires with diameters of 200 nm are plotted in figure 3. The main plot displays the resistance change in a transverse magnetic field. The total relative change is again on the order of 1% but somewhat larger than for the 100 nm wires. More important is the observation that considerably higher fields are required to increase the resistance by a certain fraction. We note also that the resistance variation between 85 mK and 300 mK (see inset of figure 3) has the same size as the variation with magnetic field. The relative resistance change between 300 mK and 4.2 K in zero magnetic field is much smaller than with the 100 nm wires.

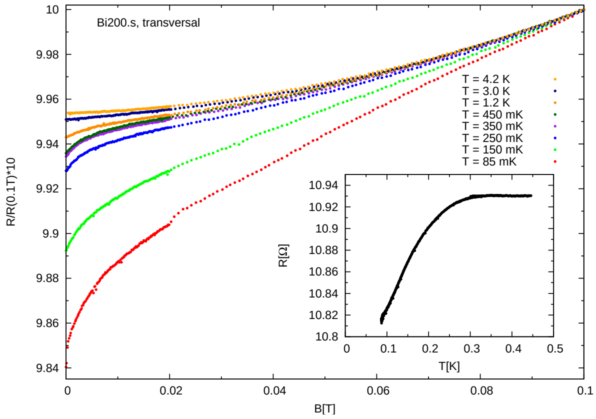

Figure 3: Transverse magnetoresistance of 200 nm wires at temperatures between 85 mK and 4.2 K. Inset shows the temperature dependence of the resistance.

Finally, in figure 4 we show the effect of a transverse magnetic field on the resistance of wires with diameters of 350 nm. Note that the field scale is now larger by a factor of 10 and the asymptotic high field $B^{3/2}$ dependence is more clearly visible. In the low field region, the magnetic fields necessary for a certain resistance increase are now on the order of 0.1 T and confirm the tendency already noticed in the case of the 200 nm wires.

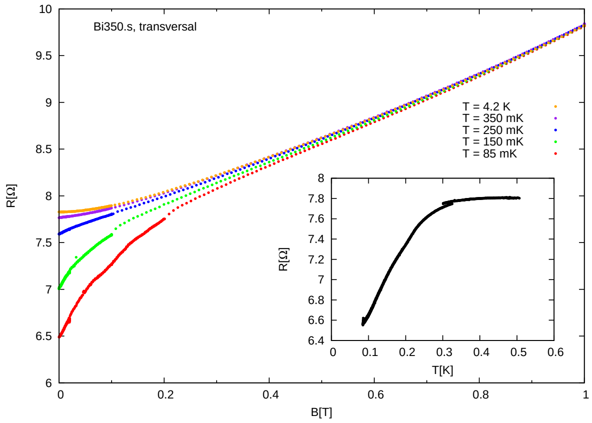

Figure 4: Resistance of 350 nm wires as function of a transverse magnetic field and temperature (inset).

To explain our experiments we could think of two paths, neither of which however turns out to be fully satisfying. Looking at our measurements of the Bi-wires with 100 nm diameter (figures 1 and 2) one is tempted to invoke an effect of weak localization. For Bi, strong spin-orbit scattering would be important and thus weak anti-localization might be expected to decrease the resistance at very low temperatures. Small magnetic fields of the order of 10 mT would suppress this interference effect. In terms of a conductance variation the effect would be of the order of e^2/h and indeed, from the temperature dependence shown in the inset of figure2 we extract $\delta G = \delta R/R^2 \approx 0.3 e^2/h$. However, the agreement ends by looking at the magnetic field dependence. The 1% resistance change corresponds to $5e^2/h$. The measured resistance variations of the 200 nm and 350 nm wires correspond to 25 and over $600 e^2/h$, respectively, and rule out weak localization after all.

The other interpretation scheme is based on the observation that nano-crystalline Bi may become superconducting. This has been reported for granular films built of Bi-clusters aggregated in an Ar beam and condensed onto a cooled substrate. The clusters had a structure close to the bulk structure and, at sizes of about 4 nm, superconducting transition temperatures T_c of 3 to 4 K, getting lower for larger clusters [3]. More recently, superconductivity has been reported in granular Bi nano-wires fabricated by electro-deposition [4]. In this latter case, cluster formation was induced by gelatin added to the electrolyte and T_c values of up to 7.2 K and 8.3 K had been observed, values reminiscent of high pressure phases of Bi.

Our own experiments would suggest that below $\simeq$ 0.3 K more or longer sections of Bi wires successively become superconducting – T_c values which have never been reported previously for Bi of any sample shape. In fact, to our knowledge Bi nanowires with a structure close to single crystalline have never been measured at such temperatures. Following previous discussions [3], we might explain superconductivity as being induced by structural disorder at the surface accompanied by a marked increase of the carrier density. $T_c \simeq 0.3$K for wires with 100 nm diameter are conceivable. On the other hand, for thicker wires where surface effects should have minor influence the 'critical fields' are higher and the resistance reduction below 0.3 K is more pronounced. Although we don't have a complete picture yet, we feel that our observations are finally caused by superconductivity. Surface effects in combination with long mean free paths may play an important role.

[1] Christoph Kaiser, Diplomarbeit, Universität Karlsruhe, 2006; Ch. Kaiser, G. Weiss, T. W. Cornelius, M. E. Toimil-Molares and R. Neumann, to be published

[2] Thomas Kaupp, Diplomarbeit, Universität Karlsruhe, 2007; annual report 2007

[3] B. Weitzel, H. Micklitz, Phys. Rev. Lett. 66, 385 (1991); C. Vossloh, M. Holdenried, H. Micklitz, Phys. Rev. B 58, 12422 (1998)

[4] M. Tian, J. Wang, N. Kumar, T. Han, Y. Kobayashi, M. Ying, E. Thomas, M. H. W. Chan, Nano Lett. 6, 12 (2006)

Scanning probe microscopy imaging of metallic nanocontacts

D. Stöffler, S. Fostner[1], P. Grütter[1] and R. Hoffmann

Molecular electronics has been proposed in order to overcome the size limitations of current silicon-based computer technology. To investigate possible transistor functionality of single molecules, it is necessary to fabricate contacts to the molecules of appropriate size. Different approaches to obtain such nanometer-sized gaps in metallic wires are known, like the break-junction technique or electromigration (EM). The latter approach offers the advantage to potentially produce gaps accessible to scanning probe tips. The electronic properties of the junction during controlled electromigration have been investigated in air [1, 2]. The junction's structural properties have so far been studied with scanning electron microscopy (SEM) techniques. Scanning probe microscopy has the potential for more versatile environments (low temperatures, ultrahigh vacuum - UHV) and preparation techniques. In order to drive a current through the nanostructure, an insulating substrate is required which complicates scanning tunneling microscopy (STM) studies. Using scanning force microscopy (SFM) we have investigated gaps in small metallic bridges fabricated by controlled electromigration in UHV. Concerning the electronic properties, we observe no fundamental difference between the electromigration process in air and in UHV. Conductance plateaus have been observed for conductance values between 30 and 1 $G_0 = 2e^2/h$. The main structure of the resulting gap is formed during the first electromigration cycles. We detect further changes to occur at resistances larger than 12900 Ω with a resolution of 3 nm.

We fabricated metallic nanobridges (Pd, Au) either by e-beam lithography or by shadow evaporation through a nanostructured mask on an oxidised Si substrate. Then we added the macrocscopic leads in the same fashion. We imaged the structures by SEM (Zeiss or JEOL microscopes), UHV-STM (Omicron with Nanonis controller) and UHV-SFM (JEOL with Nanosurf Phase Locked Loop demodulator). In SEM images of Au samples we were not able to resolve any change of the structure after electromigration. In STM images a contamination layer was formed on the sample similar to carbon-rich deposits known from SEM investigations [3]. We therefore transferred the sample immediately after fabrication to the UHV chamber for SFM studies. Here we used commercially available silicon cantilevers with a resonance frequency of about 200 kHz, a typical Q factor of 10000 and a spring constant of 40-50 N/m.

We were able to image the nanostructure by STM inspite of the insulating oxide layer covering the Si substrate using tunneling voltages between 8 and 10 V (Fig. 1a). In scanning probe microscopy, noise at long timescales on the order of a fraction of the time necessary to complete an image is often conveniently removed by subtracting the average of each scan line. If the fast scan axis is chosen to be parallel to the nanowire, such a procedure would lead to an unrealistically small contrast of the nanowire compared to the surrounding part of the sample. If, on the other hand, the fast scan axis is chosen to be parallel to the gap between the macroscopic contact pads, an unrealistically small depth of the gap between the macroscopic contact pads would be observed. Therefore an angle of 45° between the gap and the fast scan axis was chosen.

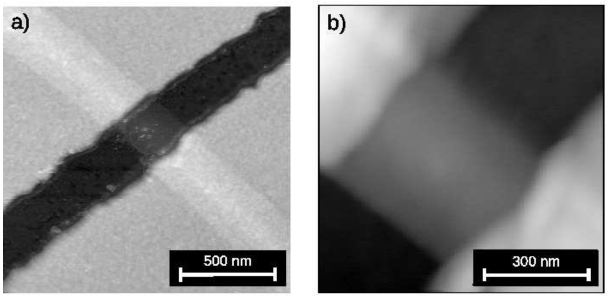

Figure 1: a) STM image of a Au wire ($U_T = 10$ V, $I_T = 0.5$ nA, $\Delta z = 37$ nm) and b) FM-SFM image of a Pd wire ($\Delta f = 0.5$ Hz, $\Delta z = 70$ nm).

For the SFM images we first used frequency modulation mode (FM-SFM) where the cantilever oscillates at resonance with a constant amplitude and the detuning of the resonance upon approach is used as a measure the tip-sample interaction (Fig. 1b). This imaging mode is well-known for highest resolution and is particular advantageous for the high Q factors that are commonly observed under UHV conditions. However, in this mode the stability of the signal was not sufficient for high-resolution imaging at close tip-sample distances in particular when the steep parts of the nanostructure were imaged. Mainly the electronics was not fast enough to keep the cantilever oscillation amplitude constant at the scan speeds necessary to image the relatively large structures within an experimentally accessible time. We therefore used an amplitude-modulation mode (AM-SFM) where the cantilever is oscillated at a constant frequency off-resonance and the reduction

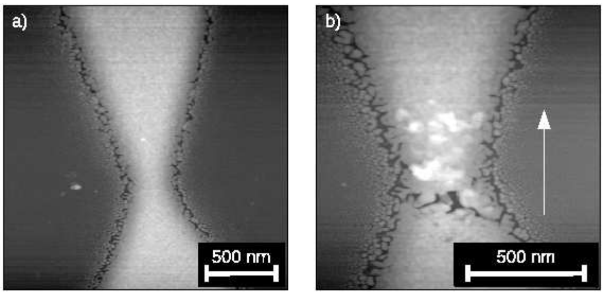

Figure 2: AM-SFM images of Au wire before (a) and after (b) electromigration. The resolution limit is around 3 nm. The initial resistance of the wire was 40 Ω and the electromigration started at around 1.2 V ($\Delta A = 0.2$, $\Delta z = 60$ nm). The arrow indicates the direction of electron flow.

of the oscillation amplitude upon approach is used as a measure of the tip-sample interaction. This became possible by reducing the Q factor of the setup with Q-control technique. In this measurement mode we obtained stable images at closer tip-sample distances, and therefore higher resolution compared to the frequency modulation mode (Fig. 2).

We controlled the electromigration by applying voltage to the samples in cycles. For each cycle, we increased the voltage in steps of 1 mV per 100 ms until the initial resistance increased by 1-6%. Then the voltage was automatically reduced so that the power was decreased to 20% and a new cyle was started. The sample prepared by shadow evaporation (Fig. 2) showed smaller overall initial resistances ($R_0 = 40$ Ω) compared to the samples prepared by e-beam lithography (Fig. 1, $R_0 = 100 - 650$ Ω) due to their different geometry.

In order to study the structural changes of the contact during the controlled electromigration process, the process was stopped after a certain number of electromigration cycles and the SFM tip was approached to the nanocontact. On all samples investigated after 2 - 8 electromigration cycles a crack was formed. One particularly complete measurement is shown in Fig. 2. This sample was prepared by shadow evaporation of 30 nm Au onto a Si substrate covered by native oxide through a nanostructured mask. The bridge had an initial resistance of 40 Ω. We took an SFM image at a total resistance of about 100 Ω (Fig. 2 b). Hillocks have built up following the direction of the electron flow from the crack to the top electrode. These hillocks are expected to build up through the diffusion of metal under the influence of electromigration forces. Along the crack one can see several positions where the sample may still be connected or a small gap may have formed. We stopped the electromigration and took further SFM images at 167, 328, 630 and 12900 Ω, which showed no further structural changes of the contact.

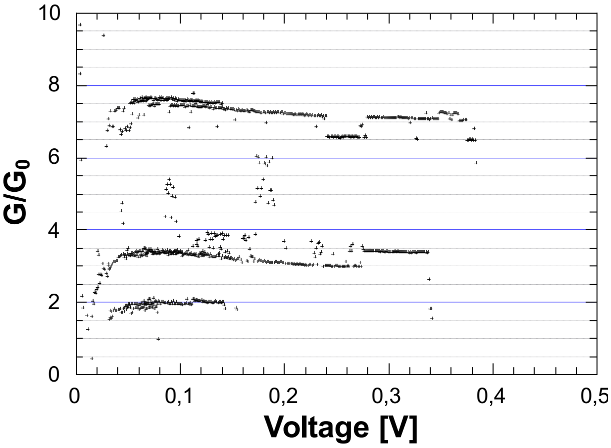

Figure 3: Plateaus in conductance over voltage for the last electromigration cycles for the gold wire.

We estimate the resolution of the SFM images to be about 3 nm. The SFM images acquired at the above mentioned resistances show in retrospect where the electrodes had still been connected. After the last electromigration cycle, when the contact was finally broken, we have imaged a change on the left hand side of the wire. The gold occured to be molten at this point and it ended up due to the cohesion in a sphere, the shape to minimize energy.

In Fig. 3 we plot the conductance for values between 0 and 10 G_0. Plateaus can be seen for certain integer conductance quanta, while others fall between the integer values. We have also observed random telegraph noise, which is often present in nanometer-sized contacts and is related to metastable atomic positions.

[1] D. R. Strachan et al., Appl. Phys. Lett. **86**, 043109 (2005)

[2] R. Hoffmann et al., Appl. Phys. Lett. **93**, 043118 (2008)

[3] D. Stöffler et al., Carbon deposition induced by STM measurements in ultra-high vacuum, this volume

---

[1] Department of Physics, McGill University, Montreal, Canada

Carbon deposition induced by STM measurements in ultra-high vacuum

D. Stöffler, C. Sürgers, H. v. Löhneysen and R. Hoffmann

A common technique to pattern structures down to tens of nanometers is e-beam lithography. The e-beam of a scanning electron microscope (SEM) is used to pattern an organic resist. Then a metallic layer is deposited onto the structure. Finally a lift-off process removes the resist together with the unused part of the metallic layer such that metallic structures are left on the sample surface. Due to the small size of the structures, a characterization by scanning probe techniques is desirable. It is also commonly known that during SEM measurements carbon is often deposit on the sample surface from residual hydrocarbon molecules in the vacuum [1]. This effect can even be exploited in "e-beam contamination lithography" [2]. After e-beam lithography patterning, we have observed the deposition of a possibly carbon-rich substance on platinum and natively oxidized silicon surfaces during STM measurements in ultra-high vacuum. We have imaged the substance with scanning tunneling microscopy (STM) as well as scanning electron microscopy (SEM). The amount of the deposited material increases with the number of scans and the tunneling voltage. Film thicknesses of up to 10 nm with 5 successive STM measurements have been achieved.

We used Si(001) with a native oxide layer as a substrate. We first wrote structures with a commercial Zeiss SEM with Raith e-beam lithography system. Then we treated the sample with methyl isobutyl ketone (MIBK) as developer and electron-beam evaporated a layer of 20-nm-thick metallic layer (Au or Pt) in a high-vacuum evaporation chamber. Between the different e-beam writing, lift-off and evaporation steps, the sample was exposed to air.

In order to attach contacts to the metallic structures on the sample, 100-μm thick Au wires were glued with conductive, UHV-compatible glue (EpoTek) to its surface. These contacts were about 1 mm away from the area scanned in STM images. The sample was then transferred to the UHV-STM with a background pressure $< 1\times10^{-9}$ mbar at room temperature. We used a commercial Omicron LT-STM with Nanonis electronics and a Femto low-noise amplifier for STM imaging.

In spite of the insulating oxide layer on the silicon substrate it was possible to perform STM measurements on the sample, even on areas not covered by metal. We used tunneling voltages between 4 V and 10 V and tunneling currents between 0.1 nA and 0.8 nA and a scan speed of 500 nm/s. On the silicon oxide voltages $\geq$ 8 V were necessary to tunnel through the oxide layer and thus to not crash the tip into the substrate. Current peaks of up to 10 nA occurred repeatedly during the measurement, which we relate to the high voltage and mobile remnants on the surface, which are eventually picked up by the STM tip during the measurement. When we used values of I_T larger than 0.8 nA, we were not able to stabilize the tip position.

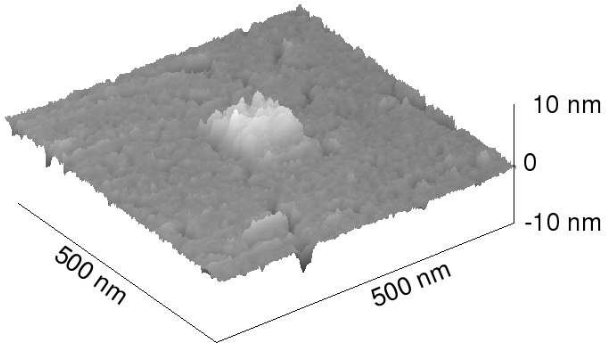

Figure 1: STM image ($U_T = 8$ V, $I_T = 0.1$ nA). The squared hillock was scanned five times with ($U_T =$ 10V, $I_T = 0.5$ nA) and a frame size of 100×100 nm^2.

After a few STM images of the same area we observed the formation of hillocks as well as holes in the metallic layer, in particular on the edges of the gap between the contact pads and along the wire. Although we had thouroughly cleaned the sample with acetone and gaseous nitrogen at the end of the fabrication process it is quite likely that remnants were still present on the sample surface.

To further investigate these structures we acquired several STM images with different parameters. We first scanned five times using $U_T = 10$ V, $I_T = 0.5$ nA and a scansize of 100×100 nm^2 on one particular spot. Then we performed a larger scan with a size of 500×500 nm^2 with $U_T = 8$ V, $I_T = 0.1$ nA, which included the smaller area scanned before. The resulting image showed a hillock with a maximum height of 10 nm (Fig.1). After the STM investigation the scanned areas appeared as regions with a different brightness in subsequent SEM images. Due to the layout of the structures it was possible to identify the region, where we had done the STM scans in SEM images and thus to relate the images obtained by both methods. The structure had not changed or

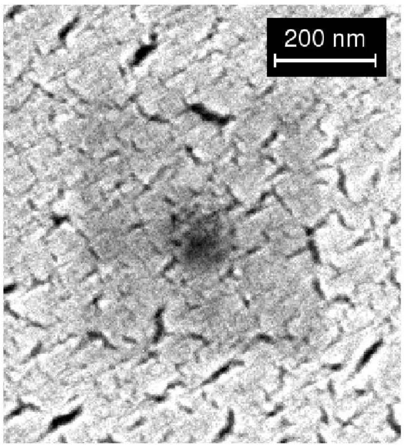

Figure 2: SEM image of the same area where we scanned the STM image in Fig. 1.

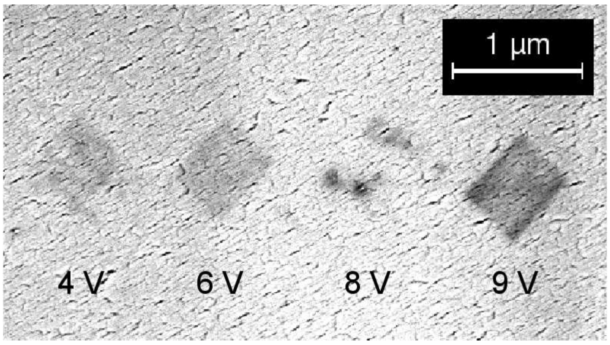

Figure 3: SEM image at 10 keV with in-lens detector. Four STM scanned regions with 500×500 nm^2 at an angle of 45° can be seen as darker regions on the platinum surface. ($I_T = 0.2$ nA).

vanished while transferred in air. Even the 500×500 nm^2 scan was visible as rather homogeneous protrusion (Fig. 2).

We furthermore acquired four scans with different voltages at the same $I_T = 0.2$ nA setpoint at an angle of 45 degrees. The STM images with different tunneling voltages on the platinum regions showed that a decreased voltage results in a less dark window (Fig. 3). Although this points to a voltage dependence, we suspect that it is related to differences in the tunneling current which is easier to stabilize at lower voltages.

We further checked this hypothesis by analyzing the tunneling current in the scan taken at $U_T = 8$ V where strong inhomogeneities of the scanned window are observed. In the brighter regions, the tunneling current fluctuated between 0.2 and 3 nA. In the dark regions, however, large peaks around 8-10 nA appeared in I_T due to stabilization difficulties. This could be related to an inhomogeneous distribution of remnants.

Scans with a fixed $U_T = 9$ V and $I_T = 0.1$, 0.2, 0.4, 0.5 nA appeared similar to each other in the SEM images. We explain this by the fact that the average tunneling current was at a comparable level for all four scans, which we can again relate to the large tunneling voltage and the residues on the surface that cause stabilization problems and peaks in the current.

Scanning tunneling spectroscopy data showed metallic behaviour on both the hillock and the platinum region. Because of the organic molecules which are left over from the fabrication process, and the experience from SEM imaging, we suppose the deposited material to be carbon-rich. The STM current densities are too small to induce melting or even migration of the metal. EDX measurements did not allow us to detect a difference of carbon content between hillocks and the rest of the sample because of the EDX induced carbon. It is well established that platinum binds with carbon [3], e.g., in catalytic processes. However, we have derived qualitatively the same STM-induced topology change on Au surfaces as well. It is futhermore known that STM scans can dissolve photoresists leaving remnants on the surfaces [4]. One group made use of the STM to fabricate nanostructures using hydrocarbons [5].

In conclusion, we showed that during STM measurements on samples produced by e-beam lithography a possibly carbon-rich substance is deposited on the surface, even after thorougly cleaning. This changes the topography and eventually physical properties of the samples. We further showed that the amount of deposited material depends on the tunneling current, which is related to the voltage. Large tunneling voltages and eventually residues on the surface lead to stabilization difficulties and therefore to large tunneling current peaks. The number of scans is also directly correlated to the thickness of the STM-induced layer which can be as thick as 10 nm on a platinum region.

[1] N. Miura et al., Jpn. J. Appl. Phys. **36**, L1275 (1997)

[2] H. W. P. Koops et al., J. Vac. Sci. Technol. B **6**, 477 (1988)

[3] M. Kiguchi et al., Phys. Rev. Lett. **101**, 046801 (2008)

[4] H. Rauscher et al., J. Vac. Sci. Technol. B **15**, 1373 (1997)

[5] T. Mühl, Appl. Phys. Lett. **85**, 5727 (2004)

Switching ferromagnetic Dy break junctions by a magnetic field

M. Müller, R. Montbrun, C. Sürgers, H. v. Löhneysen

In search for conductance switching in atomic-size contacts by a magnetic field, we study the low-temperature electronic transport properties of Dy break junctions. The rare-earth metal dysprosium is paramagnetic at room temperature. Between 87 and 179 K the magnetic moments are arranged in a helical fashion and below 87 K Dy becomes ferromagnetic. Dy has a huge saturation magnetostriction λ_s of the order of 10^{-2}. This is about 1000 times larger than for Fe, Ni and Co [1].

In previous diploma theses [2,3] nanostructured samples were prepared. However, in those samples no switching of the atomic contact between "open" and "closed" states was observed when sweeping the applied magnetic field. In the present work, thin wires of 0.3 x 0.3 mm^2 and 1 cm length were cut from a bulk Dy polycrystal. A notch was cut in the middle of the wire as a predetermined point at which the sample breaks during bending of the copper-bronze substrate. The wire was glued to the substrate with GE varnish in a way that the notch lies exactly in the middle of the substrate. Before fixing everything with stycast, the Dy wire was connected to four copper leads in order to perform four-point-probe measurements.

All measurements were done in a ^{4}He bath cryostat at $T = 4.2$ K. Breaking of the Dy wire was accomplished by means of a three-point bending mechanism. For this purpose the substrate is fixed at both ends on the sample holder and a threaded rod is pressed against the backside of the substrate directly under the predetermined breakage point. The rod can be moved forward and backward by a computer-controlled electromotor. By pushing the rod, the substrate and the Dy wire are bent until the wire finally breaks. During breaking the wire the electrical resistance is monitored by measuring the sample voltage at fixed current. After breakage it is possible to switch the wire several times between the states "open" and "closed" by moving the pushing rod forward and backward. Fig. 1 shows the wire resistance R vs. the motor position, i.e., vs. the electrode distance. A large hysteresis is observed. In the "open" state, the measured resistance is limited by the maximum range of the voltmeter. Hence, $R > 3.33\,\mathrm{M}\Omega$. A resistance of $R < 200\,\Omega$ represents the "closed" state.

From the hysteresis width of about 1026 motor positions one can estimate the separation d between the two Dy electrodes by taking into account the gear transmission ratio, the pitch of the threaded rod etc. The calculated value of $d = 2.38$ nm corresponds to approximately 7 Dy atom distances. The formation of such a long chain of atoms is very unlikely. It is more likely that after breakage the atoms rearrange in a different fashion. Hence, the way back to contact of the two electrodes is longer than before opening the contact.

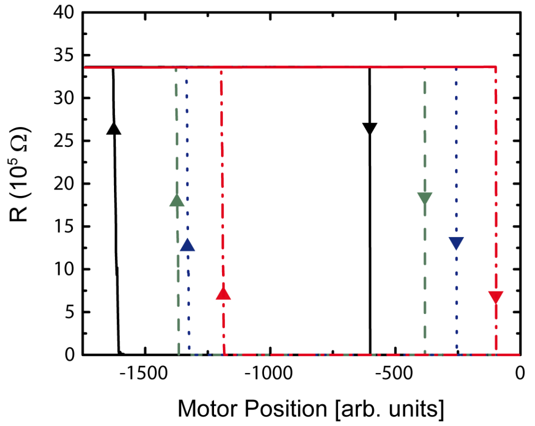

Figure 1: Hysteresis loops of resistance R vs. motor position, i.e. electrode distance. The measured maximum resistance is limited by the experimental setup, see text.

For the experiments in an applied magnetic field H the wire was first broken mechanically. The magnetic field was applied along the wire axis. In a pretuned position where the contact just opened, the magnetic field was increased and the resistance was recorded. Fig. 2 shows that the contact resistance changes from high to low resistance with increasing field. This behavior is due to the positive magnetostriction $\lambda_s > 0$ of Dy which leads to an elongation of the two electrodes and closure of the contact. The contact opened again upon decreasing the magnetic field, with a hysteresis of ~ 0.15 T, see Fig. 2.

So far it is possible to switch the wire between "open" and "closed" states with a typical hysteresis of ~ 0.1 T. In addition to the observation of magnetic switching, a step-like behavior of the conductance $G(H)$ with conductance plateaus can be observed resembling the behavior reported earlier by tuning the distance between two metal electrodes mechanically either by an STM [4] or by the break-junction technique [5]. For magnetic-field tuning, it is important that the electrode distance can be changed contin-

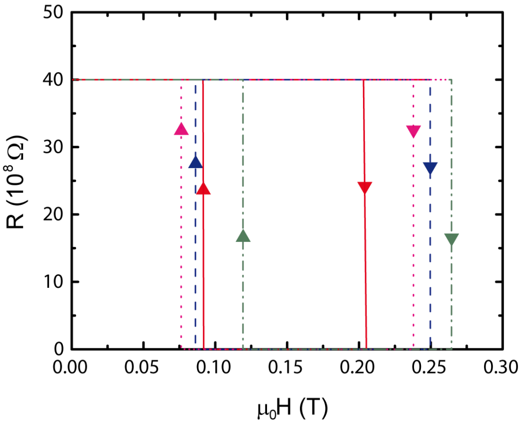

Figure 2: Hysteresis loops of $R(H)$ due to a change of the electrode separation by a magnetic field. The measured maximum resistance is limited by the experimental setup, see text.

uously in a magnetic field. Therefore, the magnetic field has to be applied along a magnetically hard axis to avoid jumps in the electrode distance when the magnetization of the sample switches at the coercive field. Fig. 3 shows the magnetization $M(H)$ at $T = 4.2$ K with the magnetic field applied along the wire axis. The S-like shape of the hysteresis clearly shows a smooth $M(H)$ and hence $\Delta l/l$ dependence in the field range where the switching behavior in $R(H)$ is observed, see Fig. 2.

Fig. 4 shows measured conductance curves G/G_0 vs. magnetic field, where G is the conductance and $G_0 = 2e^2/h = 7.746 \times 10^{-5}\Omega^{-1}$ is the conductance quantum, with distinct steps and plateaus. This step-like behavior was observed for at least four different samples measured in two different experimental setups. The right-hand curve was measured while closing the contact, the left one while opening it again. Unfortunately, we did not record enough data of the samples to get sufficient statistics for a reliable histogram of the number of events vs. conductance. In a preliminary histogram the number of 250 counts for the largest peak is very small compared to histograms using mechanical tuning.

In summary, we demonstrated that Dy break-junctions can be switched by sweeping an applied magnetic field. In a mechanically preadjusted and fixed position of the two electrodes, the contact can be opened reproducibly and closed by variation of the applied magnetic field. The switching, i.e., the change in resistance vs. contact distance, shows a hysteretic behavior and presumably arises from the large magnetostriction of ferromagnetic Dy. In addition, a step-like behavior was observed in several

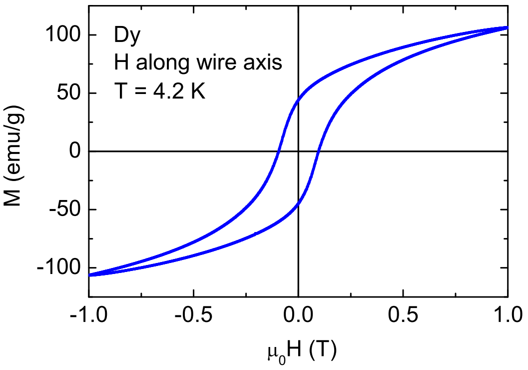

Figure 3: $M(H)$ hysteresis curve of Dy with H applied along the wire axis.

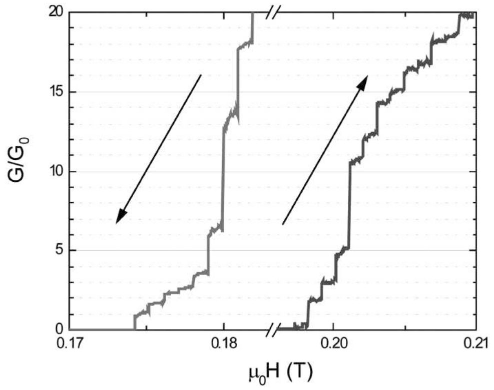

Figure 4: Conductance curves with steps and plateaus for increasing (contact closes) and decreasing fields (contact opens). The arrows represent the variation of the magnetic field - increasing or decreasing - during the measurement.

different samples and two different experimental configurations. In the future, we will aim at measuring the angular dependence of the $R(H)$ behavior in order to explore magnetostrictive effects in metallic nanocontacts in detail.

This work was supported by the DFG Center for Functional Nanostructures (CFN).

[1] F. J. Darnell, Phys. Rev. **132**, 128 (1963)
[2] P. Jaroljmek, Diplomarbeit, Physikalisches Institut, Universität Karlsruhe (2004)
[3] D. Kaufmann, Diplomarbeit, Physikalisches Institut, Universität Karlsruhe (2006)
[4] M. Brandbyge, Phys. Rev. B **52**, 8499 (1995)
[5] N. Agrait, A. Levy-Yeyati, J.M. van Ruitenbeek, Phys. Rep. **377**, 81 (2003)

Measurement of the spin polarisation of the transport current through nanostructured Nb/Fe point contacts

K. Mirlin, G. Goll, and C. Sürgers

The analysis of Andreev reflection in superconductor/ferromagnet point contacts has been widely used to extract the current spin polarisation in a variety of materials. The theoretical analysis of these point-contact Andreev reflection experiments has been mainly carried out in the spirit of the Blonder-Tinkham-Klapwijk theory [1] for Andreev reflection at an interface between a normal metal and a classical superconductor with spin-singlet pairing. The sensitivity of the Andreev process to the spin of the carriers originates from the spin content of a Cooper pair (S = 0 in conventional superconductors) and the conservation of the spin direction at the interface. In a spin-polarized situation this leads to a reduction of its probability [2]. An issue of considerable importance is how the current spin polarisation obtained by Andreev reflection is related to the ferromagnet's bulk spin polarisation. In a previous experiment we showed that spin-orbit scattering reduces the current spin polarisation in nanostructured Al/Fe point contacts and it is most effective in large contacts [3]. We used Andreev reflection to study nanostructured Nb/Fe point contacts as spin-orbit scattering is expected to be stronger for Niobium.

Nanostructured Nb/Fe point contacts were fabricated by structuring a hole of 5 - 10 nm diameter into a 50- nm thick Si_3N_4 membrane, evaporating on the "hollow" side a 200 nm Nb layer, and on the other side a 12-nm thick Fe layer topped by a Cu layer of thickness $d_{Cu} = 188$ nm serving as a low-ohmic electrode.The point contacts were produced by electron-beam lithography, followed by plasma-etching and evaporation of the metals on the substrate in a ultra-high vacuum chamber. Nb was evaporated at elevated temperatures in order to get a better film quality with higher superconducting transition temperature. The measurements of the Andreev spectra, i. e. the differential conductance as a function of applied voltage were done in a ^{4}He cryostat down to 1.5 K [4].

The spectra have been analyzed using the Cuevas model [5]. This model is based on the Landauer-Büttiker formalism with the approximation of using only two spin-dependent transmission coefficients $\tau_{\uparrow(\downarrow)}$ for all transport channels. The polarisation is given by $P = (\tau_\uparrow - \tau_\downarrow)/(\tau_\uparrow + \tau_\downarrow)$. The spin dependent transmission coefficients $\tau_{\uparrow(\downarrow)}$ are evaluated from the measured Andreev spectra using the Cuevas model.

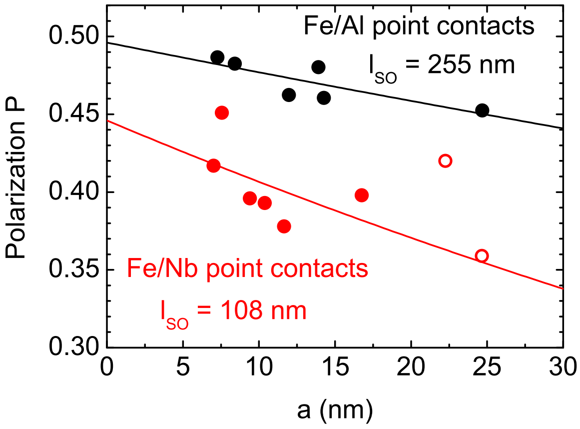

Figure 1: Dependence of the current spin polarisation on the contact radius. The solid line shows $P = P_0 \exp(-a/\ell_{SO})$ with $\ell_{SO} = 276$ nm for Al/Fe and $\ell_{SO} = 108$ nm for Nb/Fe contacts. Filled symbols for Nb/Fe are data taken from literature [7], open symbols are from present work [4]. Data for Al/Fe are taken from Ref. [3].

We observed a decrease of the polarisation P with increasing contact size a, see Fig. 1, whereas a was calculated from the resistance R using the Wexler formula [6]. An exponential decay of the polarisation, given by $P(a) \propto exp(-a/l_{SO})$, and caused by spin-orbit scattering was suggested earlier after measurements on Al/Fe point contacts [3]. This scenario is supported by a larger decrease of P for Nb/Fe contacts compared to Al/Fe contacts, as expected for spin-orbit scattering.

[1] G. E. Blonder, M. Tinkham, T. M. Klapwijk, Phys. Rev. B **25** (1982) 4515

[2] M. J. M. Jong and C. W. J. Beenakker, Phys. Rev. Lett. **74** (1995) 1657

[3] M. Stokmaier *et al.*, Phys. Rev. Lett. **101** (2008) 147005

[4] K. Mirlin, Diplomarbeit, Universität Karlsruhe (2008)

[5] A. Martin-Rodero, Physica C **352** (2001) 67

[6] G. Wexler, Proc. Phys. Soc. 89, 927 (1966)

[7] G. J. Strijkers *et al.*, Phys. Rev. B **63** (2001) 104510

Design and construction of a 500 mK Scanning Tunneling Microscope

L. Zhang, R. Dehm, W. Wulfhekel

In many investigations of nanoscopic structures, both a high lateral resolution and a high energy resolution for electronic states is required. Typically, this requirement is solved by using a scanning tunneling microscope (STM) operated at cryogenic temperatures. For surface science studies of atomically clean structures, the STM needs to be operated in ultra high vacuum (UHV) and should allow simple exchange of sample and tip without breaking the vacuum. Commercially available solutions exist for such STMs operated at 4.2 K using a He-bath cryostat. A high mechanical stability has been achieved routinely allowing atomic resolution and thermal drifts below 1Å per hour.

The energy resolution ΔE obtainable in inelastic scanning tunneling spectroscopy (ISTS) at the temperature T is 5.4 $k_B T$ [1] and thus at 4.2 K only about 1.9 meV. This is insufficient for many detailed studies of magnetic excitations in ferro- or antiferromagnets as well as quasiparticle excitations in superconductors, thus requiring lower operation temperatures. To achieve this, an entirely homebuilt STM including a He^3 cryosystem was developed and built at the Physikalisches Institut. Special care was taken that the consumption of cryogenic liquids stays low and that the vibrational level of the instrument at the STM tip is below 300 fm.

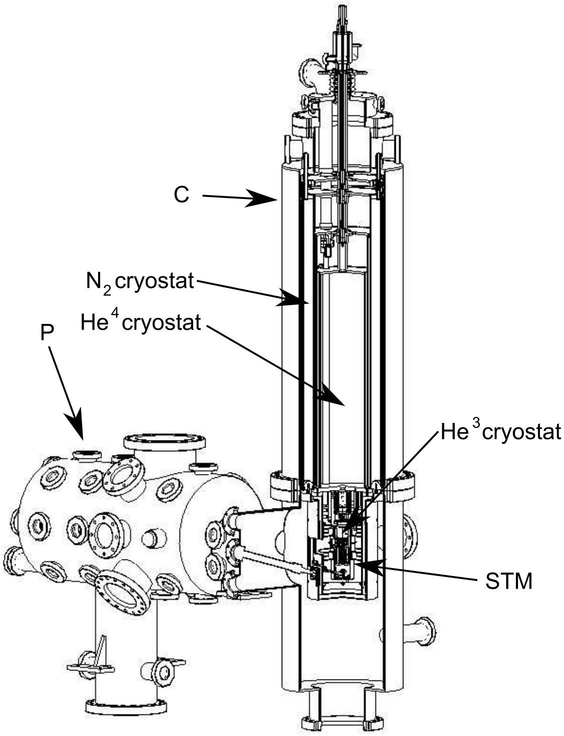

Figure 1: Layout of the UHV recipient with the preparation chamber (P), the cryostat chamber (C), and the STM. The cryostat consists of a liquid nitrogen, a liquid He^4 and a Joule-Thomson stage running with He^3.

Figure 1 shows the overall design of the UHV recipient including the preparation chamber (P) and the cryostat chamber (C). The cryostat consists of concentric bath cryostats of liquid N_2 at 77 K and liquid He^4 at 4.2 K. The containers of the cryogenic liquids are all radiation shielded such that the thermal input power remains low. The shields themselves are highly reflective for heat radiation by use of noble metal coatings and are thermally coupled to the cryogenic gas flow by heat exchanges. This ensures that the latent heat of the cold gas is as well used to keep the cryostat cool. The last cooling stage consists of a He^3 Joule-Thomson cooling stage (He^3) in which He^3 gas is injected at >1.5 bar, precooled with heat exchangers to 4.2 K and then further cooled by free expansion through a capillary into the He^3 cryostat. The latter is pumped by an external pump to a pressure of ≈0.1 mbar. The total throughput of He^3 gas corresponds to 3 liters per hour under ambient conditions giving an estimated cooling power of 1 mW at 500 mK. Below the He^3 cryostat, the cryogenic STM is fixed. It is vibrationally insulated by three springs of resonance frequency below 1 Hz and is thermally coupled to the cryostat by Cu wires. The input of heat is kept at a minimum (≈100 μW) by thermal insulation from the He^4 bath. All parts of the cryostat and the STM were modelled with finite element methods to find their mechanical eigenmodes and frequencies. In an optimization process, the lowest eigenmodes were damped by mechanically suspension at the positions of vibration maxima or by thickening of critical parts.

After designing the cryostat and the STM. The system was manufactured in the mechanical workshop of the Physikalisches Institut, assembled and tested. The careful design of the cryostat minimized the heat input to 8.5 W to the 77 K bath and 30 mW to the 4.2 K bath such that a consumption of only 153 g/h of liquid N_2 and 5.6 g/h of liquid He^4 could be achieved. This corresponds to standing times of 105 hours for liquid nitrogen (20 liters) and 230 hours for liquid helium (10 liters). Keeping in mind, that the cryostat has to take up the heat input of the He^3 injection and pumping lines (50% of the load on the 4.2 K bath) as well as a 50 A current line for a superconducting magnet, this consumption is extraordinary low. It could only be achieved by the high efficiency of the heat exchangers of ≈90% for the nitrogen and ≈50% for the helium flow.

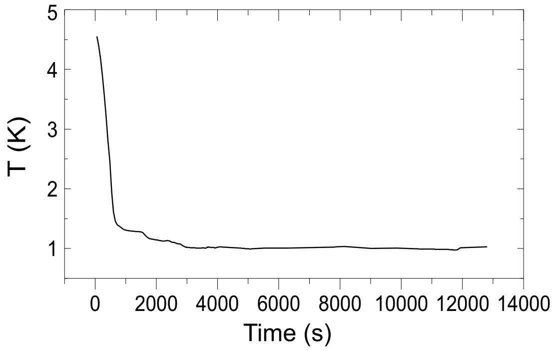

Figure 2: Evolution of the STM temperature during cooling down using the Joule-Thomson stage. At 0 seconds, the Joule-Thomson expansion was started and at 1500 stopped. The temperature further drops until at about 12000 seconds, all He^3 is consumed and the temperature rises.

In test experiments of the Joule-Thomson expansion using He^4, the STM temperature has been recorded as function of time (see Figure 2). Starting at 4.5 K, the temperature of the STM quickly cooled down to about 1.3 K during filling the He^3 cryostat in the first 1500 seconds indicating an effective thermal coupling. After stopping the He input, a base temperature of 970 mK has been reached at about 3000 seconds until all the He is consumed in about 3 hours. This base temperature converts to an expected base temperature for operation with He^3 of 420 mK. The high voltage electric lines to the STM are of low thermal conductivity and are thermally anchored at 4.2 K and at the He^3 cryostat. The two coaxial lines for the tunneling current and the bias voltage are anchord the same way. These cables are of low capacitance (≈30 pF/m) and effective damping at high frequencies (-80 dB/m at 8 GHz and a 20 dB drop per octave) to hinder infrared photon conduction down the cable and to ensure low electron temperatures at the tunneling junction.

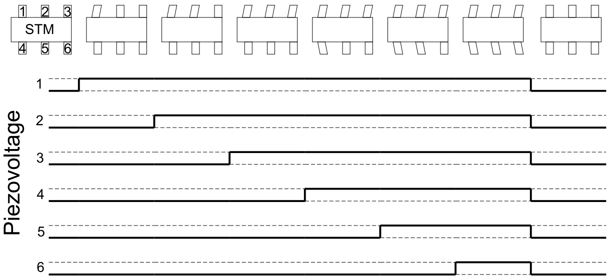

Figure 3: Time sequence of the high voltage on the six shear piezos for coarse motion together with a schematic drawing of the motion process.

To drive the STM, a commercially available STM electronics has been used [2]. The electronics controls the feedback loop, the sample bias and the scanning procedure. A second electronics, that has been designed and built in the Physikalische Institut, provides the electrical signals to coarse position the STM tip within reach of the sample surface. The approach mechanism is based on the design by Pan et al. [3], in which six shear piezos drive the coarse motion (see Figure 3). When activated one after the other, the individual piezos slide, as the friction of the other five sheer piezos dominates. When addressed at the same time, the tip moves with the piezos. The coarse motion and the operation of the STM itself has been tested in air and in UHV in the fourth floor of the building without the full damping system showing a stability better than 100 pm. This promises a good performance once that machine is transferred to the cellar and is vibration insulated using a laminar flow damping system.

Due to the good performance of the cryostat and the STM, the design of the machine has been licensed to industrial partners and will be on the market in 2009.

[1] J. Klein *et al.*, Phys. Rev. B **7**, 2336 (1973)
[2] CreaTec Fischer & Co GmbH, www.createc.de
[3] S. H. Pan *et al.*, Bull. Am. Phys. Soc. **37**, 167 (1992)

Molecular deposition by pulse injection: tetrahydrofuran as codeposited solvent

C. Pérez León, C. Sürgers, M. Marz, R. Hoffmann, H. v. Löhneysen, M. Mayor[1]

The deposition of organic molecules on metal substrates has been extensively studied during the last years due to their increasing interest in functional materials and molecular electronics. The most common method for depositing organic molecules under ultra-high vacuum (UHV) conditions is thermal sublimation. This method, however, can neither be applied to reactive molecules nor to large molecules, since in many cases they are apt to decompose before sublimation. Among alternative deposition methods, pulse injection [1] is very promising: a solution of the molecules under investigation is injected into the UHV chamber using a high-speed pulse valve. When the solvent enters the chamber it vaporizes quickly, ideally leaving only the molecules under investigation on the substrate surface. Compared with solution-based deposition methods this approach has the advantage that the substrate is never exposed to air throughout the process, so that the sample is prepared *in situ*, however with the disadvantage that the solvent is injected into the chamber as well, with the risk of contaminating the substrate. The residual solvent on the substrate after deposition is usually removed by thermal desorption [2, 3], however the necessary heat treatment can also give rise to desorption or decomposition of the molecules under investigation [3].

Here, we present the results of the investigation of the deposition by pulse injection on Cu(111) of π-conjugated organic oligomer $C_{114}H_{158}O_8S_2Si_2$ (CHOSSi) (Fig. 1) dissolved in tetrahydrofuran (THF) C_4H_8O by scanning tunneling microscopy at room temperature (RT). The CHOSSi molecule with a molecular mass of 1776.77 u and an estimated length of about 5–6 nm, corresponds to a segment of the giant macrocycle $C_{768}H_{928}O_{64}S_{16}$ [4]. In order to carry out the pulse-injection deposition, a specially designed molecular deposition chamber was used. The deposition chamber is connected to a UHV system equipped with a RT scanning tunneling microscope (STM) and other facilities for substrate preparation and surface characterization, such as a sputter gun and a cylindrical mirror analyser for Auger electron spectroscopy (AES). It is also equipped with an independent pumping system and permits the deposition of the molecules through a pulse valve located above and close to the substrate. Solutions with a concentration $\sim 8 \times 10^{-6}$ M of CHOSSi in THF ($\sim 1.5 \times 10^{-5}$ mass fraction) were used. The base pressure in the deposition chamber was lower than 2×10^{-9} mbar. The valve was opened for a short time of 10 to 12 ms to keep the pressure below 5×10^{-6} mbar, once or several times, in intervals of several minutes, i. e., the time needed for recovering the base pressure. After the completion of the deposition, the sample was transferred to the analysis chamber.

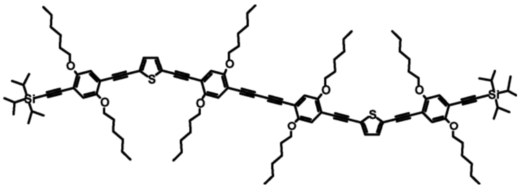

Figure 1: The $C_{114}H_{158}O_8S_2Si_2$ molecule.

Fig. 2 shows images of the Cu(111) surface after deposition of CHOSSi and THF. Image (a) shows several bright protrusions of different sizes, typically a few nm, which are distinguished from an ordered background with features on a much smaller scale. The observed features can be classified by taking into account their relative abundance, their geometry and apparent size. Spots with a dimension of about 4 nm or bigger are ascribed to clusters of several CHOSSi molecules. Some of these clusters are marked with a white circle. Individual CHOSSi molecules are observed as well. The majority appear to be folded forming a kind of knot with usually a circular shape of approximately 2.5–3 nm diameter (dashed white circles). A few of the individual molecules appear unfolded as small chains of 4–6 nm (white arrow). Fig. 2 (b) shows an image of an unfolded CHOSSi molecule, a chain-like structure with some additional protrusions at the edge. The three small bright spots on the right-handside correspond well to the position of the silicon moiety at the edge of the oligomer. The left-handside, however, does not show such protrusions. It is possible that the molecule is not completely unfolded, thereby hiding this part of its structure. The small structures which form the ordered background, clearly visible in Fig. 2 (a), are attributed to solvent molecules. THF molecules self-organize with selected orientations. Additional solvent molecules are adsorbed on this layer and appear as small isolated dots of 0.6 to 1 nm in Fig. 2 (a). A high-resolution STM image of the adsorbed THF molecules is shown in Fig. 2 (c), where domains with a self-ordered periodic structure

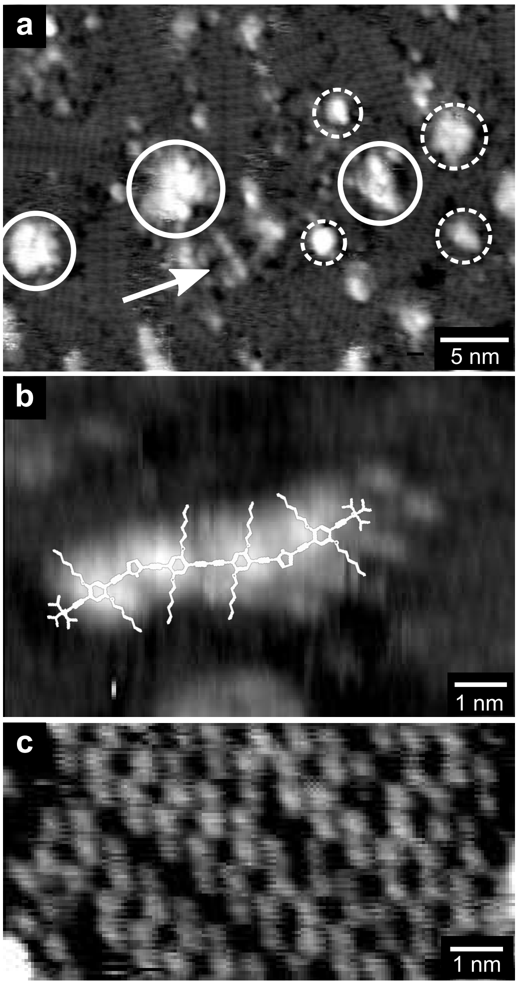

Figure 2: RT-STM images of Cu(111) after deposition of CHOSSi dissolved in THF: (a) 35 × 25 nm^2; 0.70 nA, 2 V. (b) Image of a single CHOSSi molecule with a schematic of the molecule, 9 × 6 nm^2; 0.20 nA, 2 V. (c) Image of a self-organized domain of THF, 8 × 4 nm^2; 0.20 nA, 2.5 V.

can be distinguished. The orientation of the different domains appears to follow selected directions that can be associated with the orientation of the (111) planes of copper. This is corroborated by the angles formed between the domains imaged in Figure 2 (a) which are close to 30° or 60°. The distance between nearest-neighbor protrusions of around 0.7 nm corresponds to the size of a THF molecule. Other features appearing on the STM images are believed to be clusters of molecules or impurities.

The diverse arrangements of the CHOSSi molecules on Cu(111), i.e., folded and unfolded, isolated molecules or clusters, are a consequence of the deposition method, together with the interaction between different constituents: substrate, CHOSSi molecules and solvent molecules. The non-polar CHOSSi molecules when dissolved in a polar solvent such as THF tend to fold and stay in a knotted way to minimize their energy. In the present case, the injection of the molecular solution is done through a high-speed pulse valve. Therefore, when the solution enters the chamber, most of the solvent vaporizes quickly leaving the molecules under investigation on the surface. If the solvent is completely evaporated, the molecule does not have a medium in which to unfold, thus remaining knotted at the surface. However, a small amount of solvent (with dissolved molecules) arrives at the surface, as deduced from the STM images. The presence of the residual solvent permits the molecules to unfold and even to form ordered aggregates with other oligomers. The STM images show the presence of self-organized THF structures which demonstrate a strong interaction of the THF molecules with the substrate. On the other hand, the CHOSSi oligomers do not seem to show any special affinity to it, since in previous experiments with less diluted THF solutions and also with cholorform solvent, no binding at the surface could be measured by STM. Apparently, the THF solvent provides a matrix into which the CHOSSi molecules are embedded, introducing kinetic constraints that permit their imaging by STM. It is likely that the self-ordered THF molecules form H-bonding with the alkyl chains of the CHOSSi molecules, attaching them to the surface and immobilizing them.

The measured STM images at room temperature show that the pulse-injected CHOSSi and THF molecules coadsorb on the copper surface. Both species can be identified and imaged with high-resolution via STM at room temperature, in contrast to previous reports where only in few cases was the solvent observed by STM, and then at low temperatures only [3, 4], at which the migration of the molecules is quenched. Further study of the self-organized adsorption of the THF molecules on Cu(111) is in progress.

This work was supported by the Deutsche Forschungsgemeinschaft through the Center for Functional Nanostructures (CFN).

[1] H. Tanaka, T. Kawai, J. Vac. Sci. Tech. B **15**, 602 (1997).

[2] Y. Terada, B.-K. Choi, S. Heike, M. Fujimori, T. Hashizume, Nano Lett. **3**, 527 (2003).

[3] S. Guo, S. A. Kandel, J. Chem. Phys. **128**, 014702 (2008).

[4] M. Mayor, C. Didschies, Angew. Chemie Int. Ed. **42**, 3176 (2003).

[1] Forschungszentrum Karlsruhe, Institut für Nanotechnologie, D-76021 Karlsruhe, and Department of Chemistry, University of Basel, CH-4056 Basel

Fabrication of suspended Si_3N_4 masks for shadow evaporation of CPP thin-film structures

Richard Montbrun, Christoph Sürgers and Hilbert v. Löhneysen

In a superconducting ferromagnet / superconductor / ferromagnet (FSF) spin switch the superconducting transition temperature T_c can be controlled by the relative orientation of the two F layer magnetizations from parallel (P) to antiparallel (AP). This is possible due to the different coercive fields of the top and the bottom F layer. We have investigated FSF triple layers with perpendicular magnetic anisotropy [1, 2]. Usually, FSF structures are investigated in the current-in-plane (CIP) geometry. The aim of this work is the fabrication of nanostructured FSF contacts for current-perpendicular-to-plane (CPP) transport measurements.

The experimental technique to create FSF layers in CPP layout is the shadow evaporation technique through Si_3N_4 masks. A 200 nm thick Si_3N_4 membrane is separated from the substrate by a 800 nm thick SiO_2 layer on a Si (100) substrate. On those preprocessed wafers (Fa. Si-Mat) a PMMA layer is spin-coated for further e-beam lithography.

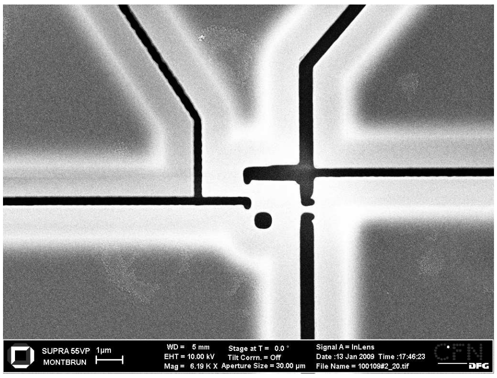

Figure 1: Layout for deposition of FSF-structures. The bright grey areas indicate the underetched self-supporting Si_3N_4 mask. The dark stripes indicate the openings through which the materials will be deposited.

Due to the different etching rates of Si_3N_4 and PMMA (1:1 or 1:2, depending on the hardness of the e-beam resist) in the reactive ion etching (RIE) process the thickness of the PMMA was chosen 400 nm. The parameters for spincoating in this case are 150 seconds at a spinning-speed of 2000 rpm. After that the coated substrates are baked in a convection oven at a temperature of 165 °C for 60 minutes.

The e-beam lithography is done in a Leo Supra 55VP scanning electron microscope (SEM) (Fa. Carl Zeiss). Small structures are written as lines with a line dose of 3200 pC/cm and a step size of 16 nm. Large areas (i.e. contact pads of 250 x 250 μm^2) are written as squares with an area dose of 640 $\mu C/cm^2$ and a step size of 32 nm. Changing the aperture from 10 μm (small structures) to 120 μm (large structures) during lithography reduces the writing time for one structure from 13 hours to $\approx$ 20 minutes.

After lithography the structures are developed in a mixture of methyl isobutyl ketone (MIBK) and isopropyl alcohol (IPA) for about 5 seconds and stopped in a stopping bath for 30 seconds. Annealing the substrates at 110 °C for 30 minutes hardens the residual PMMA.

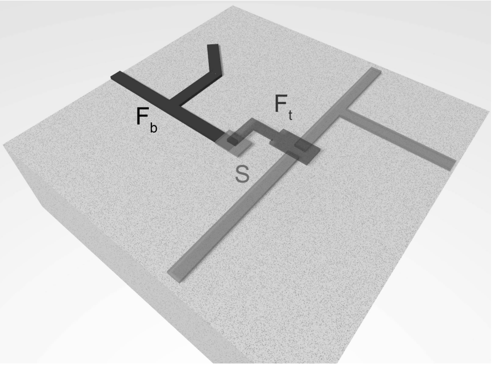

Figure 2: Structures for CPP transport measurements. The evaporation through the mask under three different angles will result in a triple structure. Only the electrically active parts for the CPP transport measurements are shown.

RIE is performed in a SI 220 plasma etching device (Fa. Sentech Instruments). For the Si_3N_4 etching step, SF_6 is used with a power of 50 W for $\approx$ 1500 seconds. In order to remove the remaining PMMA, O_2 plasma with a power of 100 W is ignited for a few minutes. Finally, wet etching is done in a buffered hydrofluoric acid (BHF = HF + NH_4F + H_2O) for about 40 minutes. This solution ist pH-neutral and provides a reproducible etching rate. After that the substrates have to be cleaned in bidestilled H_2O. Figure 1 shows the mask for shadow evaporation and Figure 2 a scetch of the final FSF structure.

[1] A. Singh et al., Phys Rev. B **75**, 024513 (2007).
[2] A. Singh et al., APL **91**, 152504 (2007).

Diploma theses

Hartbaum, Julian	Zur spezifischen Wärme von $CeCu_{5.7}Au_{0.3}$ und UCoGe
Hiebel, Fanny	Investigation of the interface of epitaxial graphene with 6H-SiC(0001) (Carbon face) via scanning tunneling microscopy
Hübler, Florian	Transportmessungen in Supraleiter-Ferromagnet Hybridstrukturen
Kimpel, Thomas	Herstellung und Wachstumsoptimierung epitaktischer Ca_2RuO_4-Schichten
Müller, Marc	Magnetfeldinduziertes Schalten von Dysprosium-Bruchkontakten
Schneider, Johannes	Magneto-Transport in Graphit
Schuh, Tobias	Magnetische Anregungen von Fe- und Co-Atomen, -Dimeren und -Trimeren auf Pt(111)
Urban, Nicolai T.	Stehende Spinwellen in extrem dünnen ferromagnetischen Co-Filmen auf Cu(100) untersucht mit inelastischer Tunnelspektroskopie
Witt, Florian	Untersuchung des Elektronentransports über einzelne Phtalocyaninmoleküle

Doctoral dissertations

Schnelzer, Lars	Spindynamik an zyklischen Eisen-Rädern in hohen magnetischen Feldern

Long-term guests

J. V. Yhakmi, Bhaba Atomic Research Center, Mumbai, India	21.04.2008 - 15.05.2008	BMBF/DLR
A. Nateprov, Institute of Applied Physics Kishinev, Moldova	01.01.2008 - 31.01.2008	DAAD
T. Miyamachi, Osaka University, Japan	01.11.2008 - 31.12.2008	Japanese Physical Society
V. Saxena, Bhaba Atomic Research Center, Mumbai, India	01.09.2008 - 23.11.2008	BMBF/DLR
T. K. Yamada, Gakushuin University, Tokyo, Japan	01.03.2008 - 31.12.2008	Alexander von Humboldt-Stiftung

Teaching activities

Summer term 2008

Prof. Dr. G. Weiß	Lecture	Physik I (Mechanik)
Prof. Dr. G. Weiß, Dr. G. Fischer	Tutorial	Physik I (Mechanik)
HD Dr. G. Goll	Lab course	Physics laboratory course for mechanical engineers
HD Dr. G. Goll, Dr. R. Hoffmann-Vogel	Lecture	Elektronische Eigenschaften von Festkörpern I
Dr. C. Sürgers	Lab course	Physikalisches Fortgeschrittenen Praktikum
Prof. Dr. W. Wulfhekel	Lecture	Ausgewählte Kapitel der Physik für Chemieingenieure, Verfahrenstechniker, Bio- und Wirtschaftsingenieure
Prof. Dr. W. Wulfhekel, Dr. G. Fischer	Tutorial	Ausgewählte Kapitel der Physik für Chemieingenieure, Verfahrenstechniker, Bio- und Wirtschaftsingenieure
Prof. Dr. W. Wulfhekel	Lecture	Moderne Physik für Ingenieurpädagogen
Prof. Dr. W. Wulfhekel, Dr. G. Fischer	Tutorial	Moderne Physik für Ingenieurpädagogen

Prof. Dr. W. Wulfhekel, Prof. Dr. G. Weiß, Dr. M. Lukas, Dr. C. Pérez León	Seminar	Hauptseminar: Rastersondenmethoden
Prof. Dr. H. v. Löhneysen, Dr. D. Beckmann, Dr. V. Fritsch, Dr. R. Krupke	Seminar	Hauptseminar: Magnetismus
Prof. Dr. H. v. Löhneysen, Prof. Dr. A. Ustinov, Prof. Dr. G. Weiß, Prof. Dr. W. Wulfhekel	Seminar	Institutsseminar
Prof. Dr. H. v. Löhneysen, Prof. Dr. G. Weiß, Prof. Dr. A. Ustinov, Prof. Dr. W. Wulfhekel, Dr. K.-P. Bohnen	Seminar	Gemeinsames Seminar Universität/Forschungszentrum über Festkörperphysik
Prof. Dr. H. v. Löhneysen, HD Dr. G. Goll	Seminar	Seminar über aktuelle Fragen der Festkörperphysik
Prof. Dr. G. Weiß	Seminar	Seminar über Fragen der Festkörperphysik
Prof. Dr. W. Wulfhekel	Seminar	Seminar zur Oberflächenphysik

Winter term 2008/09

Prof. Dr. G. Weiß, Dr. V. Fritsch, Dr. G. Fischer	Lecture	Mathematik-Vorkurs für Physiker
Prof. Dr. G. Weiß	Lecture	Physik I (Mechanik)
Prof. Dr. G. Weiß, Dr. G. Fischer	Tutorial	Physik I (Mechanik)
Prof. Dr. H. v. Löhneysen	Lecture	Physik V (Festkörperphysik)
Prof. Dr. H. v. Löhneysen, Dr. R. Hoffmann-Vogel	Tutorial	Physik V (Festkörperphysik)
Dr. C. Sürgers	Lab course	Physikalisches Fortgeschrittenen Praktikum
Prof. Dr. W. Wulfhekel	Lecture	Elektronische Eigenschaften von Festkörpern II
Prof. Dr. W. Wulfhekel	Tutorial	Elektronische Eigenschaften von Festkörpern II
Apl. Prof. B. Pilawa	Lecture	Magnetische Resonanz

Prof. Dr. A. Ustinov	Lecture	Superconductivity
HD Dr. G. Goll	Lecture	Modern physics (KSOP)
HD Dr. G. Goll, Dr. Dr. V. Fritsch	Tutorial	Modern physics (KSOP)
Prof. Dr. W. Wulfhekel, Prof. Dr. G. Weiß, Dr. M. Lukas, Dr. C. Pérez León, Dr. T. Yamada	Seminar	Hauptseminar: Rastersondenmethoden
Prof. Dr. H. v. Löhneysen, HD Dr. G. Goll, Dr. V. Fritsch, Dr. R. Schäfer	Seminar	Supraleiter und Supraflüssigkeiten
Prof. Dr. A. Ustinov, Dr. J. Lisenfeld, Dr. S. Poletto	Seminar	Qubits
Prof. Dr. W. Wulfhekel,	Lab Course	Physikalisches Anfängerpraktikum für Chemiker, Bio- und Geowissenschaftler, Technomathematiker
Prof. Dr. A. Ustinov,	Lab Course	Physikalisches Anfängerpraktikum für Maschinenbauer
Prof. Dr. H. v. Löhneysen, Prof. Dr. A. Ustinov, Prof. Dr. G. Weiß, Prof. Dr. W. Wulfhekel	Seminar	Institutsseminar
Prof. Dr. H. v. Löhneysen, Prof. Dr. G. Weiß, Prof. Dr. A. Ustinov, Prof. Dr. W. Wulfhekel, Dr. K.-P. Bohnen	Seminar	Gemeinsames Seminar Universität/Forschungszentrum über Festkörperphysik
Prof. Dr. H. v. Löhneysen, HD Dr. G. Goll	Seminar	Seminar über aktuelle Fragen der Festkörperphysik
Prof. Dr. A. Ustinov	Seminar	Seminar on Quantum Circuits
Prof. Dr. G. Weiß	Seminar	Seminar über Fragen der Festkörperphysik
Prof. Dr. W. Wulfhekel	Seminar	Seminar zur Oberflächenphysik
HD Dr. G. Goll	Seminar	Seminar über aktuelle Arbeiten

Seminar talks at Physikalisches Institut

07.01.2008*	H. J. W. Zandvliet	Self-organizing organic chains: Pt on Ge(001)
14.01.2008*	C. Pinta	LaCoO$_3$ thin films: electronic and magnetic structure
21.01.2008	G. Rodary	Electron confinement and magnetic properties of nanostructures studied by low-temperature STM
28.01.2008*	D. Schaadt	Molecular beam epitaxy of semiconductor heterostructures
04.02.2008	C. Sürgers	Eindrücke aus Indien
11.02.2008*	T. Miyamachi	Nanostructures and magnetism of Co thin films on Au(001)
07.04.2008*	S. M. Stichov	Experimental study of magnetic phase transition in the itinerant helimagnet MnSi at ambient and high pressure
14.04.2008	M. Kenzelmann	Unconventional magnetism in a magnetically-induced superconductor
21.04.2008*	T. Yamada	Study of magnetic material surfaces by means of room-temperature spin-polarized STM/STS
28.04.2008	P. Fusik	Allgemeine Sicherheitsbelehrung
05.05.2008*	S. Drobnik	Thermische Ausdehnung bei tiefen Temperaturen an CeCu$_{6-x}$Au$_x$
19.05.2008*	Y. Nahas	Ordered alloy nanostructures on gold surfaces: elaboration and magnetism
26.05.2008	M. Greiter	Are stripe correlations essential to high T$_c$ superconductivity? $-or-$ The proper interpretation of a high energy neutron scattering experiment
02.06.2008*	J. Pollmann	Verblüffende Adsorptionsprozesse auf Halbleiteroberflächen: Was kann die Theorie zur Erklärung beitragen?
09.06.2008	J. Lisenfeld	Experiments on superconducting Josephson phase quantum bits
16.06.2008	S. Blatt	Dielektrophorese von einwandigen Kohlenstoff-Nanoröhren

23.06.2008	W. Schirmacher	Anomale Schwingungseigenschaften in ungeordneten Festkörpern
30.06.2008*	M. Bowen	Electronic symmetries in spin electronics
07.07.2008	T. Balashov	Magnetic excitations in thin films and atomic clusters probed by inelastic scanning tunneling spectroscopy
14.07.2008*	M. Merz	Oribital degrees of freedom in single-layered manganites
20.10.2008	C. Sürgers	Ferromagnetismus durch Kohlenstoffdotierung von Mn_5Si_3
27.10.2008*	B. Gopalakrishnan	Single spins in diamond - probing science at the nanoscale
03.11.2008	V. Saxena	Polymer transistors with chemically modified dielectric interfaces
10.11.2008*	M. Smith	Wiedemann-Franz violation near a quantum critical point: reports of quasiparticle's death may be exaggerated
17.11.2007	M. Brando	Quantum criticality in slightly Ir- and Co-doped $YbRh_2Si_2$
24.11.2008*	S. Poletto	Coherent oscillations in a superconducting tunable flux qubit manipulated without microwaves
01.12.2008	C. Gao	Investigation of antiferromagnetic thin films with STM: spin structure and magnetic excitations
08.12.2008*	P. Buczk	Spin dynamics of complex itinerant magnets
15.12.2008	C. Heiliger	Ab initio description of spin-dependent transport in tunnel junctions
22.12.2008*	A. Varlamov	Physics of Christmas cooking

* Gemeinsames Seminar über Festkörperphysik von Universität und Forschungszentrum

Publications

T. Balashov, A. F. Takacs, M. Däne, A. Ernst, P. Bruno, W. Wulfhekel	*Inelastic electron-magnon interaction and spin transfer torque*, Phys. Rev. B **78** (2008) 174404
M. Bode, O. Pietzsch, A. Kubetzka, W. Wulfhekel, S. McVitie, J. N. Chapman	*Comment on: Three-dimensional, spin-resolved structure of magnetic vortex and antivortex states in patterned Co films using scanning ion microscopy with polarization analysis*, Phys. Rev. Lett. **100** (2008) 29703
A. K. Chauhan, D. K. Aswal, S. P. Koiry, S. K. Gupta, J. V. Yakhmi, C. Sürgers, D. Guerin, S. Lenfant, and D. Vuillaume	*Self-assembly of the 3-aminopropyltri-methoxysilane multilayers on Si and hysteretic current-voltage characteristics*, Appl. Phys. A **90** (2008) 581
A. K. Debnath, S. Samanta, A. Singh, D. K. Aswal, S. K. Gupta, J. V. Yakhmi, S. K. Deshpande, A. K. Poswal, C. Sürgers	*Growth of iron phthalocyanide nanoweb and nanobrush using molecular beam epitaxy*, Physica E **41** (2008) 154-163
S. Domingo Köhler, B. Pilawa, D. Saez de Jauregui, G. Fischer, R. Grubba, R. Köppe, A. Schnepf, H. Schnöckel, E. Dormann	*Magnetic resonance of the new neutral Al cluster radical*$[Al_7R_6]$, Euro. Phys. Lett. **8** (2008) 37002
C. L. Gao, A. Ernst, A. Winkelmann, J. Henk, W. Wulfhekel, P. Bruno, J. Kirschner	*Noncollinear surface spin density by surface reconstruction in the alloy NiMn*, Phys. Rev. Lett. **100** (2008) 237203
C. L. Gao, A. Ernst, G. Fischer, W. Hergert, P. Bruno, W. Wulfhekel, J. Kirschner	*Spin wave dispersion on the nanometer scale*, Phys. Rev. Lett. **101** (2008) 167201
C. L. Gao, W. Wulfhekel, and J. Kirschner	*Revealing the 120° antiferromagnetic Néel structure in real space: One monolayer Mn on Ag(111)*, Phys. Rev. Lett. **101** (2008) 267205
G. Goll, M. Marz, A. Hamann, T. Tomanic, K. Grube, T. Yoshino, and T. Takabatake	*Thermodynamic and transport properties of the noncentrosymmetric superconductor LaBiPt*, Physica B **403**, (2008) 1065
B. Gopalakrishnan, C. Sürgers, R. Montbrun, A. Singh, M. Uhlarz, H. v. Löhneysen	*Electronic transport in magnetically ordered* $Mn_5Si_3C_x$ *films*, Phys. Rev. B **77** (2008) 104414
R. Hoffmann, D. Weissenberger, J. Hawecker, D. Stöffler	*Conductance of gold nanojunctions thinned by electromigration*, Appl. Phys. Lett. **93** (2008) 043118/1-3
W. Knafo, C. Meingast, A. Inaba, Th. Wolf, H. v. Löhneysen,	*Heat capacity and magnetic phase digram of the low-dimensional antiferromagnet* Y_2BaCuO_5, J. Phys.: Cond. Matt. **20** (2008) 335208

I. Kokanović, A. Helzel, D. Babić, C. Sürgers, C. Strunk	*Effect of vortex-core size on the flux lattic in a mesoscopic superconducting strip*, Phys. Rev. B **77** (2008) 172504; Virtual Journal of Nanoscale Science & Technology 17 (Issue 22) (2008); http://www.vjnano.org; Virtual Journal of Applications of Superconductivity 14 (Issue 11) (2008); http://www.vjsuper.org
E. Moyen, M. Macé, C. Léandri, L. Masson, G. Agnus, A. Fleurence, T. Maroutian, W. Wulfhekel, B. Bartenlian, P. Beauvillain, M. Hanbücken	*Selective functionalization of Si(111) and Ag(110) surfaces for preparation of Co nanostructures*, J. Phys.: Conference Series **100** (2008) 72002 1-4
T. Pietrus, H. v. Löhneysen, P. Schlottmann	*Kondo-hole conduction in the La-doped Kondo insulator* $Ce_3Bi_4Pt_3$, Phys. Rev. B **77** (2008) 115134
C. Pinta, D. Fuchs, M. Merz, M. Wissinger, E. Arac, H. v. Löhneysen, A. Samartsev, P. Nagel, S. Schuppler	*Suppression of spin-state transition in expitaxially strained* $LaCoO_3$, Phys. Rev. B **78** (2008) 174402
N. Quershi, H. Fuess, H. Ehrenberg, B. Ouladdiaf, J. Rodriguez-Carajal, T. C. Hansen, Th. Wolf, C. Meingast, Q. Zhang, W. Knafo, H. v. Löhneysen	*Magnetic structure of the Kagome mixed compound* $(C_{0.5}N_{0.5})_3V_2O_8$, J. Phys.: Cond. Matt. **20** (2008) 235338
K. Ruschmeier, A. Schirmeisen, R. Hoffmann	*Atomic scale force vector fields*, Phys. Rev. Lett. **101** (2008) 156102/1-4
S. Sakarya, N. T. Huy, N. H. van Dijk, A. de Visser, M. Wagemaker, A. C. Moleman, T. J. Gortenmulder, J. C. P. Klaasse, M. Uhlarz, H. v. Löhneysen	*Evolution of ferromagnetic order in URhGe alloyed with Ru, Co and Si*, J. Alloy. Comp. **457** (2008) 51
M. Stokmaier, G. Goll, D. Weissenberger, C. Sürgers, H. v. Löhneysen	*Size dependence of current spin polarization through superconductor/ferromagnet nanocontacts*, Phys. Rev. Lett. **101** (2008) 147005
C. Sürgers, K. Potzger, T. Strache, W. Möller, G. Fischer, N. Joshi, H. v. Löhneysen	*Magnetic order by C-ion implantation into* Mn_5Si_3 *and* Mn_5Ge_3 *and its lateral modification*, Appl. Phys. Lett. **93** (2008) 062503
A. F. Takacs, F. Witt, S. Schmaus, T. Balashov, M. Bowen, E. Beaurepaire, W. Wulfhekel	*Electron transport through single phthalocyanine molecules with STM*, Phys. Rev. B **78** (2008) 233404
M. Wasniowska, W. Wulfhekel, M. Przybylski, J. Kirschner	*Submonolayer regime of Co epitaxy on Pd(111): Morphology and electronic structure*, Phys. Rev. B **78** (2008) 035405
J. Winterlik, G. H. Fecher, C. Felser, M. Jourdan, K. Grube, F. Hardy, H. v. Löhneysen, K. L. Holman, R. J. Cava	*Ni-based superconductor: Heusler compound* $ZrNi_2Ga$, Phys. Rev. B **78** (2008) 184506
J. Wosnitza, G. Goll, M. Bartkowiak, B. Bergk, A. D. Bianchi, H. v. Löhneysen, T. Yoshino, and T. Takabatake	*Possible magnetic-field-induced Lifshitz transition in CeBiPt*, Physica B **403**, (2008) 1219

Scientific and technical staff

Prof. Dr. Hilbert v. Löhneysen

Drobnik, Stefanie, Dr.
Fritsch, Veronika, Dr.
Hoffmann, Regina, Dr.
Pérez León, Carmen, Dr.
Weber, Frank, Dr.

Bagrets, Nadezda, Dipl.-Phys.
Drotziger, Sandra, Dipl.-Phys.
Hamann, Andreas, Dipl.-Phys.
Montbrun, Richard, Dipl.-Phys.
Sauter, Markus, Dipl.-Phys.
Stöffler, Dominik, Dipl.-Phys.
Tomanic, Tihomir, Dipl.-Phys.
Müller, Marc, Dipl.-Phys.

Prof. Dr. Alexey Ustinov

Lisenfeld, Jürgen, Dr.
Lukashenko, Oleksandre, Dr.
Poletto, Stefano, Dr.

Fedorov, Kirill, Dipl.-Phys.
Feofanov, Alexey, Dipl.-Phys.
Wirth, Tobias, Dipl.-Phys.
Grabovskij, Grigorij, cand. phys.
Schwemmer, Christian , cand. phys.

Prof. Dr. Georg Weiß

Kaupp, Thomas, Dipl.-Phys.
Peichl, Torben, Dipl.-Phys.

Adler, Clemens, cand. phys.
Aslan, Ferhat, cand. phys.
Wirner, Frank, cand. phys.

Prof. Dr. Wulf Wulfhekel

Yamada, Toyo Kazu, Dr.
Nahas, Yasmine, Dr.

Balashov, Timofey, Dipl.-Phys.
Schmaus, Stefan, Dipl.-Phys.
Schuh, Tobias, Dipl.-Phys.
Urban, Nicolai, Dipl.-Phys.
Witt, Florian, Dipl.-Phys.

Bork, Annika, cand. phys.
Gerhard, Lukas, cand. phys.
Gerstl, Stefan, cand. phys.
Zhang, Lei, cand. phys.

Apl. Prof. Dr. Bernd Pilawa

Schnelzer, Lars, Dr.

HD Dr. Gernot Goll

Marz, Michael, Dipl.-Phys.
Bouvron, Samuel, Dipl.-Phys.
Hartbaum, Julian, Dipl.-Phys.
Mirlin, Konstantin, Dipl.-Phys.

Permanent scientific staff

Fischer, Gerda, Dr., Akad. Oberrätin
Sürgers, Christoph, Dr., Akad. Oberrat

Professors emeriti

Baumann, Friedhold, Prof. Dr.
Dormann, Elmar, Prof. Dr.
Hasse, Jörg, Prof. Dr.

Secretary

Baatz, Steffi
Hornung, Monika, also at CFN
Schelske, Birgit

Technical support

Aydin, Orhan, technician
Behrens, Lars, computer assistance
Hugle, Cornelia, sample preparation
Odenwald, Ilse, crystal groth

Helium liquifier

Hartlieb, Franz

Electronics workshop

Johannsen, Torsten
Opfer, Ulrich
Opolony, Christine

Mechanical workshop

Binkert, Erwin
Dehm, Reinhold
Fey, Heinzpeter
Giesinger, Willi
Hummel, Marco
Knecht, Stefan
Masur, Jessica
Pech, Martin
Rose, Jens
Zink, Bernhard

Apprentice machinist workshop

Barner, Björn
Gerber, Roman
Hergt, David
Schöffel, Patrick Kalugin, Michael
Kukelka, Patrick
Schmidt, Dustin
Schmitt, Markus
Weinmann, Tobias

Cover design: C. Sürgers